Spatially and Temporally Resolved Spectroscopy of Transition Metal Dichalcogenide Semiconductors

By

Jason Scheeler

A dissertation submitted in partial fulfillment of

the requirements for the degree of

Doctor of Philosophy

(Chemistry)

at the

UNIVERSITY OF WISCONSIN-MADISON

2024

Date of final oral examination: 08/23/2024, 1:00 PM, Room 9341

This dissertation is approved by the following members of the Final Oral Committee:

John C. Wright, Professor Emeritus, Analytical Chemistry
Song Jin, Professor, Materials Chemistry
Susanna L. Widicus Weaver, Professor, Physical Chemistry and Astronomy
Deniz D. Yavuz, Professor, Atomic and Optical Physics

ABSTRACT

Coherent multidimensional spectroscopy (CMDS) is a powerful analytical technique for learning about the structure and dynamics of quantum states in a variety of sample systems. In this dissertation, we apply CMDS to investigate monolayers and heterobilayers of transition metal dichalcogenide (TMD) semiconductors, a materials system that shows promise in photovoltaic applications. Experiments use multiple 50-femtosecond laser pulses to interrogate the rich exciton diversity in TMDs as a function of frequency, time, and space. First, we motivate adding a widefield nonlinear microscope to our CMDS setup by describing how spatial heterogeneity within monolayer and heterobilayer TMDs affects their optical properties. We discuss the design principles for each component in the widefield nonlinear microscope and present proof of principle measurements on TMDs to validate the instrument. Next, we demonstrate that two-color sum frequency generation (SFG) spectroscopy is capable of probing high-energy conduction bands in monolayer WS_2. We show the technique's general applicability by performing the SFG measurements on TMDs of various sample morphologies. We extract the ultrafast dynamics of charge carriers occupying the high-energy conduction bands throughout the Brillouin zone by preceding the SFG pulse sequence with a pump pulse. Finally, we suggest software improvements to the microscope that would allow it to speed up the camera frame rate and greatly improve the S/N for pump-probe experiments with strong probe fields. For the SFG measurements, we propose additional experiments to further confirm the peak assignments made for monolayer WS_2 and suggest a strategy for directly probing the dynamics of high-energy conduction bands localized at the direct-gap momentum point. This work applies foundational optical principles to build a novel widefield nonlinear imaging system and provides a framework

for developing highly selective, multidimensional probes of non-direct-bandgap states in materials systems with large excitonic transition dipoles.

ACKNOWLEDGEMENTS

Obtaining a PhD is an exciting and rewarding time in one's career. However, I'm well aware that it takes the combined effort of many people, and I'm grateful to those who have helped me professionally, socially, and personally to reach this stage in my scientific career.

My first thank you goes to my advisor John. John taught me the importance of rigor and detail when it comes to doing science. He exemplified to me that the quality of one's scientific work is what people remember most about them, not any award or the number of publications they have, so the work ought to be done correctly. As a young graduate student, I was surprised and impressed that his office door was always open, and the amount of attention he gave to me and students in my cohort. Looking back, this makes sense as to the generous and humble person I know him to be. In my future scientific endeavors, I hope to emulate John's integrity as a scientist and generosity as a person.

To the faculty members who have served on previous and current committees of mine (Song Jin, Marty Zanni, Susanna Widicus Weaver and Deniz Yavuz): I'm grateful for the time you took out of your busy lives to read the written documents and listen to the oral presentations I've prepared throughout the years. Your feedback and guidance have always been insightful.

To the Jin group members who I worked with as part of the Solar supergroup (Yuzhou Zhao, Chris Roy [joint between Jin and Wright], Willa Mihalyi-Koch, Chris Triggs, and Kristel Forlano: thank you for providing me with numerous TMD and perovskite samples, and for your patience as the spectroscopy side of the Jin-Wright collaboration typically advanced more slowly than the synthesis side. I enjoyed our conversations because I usually came away with a new

materials/solid-state chemistry perspective on the research we were doing that I hadn't previously considered or known about.

To the members of Xiaoyang Zhu's group at Columbia University (Feng Liu, Qiuyang Li and Nicholas Olsen): Thank you for providing me with the exfoliated TMD heterobilayer samples that star in this dissertation and for informing me of the gold-tape exfoliation method your group pioneered.

To Dan Kohler: thank you for always being willing to help me in the lab or with data processing/interpretation. Having your spectroscopic intuition literally a desk away was a luxury to have throughout my graduate career. Your patience and empathy as a staff scientist/mentor are admirable.

To my mentor on the TMDs project Darien Morrow: Thank you for investing your time and effort into me learning the ways of the Wright Group and science in general. You made becoming an experimentally competent member of the Wright Group seamless (well, as seamless as it can be considering the difficulty of some of our experiments). You heavily influenced how I conducted myself in the laser lab and how I thought about doing CMDS on TMDs.

To David Lafayette: we shared a similar graduate school experience being only one year apart, working on the fs system, and being on similar projects. It was nice having someone to discuss the highs and lows of graduate school that understood where I was coming from. I benefited greatly from your efforts spending time on OPA alignment and with yaqc-cmds during the COVID years. You were a consistent source of valuable insight for all things related to materials spectroscopy in the Wright Group.

To Kyle Sunden: thank you for always being willing to help me with getting Python scripts to run or issues related to PyCMDS/yaqc-cmds/bluesky-cmds/yaqc-qtpy. I learned a great deal about hardware control, experiment orchestration, and Python in general from you.

To Ryan McDonnell: thank you for expressing your excitement for science in the office, group meetings, at seminars, etc. It often provided me with renewed motivation when I temporarily lost it as an older (and at times, jaded) graduate student. Also, thank you for reviving Spikey. I'm sure they are very appreciative.

To all other Wright Group members I've overlapped with: thank you all for being great coworkers. Our conversations in the labs and offices never failed to be entertaining, intellectually productive, or both.

To Wright Group members of the past: thank you for your theoretical and experimental/software contributions to everything the Wright Group does and is known for. Without the momentum you all had built, my experiments would not have been possible.

To the dodgeball and soccer teams I played on during graduate school: thank you for providing an outlet for exercise and a way to clear my mind if a day at work hadn't gone well. I will look back fondly on the games we played, championships we won, post-game beers, and the friendships I made on those teams.

To Ryan Allen and Matt Ryan (aka Ry and Duck): Hanging out with you two on the weekends always gave me something to look forward to during graduate school as it was never a dull time when the three of us were together. I will never forget our times homebrewing beer at 1317 Chandler St. I look forward to our continued friendship.

To my older brothers Matt and Dan and my parents Steve and Kathy: the sincerest thank you for the unconditional support you all gave to me as I progressed through graduate school.

TABLE OF CONTENTS

1 Introduction and Background Information

1.1 Coherent multidimensional spectroscopy in the Wright Group

Coherent multidimensional spectroscopy (CMDS) is a family of analytical methods that can selectively interrogate the quantum states in a material system. CMDS uses multiple pulsed laser sources to induce a nonlinear polarization, $\tilde{P}$, in the material. The nonlinear polarization can be expressed as a function of the applied electric field in Equation 1 as

$$\tilde{P} = \varepsilon_0\left[\chi^{(1)}\tilde{E} + \chi^{(2)}\tilde{E}^2 + \chi^{(3)}\tilde{E}^3 + \cdots\right] \quad (1)$$

where ε_0 is the permittivity of free space, $\tilde{E}$ is the applied electric field, and $\chi^{(n)}$ is the nth order (non)linear susceptibility. $\tilde{P}$ launches additional electromagnetic fields and one of them is collected for the signal in CMDS experiments. For the collected signal field to have considerable intensity, the phase matching criteria need to be satisfied. That is, the wavevector of the signal field $\vec{k}_{out}$ needs to equal the sum of the wavevectors of the excitation fields $\vec{k}_i$. Phase matching is represented mathematically in Equation 2 as

$$\vec{k}_{out} = \sum_i \pm\vec{k}_i \quad (2)$$

where the index *i* accounts for all excitation field interactions with the sample. The excitation fields can act on the bra or ket of the quantum state's wavefunction which determines the wavevector sign. The value of the wavevector depends on the frequency of the field, the index of refraction of the material at the field's frequency, and the angle at which the field impinges on the sample. How the excitation fields interact with the sample is ultimately decided by the spectroscopist and defines the output phase matching criteria.

$\chi^{(n)}$ is the complex, material-dependent parameter that dictates the output field intensity in a CMDS experiment. It relates the optical properties of a state within a sample (e.g. transition dipole strength, center frequency, and linewidth) to the applied electric field based on the number of field interactions with the sample. When the frequency of the applied electric field is equal to a sample's optical transition frequency, the signal becomes resonantly enhanced. Scanning multiple laser frequencies against one another results in a multidimensional spectrum where peaks occur along the frequency axes. Multi-resonant CMDS (MR-CMDS) creates a multidimensional fingerprint of the sample and the Wright Group has pioneered its use in the frequency domain. MR-CMDS can determine the coupling between different quantum states (which present as cross peaks in the multidimensional spectrum) and decongest crowded linear spectra. MR-CMDS can also interrogate temporal state evolution by changing the time delays between the incident laser beams. The Group has successfully demonstrated MR-CMDS in molecular,[1–3] biological,[4] and solid-state systems.[5–9]

The materials side of the Wright Group at the time that I joined used MR-CMDS to study novel semiconducting materials, namely monolayer transition metal dichalcogenides (1L TMDs) and lead halide perovskites (LHPs). The electronic transitions in these materials are spectrally broad at room temperature and therefore have fast dephasing rates (a few 10s of fs). The primary optical table I worked on, hereafter called the "fs system" (see Appendix A, Section 6), produces spectrally broad pulses with ~50 fs temporal pulse duration making it an ideal ultrafast system to study semiconducting materials. As will be detailed in the following sections, the material system I specialized in is TMDs. The first paper published by the Wright Group on TMDs was in 2015. Kyle Czech, a former Group member, performed transient grating experiments on a few-layer TMD sample to explore, for the first time, the frequency dependence of the ultrafast

dynamics in this material system.[10] The bulk of my foundational MR-CMDS knowledge of TMDs came from the work of my mentor, Dr. Darien Morrow. He performed triple-sum frequency (TSF) spectroscopy on a few-layer TMD sample for the first time.[5] He also quantitatively described how the substrate that supports the TMD sample can obfuscate the TSF signal.[11] The bulk of Darien's dissertation developed multi-photon pumps and multi-photon probes in pump-probe experiments to mitigate substrate response and decrease noise.[6,12]

The samples that Darien investigated were comprised of multiple layers of both substrate and sample. The layers were thin enough such that interference effects were prevalent. He also looked at samples of varying lateral size so the proportion of his beam excitation area interrogating the sample differed between experiments. These sample morphologies often required quantitative optical modeling to understand the spectral line shapes. Overall, Darien's work demonstrated to me that clear spectroscopic signals can be hard to come by in the types of samples we study. This insight, coupled with the fact that 1L TMDs are $\chi^{(2)}$ active (see Chapter 1.2.1.1), motivated me to pursue $\chi^{(2)}$ spectroscopies throughout my graduate research. All the common substrates that support 1L TMDs such as sapphire, fused silica, or protected silicon are either not $\chi^{(2)}$ active or have a negligible $\chi^{(2)}$ which rids the material response of substrate interference. This greatly simplifies signal interpretation.

Figure 1 outlines the wave mixing energy level diagrams (WMELs) for two $\chi^{(2)}$ pathways that play important roles in Chapters 2 and 3. Second harmonic generation (SHG) uses two photons of frequency ω to generate one photon at frequency $\omega_{SHG} = 2\omega$. Sum-frequency generation (SFG) uses two photons with different frequencies, ω_1 and ω_2, to produce one photon at frequency $\omega_{SFG} = \omega_1 + \omega_2$. SHG is the degenerate analogue of SFG. In the context of this dissertation and Wright Group materials spectroscopy in general, SHG is typically used when targeting a single

resonance (the resonance frequency is equal to ω_{SHG}) and SFG is typically used when targeting two resonances (one of the materials' resonances is equal to ω_1 and another resonance is equal to ω_2).

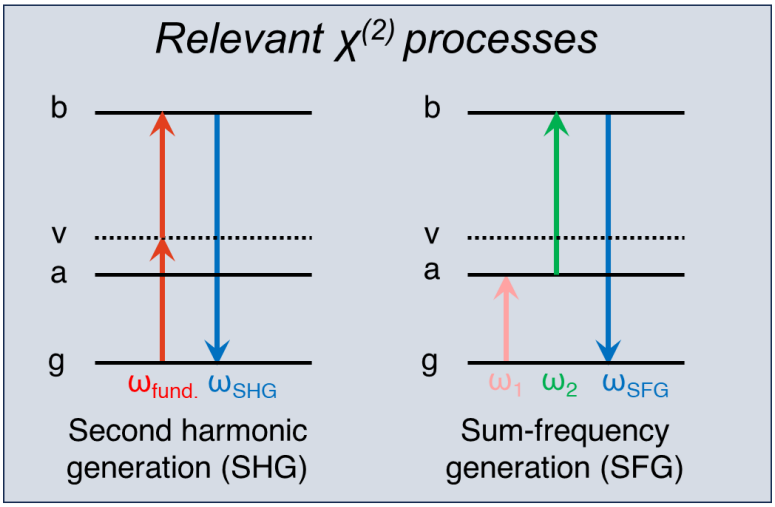

Figure 1 | WMEL diagrams for the $\chi^{(2)}$ processes relevant in this dissertation. SHG is shown on the left and SFG is shown on the right. The input field for harmonic generation processes is often called the fundamental, which is abbreviated as "fund." in the SHG WMEL.

All the measurements on TMDs in the Wright Group up until the time that I joined had been ensemble-averaged, meaning the output signal is the spatially averaged response of the excitation area. Any nuance brought about by heterogeneities within the sample was completely lost. Heterogeneities inherent to the material such as grain boundaries were problematic in gaining a spatially resolved understanding of material response. Furthermore, the *designed* heterogeneity from vertical and lateral heterostructures of 1L TMDs were becoming increasingly important to the TMD photophysics research enterprise.[13,14] For the Wright Group to continue interrogating the most relevant aspects of TMDs and LHPs, the Group needed to add a spatial axis to its MR-CMDS setup. This forms the basis for Chapter 2.

The other main research aim on the TMDs project was to use TMDs as a model system to develop MR-CMDS as an alternative to angle-resolved photoemission spectroscopy for probing the Brillouin zone in solid-state systems. The frequency-scanning capabilities of the Wright Group's MR-CMDS setup makes it well-positioned to achieve this aim. This forms the basis for Chapter 3.

The rest of this Chapter describes in detail 1L TMDs and their vertical heterostructures. It provides the basis to understand the materials physics that's presented in the rest of this dissertation. A short description of each Chapter follows the section on TMDs.

1.2 Transition metal dichalcogenide (TMD) semiconductors

1.2.1 Monolayers

1.2.1.1 Physical description

TMDs have a chemical makeup of MX_2 with the four most prevalent variations having the transition metal M=Mo or W and the chalcogenide X=S or Se. All four, namely MoS_2, WS_2, $MoSe_2$, and WSe_2 occur naturally in their bulk form as minerals albeit in varying abundances. The bulk structure consists of many layers stacked on top of one another and are held together by van der Waals (vdW) forces. Because there is no chemical bond between the layers, individual layers can be easily cleaved to form few-layer, bilayer (2L), and 1L structures. The chemical arrangement of 1L TMDs is shown in Figure 2.[15] The unit cell consists of the transition metal sandwiched between 6 chalcogens in a trigonal prismatic arrangement (Figure 2a) that is ~0.7 nm thick. This results in a hexagonal, honeycomb-like pattern with M and X atoms alternating when looking from the top-down (Figure 2b). The so-called armchair direction points along

alternating M and X atoms and the zigzag direction points along repeating M or repeating X atoms.

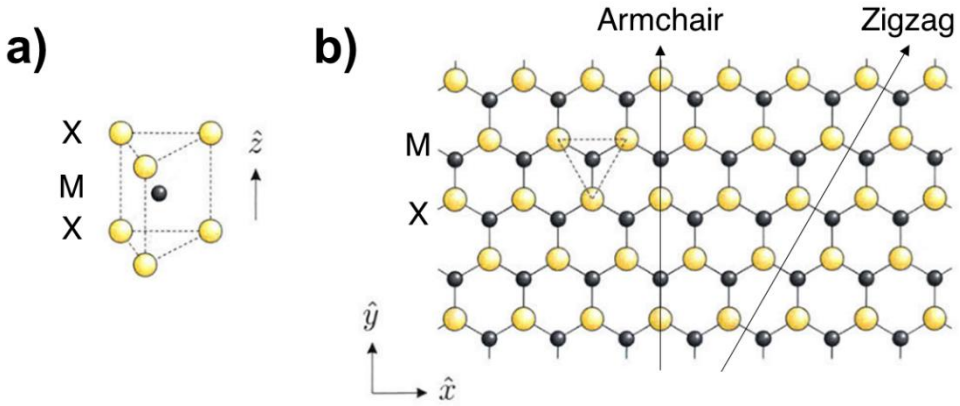

Figure 2 | Physical structure of 1L TMDs. a) the unit cell in a trigonal prismatic arrangement with six chalcogens surrounding the transition metal. b) top-down view with M and X atoms alternating to create a hexagonal, honeycomb-like pattern. The armchair and zigzag directions point along directions that follow alternating atoms or the same atom, respectively. Figure adapted from Ref 15.

As mentioned previously, the unit cell lacks an inversion center making 1L TMDs $\chi^{(2)}$ active. 2L TMDs in the 2H polytype, where the two layers are rotated 60° or "anti-aligned", does contain an inversion center and are thus not $\chi^{(2)}$ active. The other common polytype, 3R, consists of three layers that are aligned with a 0° twist angle but are translated with respect to one another, maintaining inversion asymmetry and making the 3R polytype $\chi^{(2)}$ active. The twist angle from 0-60° between successive TMD layers acts as an effective toggle of the structure's overall $\chi^{(2)}$,[16] which plays an important role in the transient SHG microscopy measurements in Chapter 2.

Two common ways of synthesizing 1L TMDs are through mechanical exfoliation and chemical vapor deposition (CVD). The Scotch-tape exfoliation method, popularized for synthesizing graphene from graphite,[17] is also a valid synthetic method for TMDs. Scotch-tape exfoliation is relatively cheap and readily accessible which makes it a more popular synthetic method over

chemical vapor deposition (CVD). A downside to the Scotch-tape method is the 1L regions are typically small (~10 μm x 10 μm areas) and obtaining a 1L is a stochastic process. Recently, an exfoliation method using gold tape rather than Scotch tape was shown to create large area 1L TMDs of high quality.[18] CVD grows the 1L TMD in well-defined orientations (i.e. epitaxially) that are controlled by conditions within a tube furnace.[19] While the setup required to perform CVD is more involved compared to exfoliation, the resulting structures are typically of higher crystalline quality.

1.2.1.2 Electronic/optical description

When an electron gets promoted from the valence band maximum (VBM) to the conduction band minimum (CBM) in a semiconductor, it leaves behind a positively charged hole that resides at the VBM. The electron and the hole are held together by the Coulomb force and the correlated pair are known as an exciton. The characteristics of excitons in TMDs are shown in Figure 3. Bulk TMDs have an indirect bandgap in the near IR and host loosely bound excitons. Material surrounds an exciton in all three dimensions in a bulk TMD which significantly screens the Coulomb attraction (Figure 3a, top).[20] When thinned down to a single layer, the bandgap becomes direct and there's a significant reduction in the Coulomb screening making the exciton tightly bound (Figure 3a, bottom). The optical bandgaps for MoS_2, WS_2, $MoSe_2$, and WSe_2 are all in the visible spectral range which plays a role in their popularity. The binding energy (the energy required to break apart the electron and hole) for 1L TMDs is ~320 meV whereas the binding energy for the bulk structure is ~50 meV.[20] The strong effect the binding energy has on the optical properties is demonstrated in the reflectance contrast spectrum of 1L WS_2 in Figure 3b. Given the morphology of the 1L WS_2 sample and its substrate, the reflection contrast spectrum is proportional to the absorption spectrum.

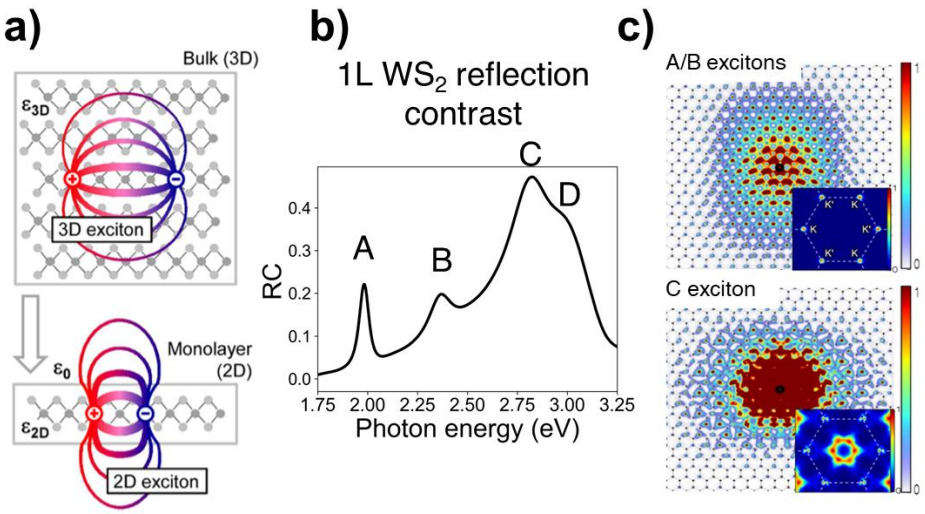

Figure 3 | Excitons in bulk and 1L TMDs. a) Cartoon of the Coulomb force bounding the electron-hole pair together, highlighting the reduced charge screening in the 1L case. b) reflection contrast spectrum of 1L WS_2 showing the A and B excitonic resonances separated from the continuum absorption as well as the C and D excitons on top of the continuum. The spectrum was taken with the hyperspectral nonlinear microscope constructed for this dissertation. c) real-space representation of the excitonic wavefunctions for the A/B excitons (top) and the C exciton (bottom). The insets show the momentum-space wavefunctions. Panel a) is adapted from Ref 20 and panel c) adapted from Ref 21.

The so-called A exciton, and to a lesser extent the B exciton, are separated from the continuum absorption in Figure 3b. The real-space representation of the A and B excitonic wavefunctions are shown in Figure 3c (top) over the crystal lattice. The inset shows the reciprocal-space, or momentum-space, representation of the A and B excitonic wavefunctions. The wavefunctions are highly localized in momentum space and, accordingly, delocalized in the real-space representation. The so-called C and D excitons are of a different nature than the A and B excitons which is demonstrated in the real- and momentum-space representations of the C exciton wavefunction in Figure 3c (bottom).[21]

These differences come about from where they originate in the Brillouin zone (BZ) which is shown in Figure 4 along with the band structure diagrams of the high symmetry points in 1L TMDs' first BZ. The first BZ is the natural way to think about solid-state systems due to their

periodicity. The first BZ for a hexagon in real space is a hexagon in momentum space and is shown in Figure 4a with the irreducible representation (red dashes) and the high symmetry points. The relevant high symmetry points are K, Γ, Q and M. The Γ point is the origin of the first BZ and has zero momentum. Therefore, in real space, the wavefunction that comprises the Γ point is delocalized across the entire unit cell (i.e. there's no periodicity).

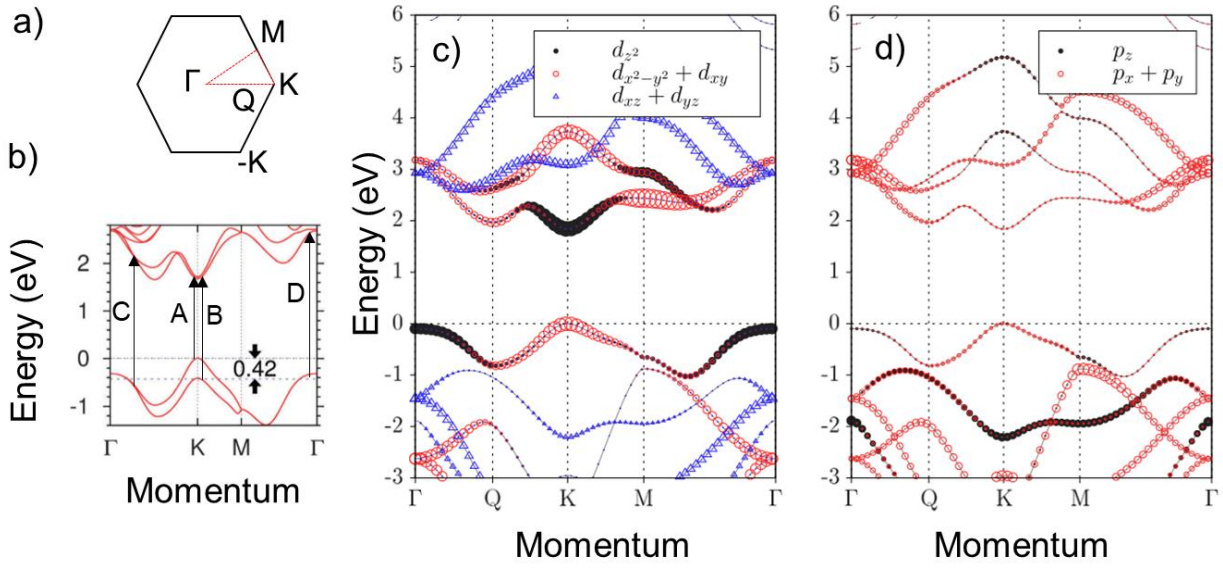

Figure 4 | Brillouin zone and band structure diagrams of 1L TMDs. a) hexagonal BZ labeled with the high symmetry points and the irreducible representation outlined in red dashes. b) band structure diagram of a representative 1L TMD with SOC considered. The arrows highlight the prominent transitions that are seen in linear spectra. c-d) orbital projection band structure diagrams for the *d* and *p* orbitals. The *d* orbitals play a dominant role in many of the optical transitions throughout the BZ while there is considerable *p* orbital character at the Γ point. Panel b adapted from Ref 22 and panels c, d) adapted from Ref 23.

There is prominent spin-orbit coupling (SOC) in TMDs due to the heavy transition metal atom. A band structure diagram describes the allowed energies at momentum points in the first BZ. A band structure diagram for a 1L TMD that incorporates SOC is shown in Figure 4b.[22] It is apparent that the A and B excitons originate from the same momentum point (the K point) at the

VBM and CBM but are separated in energy due to SOC. The K point houses the direct bandgap transition in TMDs and therefore is the most studied. The A and B excitons in Mo-based 1Ls are separated by ~200 meV and in W-based 1Ls they are separated by ~400 meV. The A and B resonances seen in the reflection contrast spectrum in Figure 3b are prominent due to the strong transition dipole from the direct-gap transition at the K point. The C and D excitons are prominent due to band nesting. Band nesting occurs when the slopes of two different bands match each other so that optical transitions at many momentum points fall within a small bandwidth of energy. The C exciton originates from nested transitions between the Γ and Q momentum points[21] and the D exciton originates from nested transitions at the Γ point.[23] The contribution from the *d* and *p* orbitals are projected onto the band structure in Figures 4c and 4d, respectively. The size of the symbol in the diagrams is proportional to the orbital population in the corresponding state. The direct bandgap transition at the K point, along with many other momentum points along the lowest-energy CB and highest-energy VB, are comprised of *d* orbitals of varying symmetry (Figure 4c).[24] The *p* orbitals play a reduced role in the number of transitions available near the band edge compared to the *d* orbitals, however there are considerable contributions at and near the Γ point (Figure 4d).

Ultrafast transient absorption (TA) spectroscopy is the dominant technique to measure population recombination dynamics in TMDs. In TA, an ultrafast pump pulse creates a carrier population in the material and an ultrafast probe pulse measures the absorbance at a well-defined time after the pump. Typically, the transmission or reflection of the probe is the measured quantity and the absorbance is calculated from it. The time delay between the pump and probe is stepped to create population decay traces. In 1L TMDs, the wide range of sample quality due to varying synthetic methods, sample age, and supporting substrate can make interpretation of the population

recombination dynamics ambiguous. However, there are some common trends. The recombination dynamics generally consist of a fast and slow component and are fit to a biexponential decay. The fit is phenomenological but the extracted time constants get mapped to physical processes that help paint an intuitive picture for carrier relaxation. The fast component typically has a time constant of a couple picoseconds (ps) or less. In a high carrier-density regime (large pump fluence), the fast decay is attributed to exciton-exciton annihilation[25] that has a linear dependence on the pump fluence and biexciton formation[26,27] that has a quadratic dependence on the pump fluence. At long delay times and low carrier concentrations, radiative recombination is the dominant relaxation pathway. It has a time constant of a few 10s of ps and is independent of charge carrier density, which is corroborated by both theory and experiment.[28,29] Even at low carrier densities, defects such as atomic vacancies, atomic substitution, and grain boundaries can dominate over radiative recombination and speed up the relaxation process. Finally, optically dark states can compete with radiative recombination on both fast and slow time scales.[30,31] The probability of populating optically dark states increases at elevated temperature where carriers are more likely to scatter with a phonon to a different momentum point.

1.2.1.3 Applications

1L TMDs can host excitons at both the K and -K momentum points (-K point is shown in Figure 4a). They are energetically degenerate. The magnetic quantum numbers of electrons and holes that comprise excitons at the K point are the opposite sign to that of excitons at the -K point.[32] This gives rise to distinct optical selection rules and related spin-valley properties of excitons populated at these momentum points. Pumping 1L TMDs with one handedness of circularly polarized light creates excitons only at the K point, while circularly polarized light of the

opposite handedness creates excitons only at the -K point.[32,33] This aspect of TMD excitons was not discussed earlier in the introduction because the experiments in this dissertation use linearly polarized excitation beams which excites an equal proportion of excitons at the K and -K points. Personally, however, I think the most intriguing application of 1L TMDs is in devices that use spintronics/valleytronics. Spintronics (valleytronics) utilizes the spin state of an electron (the valley at which an electron resides) to encode and process information. This gives devices multiple degrees of freedom, in addition to the charge of an electron, to perform typical electronics operation such as logic and memory. The coherent control of spin- and valley-specific charge carriers in 1L TMDs makes them an attractive material for the realization of spintronic and valleytronic devices.[34–36]

1.2.2 Heterostructures

1.2.2.1 Physical description and electronic structure

TMDs of differing chemical composition can be combined to create a heterostructure (HS) which is shown schematically in Figure 5.[37,38] The figure shows different transition metals but HSs can also be made with different chalcogens or with a different transition metal and a different chalcogen. A 1L TMD stacked on top of another 1L TMD creates a vertical HS which is referred to as a heterobilayer (HBL) hereafter (Figure 5a, left). The vertical stacking arrangement creates

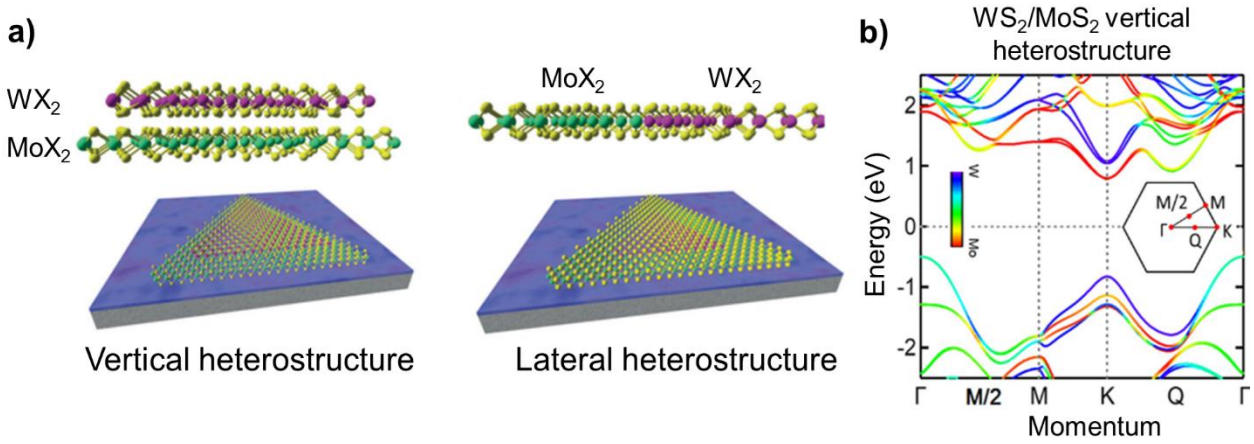

Figure 5 | Stacking arrangements and electronic structure of TMD HSs. a) the two types of HSs which comprise two different 1L TMDs. Vertical HSs (left) create a 2D interface and laterals HSs (right) create a 1D interface. Note the figure shows the transition metal changing, but HSs can also be created by changing the chalcogen or both the transition metal and the chalcogen. b) band structure diagram for a WS_2/MoS_2 vertical HS. The color of the bands represents the relative contribution of the WS_2 and MoS_2 orbitals that comprise the band at the corresponding momentum point. Note the VBM and CBM at the K point reside in different layers. Panel a) adapted from Ref 37 and b) adapted from Ref 38.

a 2D interface. Like the bulk homostructures, the constituent layers in a HBL are not chemically bonded but are held together by vdW forces. This relaxes the synthetic constraint so TMD HBLs can be created through mechanical exfoliation of both layers and manually stacking one 1L on top of the other. TMD HBLs can also be synthesized using CVD.

Lateral HSs are more synthetically involved than their vertical counterparts. Instead of a 2D interface, lateral HSs have a 1D interface where the different TMDs are chemically bonded to one another (Figure 5a, right). The atomically sharp interface provides a higher degree of coupling than the vertical HSs that are held together by weaker vdW forces.[39] To properly interrogate the 1D junction, near-field spectroscopy and microscopy techniques are needed (I note that the Wright and Jin group recently published a paper using routine spectroscopic characterization methods to learn about alloying in a lateral HS. Those experiments had few-micron spatial resolution[40]). Unsurprisingly, the more involved synthetic and optical characterization methods of lateral HSs make them much less studied than vertical HSs. Any measurements performed on a TMD HS in this dissertation are on vertical ones. As such, the following discussion regarding the band structure, optical characteristics and the applications only pertains to vertical HSs.

The band structure for a WS_2/MoS_2 HBL is shown in Figure 5b. The color of a band at a given momentum point represents the relative WS_2 and MoS_2 orbitals' contribution to the orbitals that comprise that band. Blue means the band is completely WS_2 in character and red means the band is completely MoS_2 in character. There are three important characteristics to point out in the band structure: 1) at the K point, the VBM resides in the WS_2 layer and the CBM in the MoS_2 layer. This band alignment is known as Staggered or a Type II band alignment; 2) the VBM at and near the Γ point is higher in energy than the VBM at the K point, making the HBL an indirect gap semiconductor; 3) a few of the high symmetry points like the Γ, M/2, and Q points are hybridized between the WS_2 and MoS_2 layers (i.e. the highest-energy VB or lowest-energy CB at these momentum points is light blue, green or yellow; see colorbar in Figure 5b). This has implications

for charge carriers transferring between the layers which will be discussed in the following section and Chapter 3.2.

1.2.2.2 Optical characteristics

When an exciton is created at the K point in the layer with the lower-energy bandgap, either the electron or hole will funnel to the lowest energy configuration (whether the electron or hole transfers is determined by the relative band energies). A cartoon of this situation for Type II band alignment in a generic HBL is shown in Figure 6a. Type II band alignment occurs for any HBL combination that is composed of the four main TMDs in this dissertation. The pump selectively creates an exciton in TMD 1 but not TMD 2 as the pump energy is too low to create carriers in TMD 2. Due to the energy offset between the layers' CBMs, the electron will transfer from TMD 1 to TMD 2. This process is called charge transfer (CT) and it was first discovered in a WS_2/MoS_2 HBL in 2014.[41] Figure 6b shows a spatial representation of CT. When pumping the

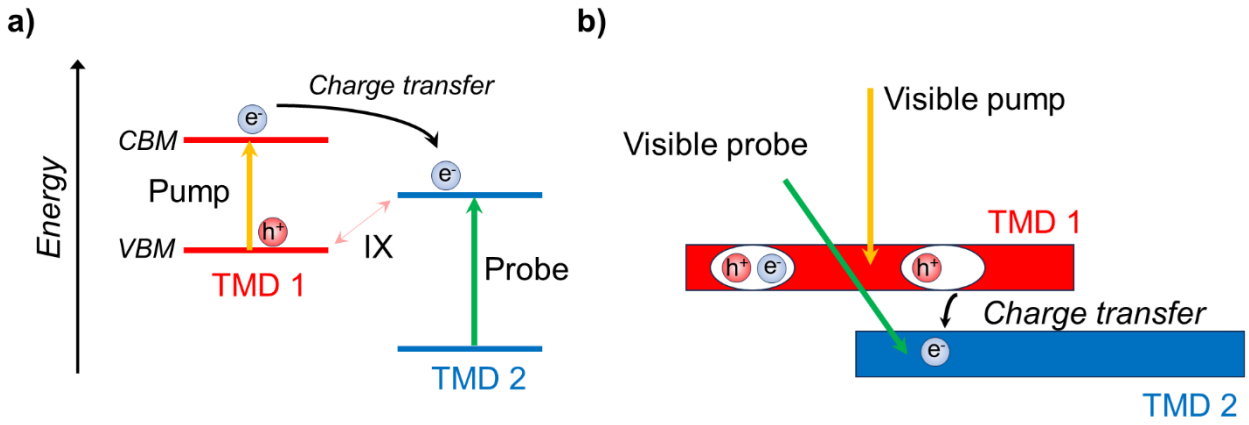

Figure 6 | Charge transfer schematic in TMD HBLs. a) band energy representation showing a staggered/Type II band alignment. Excitons are selectively created in the TMD with the lower-energy bandgap. The energy offset between the CBMs of the TMDs drives the electron to transfer from TMD 1 to TMD 2. b) spatial representation of the electron transferring from TMD 1 to TMD 2.

lower-energy-bandgap material, a photoinduced bleach at TMD 2's A exciton energy is indicative of CT occurring in the HBL. On the flip side, if TMD 2 hosts an exciton, then the electron remains in TMD 2 and the hole transfers to TMD 1 due to the band energy offset. At room temperature, CT occurs on an ultrafast timescale that is typically shorter than the temporal resolution of fs-pulsed TA spectroscopy experiments (< ~30 fs). This ultrafast time scale is independent of stacking angle between the two layers,[42] the reason for which is discussed in detail in Section 3.2.1.

After CT occurs, the free electrons in one layer are attracted to the free holes left behind in the other layer and create an interlayer exciton (ILX; Figure 6a, pink arrow). ILXs have an energy equal to the VBM and CBM of the entire HBL system and are therefore lower in energy than the *intralayer* A excitons of both layers. ILXs create a transient dipole across the 2D interface which has been shown to increase the asymmetry of the system by enhancing the HBL's $\chi^{(2)}$.[43] Relative to intralayer excitons, the wavefunction overlap of excitons and holes comprising ILXs is small, which results in a weaker oscillator strength. A PL trace for a WS_2/MoS_2 HBL is shown in Figure 7a (middle trace).[38] The ILX emits around 1.5 eV and the PL intensity is significantly weaker compared to the lone WS_2 and MoS_2 A exciton PL intensities (Figure 7a, top and bottom traces). It's rare to see ILX photoemission at room temperature; a sample temperature near LN_2 or colder is often required to see discernible ILX photoemission.

Another defining characteristic of ILXs is their lifetime. Figure 7b compares TA traces for ILXs in two HBL samples with twist angles between the layers of 60° and 0° (green circle and blue diamond traces).[44] A considerable amount of TA signal remains for both HBLs even at a pump-probe delay of 1 ns whereas the TA signal drops to 0 at a pump-probe delay of <200 ps for the pure 1L (black triangle trace). The long-lived nature of the ILX is seen in most TMD HBL

combinations, however that's not the case for $WS_2/MoSe_2$ which has ILX lifetimes similar to intralayer exciton lifetimes.[45]

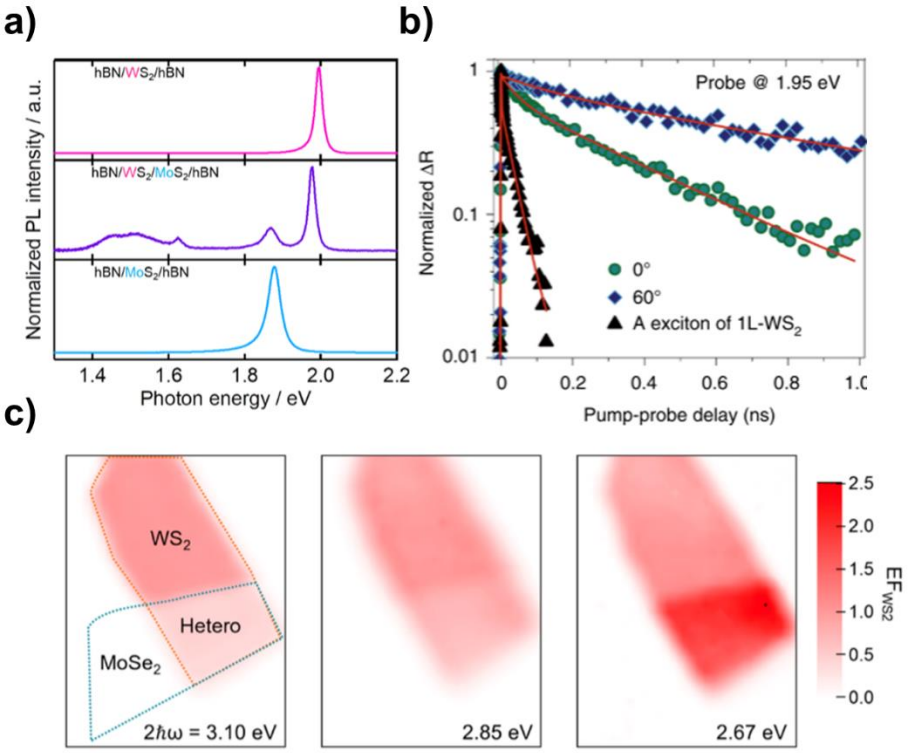

Figure 7 | Unique optical phenomena in TMD HBLs. a) PL comparison between a WS_2/MoS_2 HBL (~1.5 eV, purple trace) and the individual 1Ls (pink and blue traces) highlighting the weak oscillator strength of the ILX. b) TA transients comparing the ILX in two WS_2/WSe_2 HBLs of differing twist angles to the intralayer exciton in 1L WS_2, highlighting the long-lived nature of the ILX. c) SHG enhancement images of a $WS_2/MoSe_2$ HBL with 3 different output SHG energies, illustrating the effect that excitonic resonances in one layer has on the SHG properties of the other layer. Panels a, b, c adapted from Refs 38, 44, and 46, respectively.

Finally, another optical characteristic of TMD HBLs worth mentioning is how the output SHG intensity varies as a function of its frequency which is illustrated in Figure 7c.[46] In these SHG images, the polarization setup is such that any SHG from the $MoSe_2$ layer is rejected and only SHG from the WS_2 layer is detected. Because the polarization setup only allows SHG photons from the WS_2 layer to reach the detector, this gives a clear picture on how the $MoSe_2$ layer

affects the SHG originating from the WS_2 layer in the HBL region. The HBL region is labeled as "Hetero" in Figure 7c (left image). The red colorbar plots the enhancement factor (EF) which is calculated by dividing the SHG intensity values within a region by the average SHG intensity in the pure WS_2 region. Thus, the EF for the pure WS_2 region is always 1 and the EF for the pure $MoSe_2$ region is always 0, which is reflected in all three images. The only region whose EF changes is the HBL region. As the SHG output energy gets closer to the $MoSe_2$ C exciton energy (2.67 eV), the EF of the HBL region increases, meaning that the WS_2 layer is resonantly enhanced by the $MoSe_2$ C exciton. This highlights the role that excitons in one layer have on the SHG intensity of the other layer, which will be important to consider in Chapter 2.3.1.

1.2.2.3 Applications

Charge readily separates in TMD HBLs due to their Type II band alignment which, along with their efficient light absorption, makes them attractive materials to use in solar cells. However, the binding energy of the ILX has caused the power conversion efficiency in TMD-based photovoltaics devices to remain below their calculated theoretical limit.[47] Thus, the applications most suitable for TMD HBLs lie in electronic and optoelectronic devices.

When one layer in a TMD HBL is n-doped and the other is p-doped, an atomically thin p-n junction is created which exhibits different charge transport characteristics than the bulk version.[48] Regarding spin and valleytronics applications, the spin-valley polarization of excitons in 1L TMDs only lasts up to a few ps which makes them more suited for *coherent* manipulation of the spin states.[49] ILXs have been shown to preserve spin-valley information on much longer time scales making TMD HBLs an attractive material system for spin and valleytronics applications where longer duration of spin-valley polarization is required.[50]

1.3 Remaining thesis structure

With the relevant spectroscopy and materials background established, the rest of this dissertation includes three chapters:

- The next chapter discusses the motivation for the Wright Group building a nonlinear microscope to investigate the spatially resolved photophysics in 2D materials. It goes over the design principles for the key components that comprise the microscope and ends with a manuscript intended for publication that includes measurements taken by the nonlinear microscope, which is the culmination of the microscope project.
- The following chapter details the Wright Group's efforts to characterize TMDs at optical transitions that do not arise from the direct bandgap transition. We perform SFG spectroscopy on a variety of TMD samples and evidence resonance enhancement from high-lying CB states. Simple simulations corroborate the experimental results. We then use the SFG output as a probe in pump-SFG probe spectroscopy to investigate the CT mechanism in TMD HBLs.
- The final chapter presents natural extensions of the work discussed in the two preceding chapters. We discuss a modification to the nonlinear microscope's image acquisition strategy so the instrument is well-suited to perform more conventional pump-probe microscopy measurements that utilize a linear probe, in addition to it already being well-suited for nonlinear probes like SHG and SFG. Regarding the SFG measurements, we discuss experiments that would further confirm the peak assignment for the novel high-energy CB state we see in 1L WS_2. Finally, we propose using a well-known variation of pump-probe spectroscopy to more directly interrogate the dynamics of the high-energy CB state.

2 Widefield Nonlinear Microscopy

Integrating a widefield nonlinear microscope into the Wright Group's CMDS setup on the fs system was the primary project I worked on in graduate school. It was the most challenging yet most rewarding project I worked on due to its complexity in both the technical and logistical aspects. Section 2.1 uses examples from the literature to motivate the Wright Group's desire to build such an instrument. Section 2.2 details my thought process for designing the key microscope components. Finally, Section 2.3 is a manuscript for proof of principle measurements taken with the widefield microscope on exfoliated TMD HBL samples, accompanied with the Supporting Information for the manuscript. I plan to publish the manuscript in the near future.

2.1 Motivation for spatially resolved measurements on 2D materials

2.1.1 Heterogeneities

The primary motivation for doing spatially resolved CMDS experiments is due to the heterogeneities in the 2D materials that the Wright Group studies. There are different classes of heterogeneities, some that are unavoidable and some that are designed. The former class comes from undesired sources like imperfections that result from the synthesis of the materials, both through non-epitaxial methods like the well-known Scotch-tape exfoliation method and epitaxial methods like CVD. Common imperfections are cracks and bubbles in the crystal lattice,[51,52] lattice strain, atomic vacancies, atomic substitutions,[53] alloying,[40] and charge doping.[54] These imperfections typically lead to electronic/optical properties that are less desirable than the pristine material. However, depending on the desired material properties for a given application, the "undesired" defects may become "desired" where synthetic conditions favor a particular defect as it improves device performance.[53]

The other class of heterogeneities in 2D materials comes from directed fabrication of HSs.[55] As stated in the introduction chapter, HS interfaces (2D interface for vertical, 1D interface for lateral) give rise to interesting materials physics and have applications in next-generation electronics and solar cells. Thus, it's crucial to correlate the optical and electronic properties to specific points along the sample. Doing ensemble measurements where the spectroscopic signal is spatially averaged is not sufficient when studying this class of materials. An example that combines both discussed types of heterogeneities (inherent material defects and HS fabrication) is a 2L WS_2/graphene vertical heterostructure studied by transient absorption microscopy (TAM)[56] and is illustrated in Figure 8.

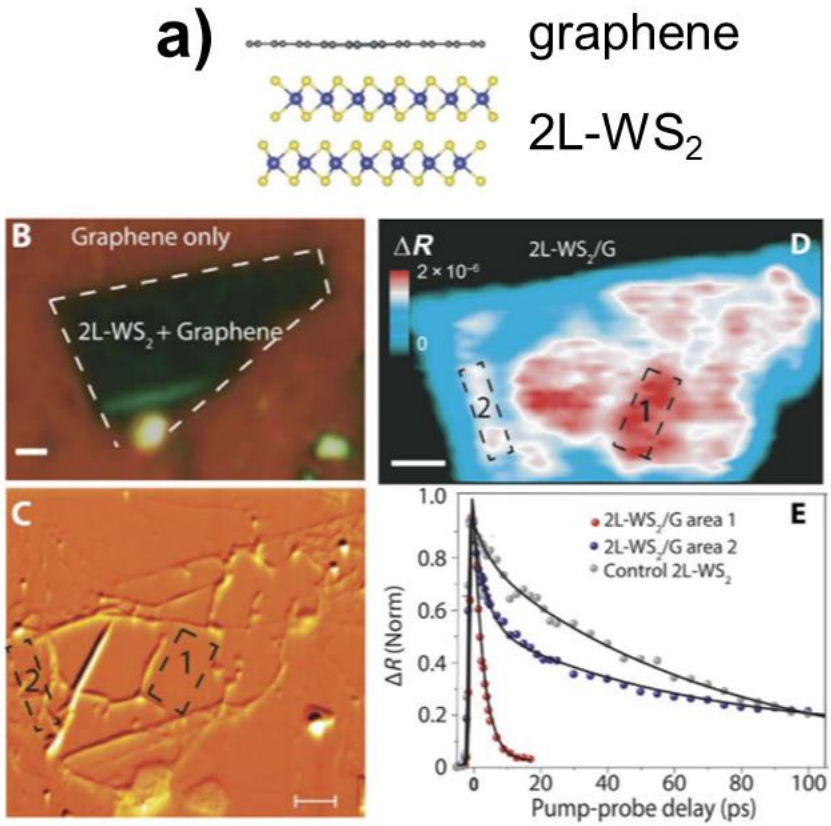

Figure 8 | 2L WS_2/graphene HS that highlights spatial heterogeneity. a) side-on chemical schematic, b) optical micrograph, c) AFM height map, d) TAM map, and e) spatially correlated delay traces. Scale bars are 1 μm. Figure adapted from Ref 56.

A standard optical micrograph (Figure 8b) erroneously shows a mostly homogenous sample. When viewed through the lens of an AFM height map (Figure 8c) or a TAM map (Figure 8d), however, heterogeneities are readily seen. These heterogeneities are a result of both imperfections inherent to the parent crystals and imperfections that get introduced during sample fabrication. Furthermore, dynamics reported in Figure 8e tell two completely different stories when it comes to heterostructure behavior: the transient signal in Region 1 dies off completely within 20 ps, indicating efficient charge transfer and strong interlayer coupling whereas Region 2 has dynamics that more closely resemble the control 2L WS_2 sample. Had this been an ensemble

measurement, the two drastically different responses would have averaged out and the nuance that the spatially resolved measurements brought to the researchers would've been lost.

The above study has heterogeneity from stochastic processes during crystal growth and sample fabrication which leads to defects on a highly variant spatial scale. There are methods of crystal growth and HS fabrication that are more controlled which result in the dominant form of heterogeneity within a sample to be *between* different HS domains rather than *within* a single domain. An example of this inter-domain heterogeneity is illustrated in Figure 9.[57]

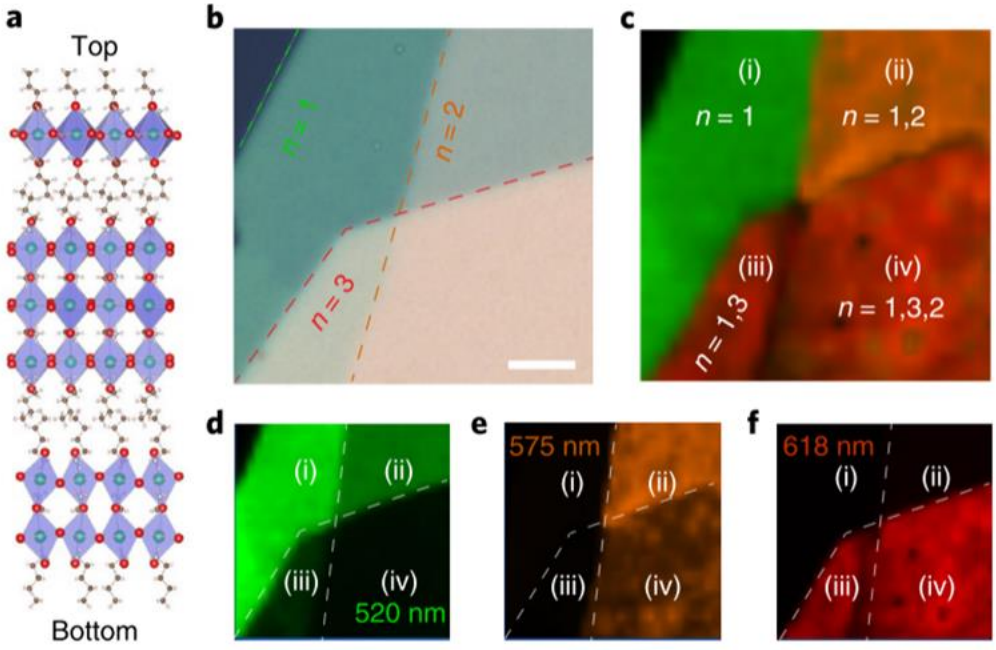

Figure 9 | Characterization of 3-layer 2D RP perovskite heterostructure. a) schematic for the layer stacking of the heterostructure, b) optical micrograph, c-f) spectrally integrated PL mappings. c) composite PL map, d) PL map integrated from 515-525 nm, e) PL map integrated from 570-580 nm, f) PL map integrated from 613-623 nm. Figure adapted from Ref 57.

The sample is a 3-layer 2D Ruddlesden-Popper (RP) lead halide perovskite with each layer constituted from quantum wells of varying thickness (i.e. *n* number, Figure 9a). The degree of heterogeneity in the optical micrograph (Figure 9b) is similar to the degree of heterogeneity that is seen in the spectrally integrated PL composite image (Figure 9c). The composite image is constructed from the individual PL maps (Figures 9d-f). The *intra*-domain heterogeneity is a lot less dramatic compared to the example in Figure 8. The interesting materials physics in this heterostructure sample comes from the vertical stacking of 2D perovskite layers. Differentiating the heterostructure regions by their *inter*-domain heterogeneity is thus crucial and, again, would be lost in the case of an ensemble spectroscopic measurement. The PL measurement in this example is straightforward experimentally. A nonlinear microscope in the Wright Group would aim to use more involved spectroscopic methods (pump-probe spectroscopy and MR-CMDS) while getting the more routine measurements (like PL or static SHG) for free, allowing both basic and advanced characterization of novel 2D materials.

2.1.2 Unique microstructures (synthesized by Jin group)

The examples provided in section 2.1.1 are non-epitaxial structures and thus have less stringent synthetic conditions to realize the interesting interface phenomena. There's another type of sample heterogeneity that's a result of more involved synthetic methods which the Jin group at UW-Madison, the Wright Group's primary synthetic collaborators, specializes in. More specifically, they are screw-dislocation spirals of TMDs where differences in the stacking configuration leads to differences in the electronic structure of nearby layers and is illustrated in Figure 10.[58]

The top row of Figure 10 contains AFM images for three stacking configurations where the layers have a 0° stacking angle (Figure 10a), a 60° stacking angle (Figure 10c), and a mix of 0°

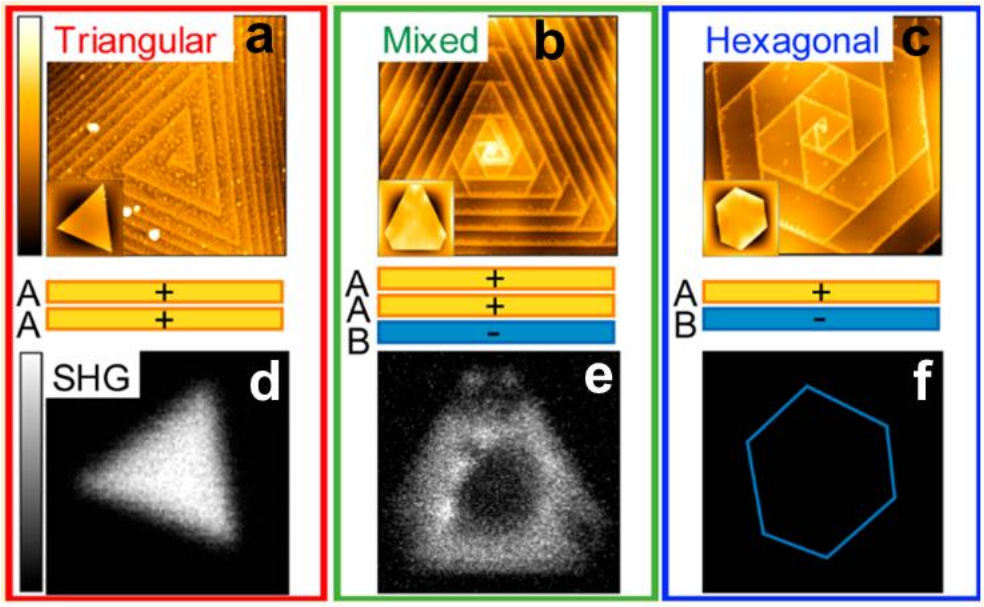

Figure 10 | Screw-dislocation spirals of TMD microplates. Top row is AFM maps and the bottom row is SHG intensity maps. a, d) is for triangular stacking, b, e) is for mixed stacking, and c, f) is for hexagonal stacking. Figured adapted from Ref 58.

and 60° stacking angles (Figure 10b). Figure 10d-f displays the corresponding SHG image for the three stacking configurations. It is apparent there is a structure-function relationship between stacking configuration and SHG intensity.

The SHG behavior of the three stacking configurations likely could've been predicted based on previous exfoliated 1L and 2L TMD SHG studies. However, it's much less clear how the time-dependent photophysics (i.e. pump-probe response) depends on the stacking configuration and if there's a meaningful dependence on the structure thickness. There may also be a difference between stacking configurations in the response of a fully coherent CMDS experiment that is resonant with an out-of-plane vibrational mode and probes the vertical stacking interactions. It's

these sorts of inquiries and questions that were being asked in the Wright Group when I joined and is the motivation for building a nonlinear microscope.

2.2 Design considerations for building a widefield nonlinear microscope

2.2.1 Excitation geometry

How the excitation beams are prepared prior to interrogation of the sample is a crucial aspect to consider when building a multibeam microscope as they will either directly generate the detected output (for a homodyned experiment) or will be detected by mixing the output with a local oscillator and Fourier transforming the resulting fringes (for a heterodyned, interferometric measurement). The excitation beams can either be collinear where they occupy the same beam path or noncollinear where the beams do not take the same path to get to the sample. The dilemma is the same for spatially averaged spectroscopic measurements where one needs to consider how they will isolate the signal of interest. Solid state materials at room temperature have strong electronic transition dipoles but dephasing times (10s of fs) that are shorter than the excitation pulses used on the fs system in the Wright Group. Thus, most nonlinear spectroscopies done on solid state materials are done at pulse overlap where all possible spectroscopic pathways will generate output. These output beams may be the same color or have the same polarization dependence as one another. The signal beams may also share color and polarization dependencies with the excitation beams; either scenario makes nonlinear signal isolation difficult. Nonlinear spectroscopy is mostly performed in the time domain where, by necessity, the experimentalist has control of the excitation pulse's phase and can use phase cycling to isolate the signal of interest.[59,60] Frequency domain experiments do not require shot-to-shot

phase stability and don't need phase control of excitation beams. They utilize a noncollinear excitation geometry where the output beams are generated at angles defined by phase matching. The output beams are spatially coherent. Changing time delays will then separate pathways that have the same phase matching dependence. Thus, nonlinear signal isolation requires phase cycling if using a collinear beam geometry. Phase cycling is not required if using a noncollinear beam geometry.

In theory, converting a nonlinear spectroscopy setup into a nonlinear microscope is straightforward: place a microscope objective into the beam line to magnify the image and figure out a means to extract spatial information. Two common ways to extract spatial information are with raster scanning or widefield excitation and schematics of both are shown in Figure 11 along with an example excitation geometry employed by Wright Group spectroscopy experiments on semiconductors. Raster scanning setups use either a static beam with an *xy* sample scanner or galvanometric mirrors that scan the beams across a stationary sample. Raster scanning setups only need a single pixel detector as the spatial information comes from scanning the beams/sample. The beam size provides the spatial resolution and is therefore small relative to the sample (Figure 11b). A widefield setup illuminates the entire sample (Figure 11c) and the light is routed to a 2D array detector which provides the spatial information. There are advantages and disadvantages to both geometries. Significant factors that inform on the optimal geometry include available beam intensity, sample degradation, and scan time. Many nonlinear microscopes in the literature utilize a collinear beam geometry and use either raster scanning[44,61,62] or widefield[60] configurations to extract spatial information.

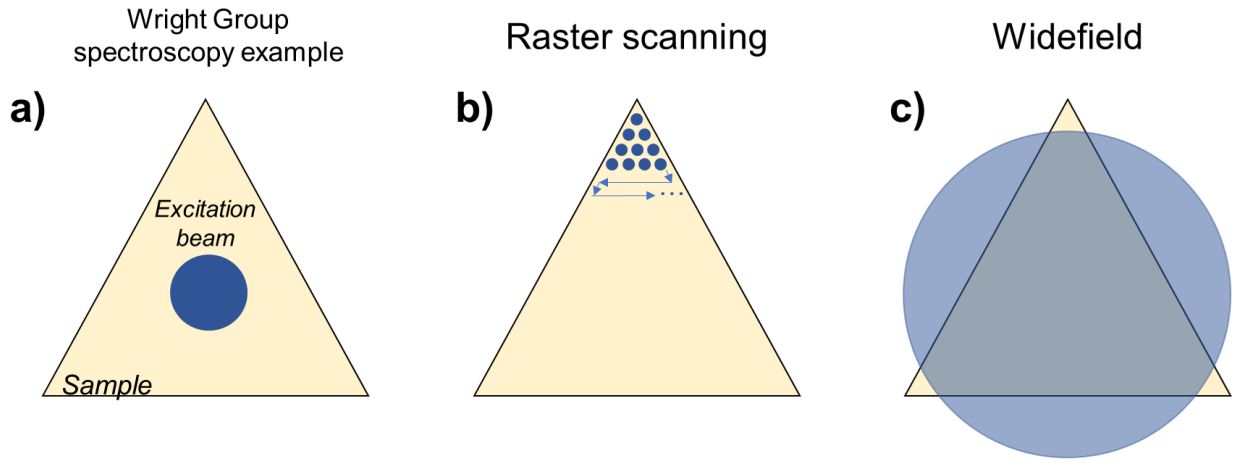

Figure 11 | Schematic of various spectroscopic excitation geometries. Relative beam and sample sizes for a) an example of Wright Group spectroscopy on semiconductor samples, b) a raster scanning microscope, and c) and widefield microscope.

Nonlinear microscopes that utilize a noncollinear excitation geometry are much less common in the literature. The Wright Group, being a frequency domain multidimensional spectroscopy group, does not have phase control of the excitation pulses and extracts its nonlinear output through a noncollinear excitation geometry. Thus, the natural extension for creating a nonlinear microscope in the Wright Group is to use a noncollinear beam geometry as the Group doesn't readily have the infrastructure to perform phase cycling. We chose to use a 2D array detector (camera) since that also gives the microscope the capability to do spectrally resolved measurements (by placing a diffractive element in front of the camera, see Section 2.2.3). Using a single pixel detector with a sample scanner can only give spectral resolution with the addition of a monochromator, and sending multiple beams through a galvanometric scanner is needlessly complex. Using a camera for a detector then necessitates widefield excitation.

Widefield excitation simply means the entire field of view is excited at a single time, it doesn't give any information as to how wide the field needs to be. Beam size will be determined by the

lateral extent of the sample. For the materials side of the Wright Group, the largest interrogated samples are in the 250-500 μm range. Depending on the wavelength of light and focal length of the focusing optic, this beam size can be achieved at the focus or ahead of/behind the focus. This microscope uses primarily visible/NIR light and would need focal lengths in the ~1 m range to achieve a big enough beam size (250-500 μm). Due to space constraints on the optical table, the focal lengths of the excitation optics were constrained to 100-200 mm. Thus, to achieve the desired beam size, the beams interrogate the sample *after* progressing through their focus. A schematic of the excitation geometry is shown in Figure 12. The noncollinear beam geometry in conjunction with defocused excitation is what makes this nonlinear microscope unique as there are not many, if any, examples of this type of microscope in the literature.

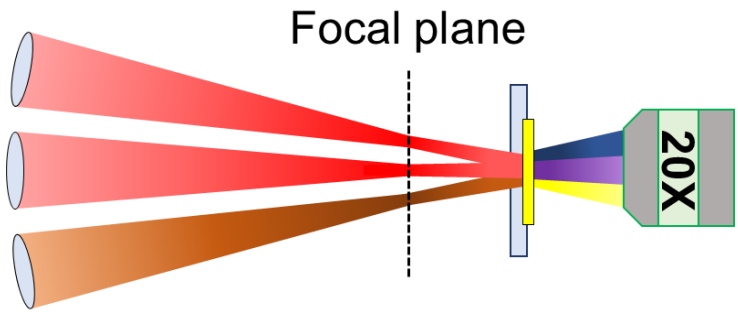

Figure 12 | Widefield non-collinear excitation geometry. Each beam passes through its focus, expands and then interrogates the sample. A long working distance objective collects all excitation beams and generated signal beams.

2.2.2 Imaging objective

The primary consideration when choosing an objective in the context of a multibeam, ultrafast microscope is if it has any adverse effects on the excitation beams. Reflective and refractive objectives have markedly different constructions and are shown in Figure 13. Ultrafast pulses traveling through a large amount of glass in the case of a refractive objective will severely distort the pulse (e.g. 50 fs pulses traveling through 100 mm of BK7 glass will stretch to ~250 fs[63] and obfuscate the temporal information in the measurement). However, if the output signal is collected through a refractive objective *after* the beams have interacted with the sample, then a refractive objective will suffice and is the configuration implemented in the proof of principle measurements in Section 2.3.

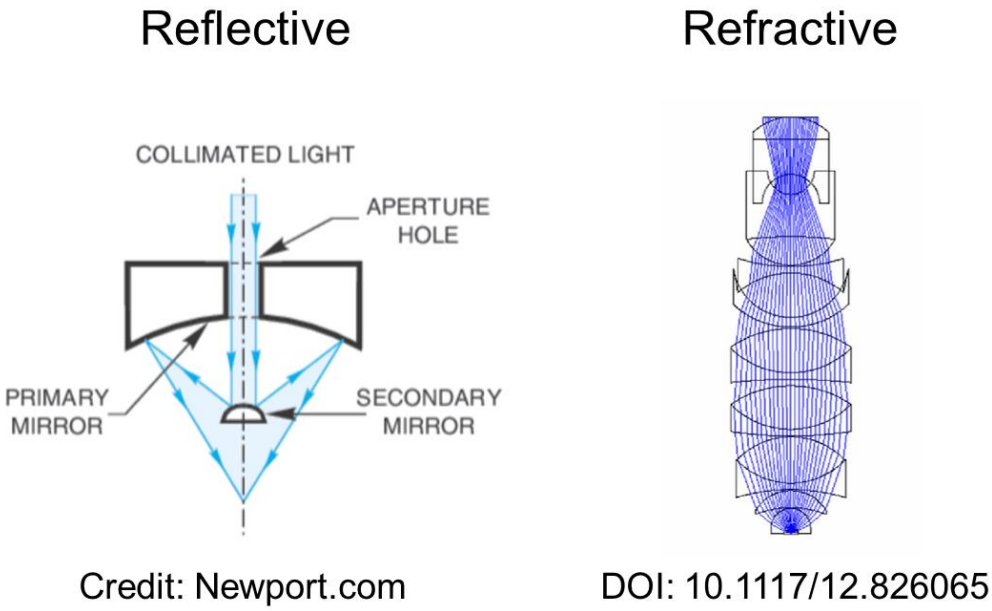

Figure 13 | The two primary types of microscope objectives. A reflective (Schwarzchild, Cassegrain) objective is shown on the left and a refractive objective on the right.

While the physical footprint of the Wright Group's nonlinear microscope can accommodate both transmissive and reflective excitation geometries, the instrument is better suited to a transmissive geometry. This constraint is primarily influenced by the difficulty of using a reflective objective in either reflection or transmission. There are two concerns when using a reflective objective in transmission (i.e. input beams enter and output beam exits on opposite sides of the objective). The first is preparing the excitations beams such that the phase matching condition directs the nonlinear output past the secondary mirror while still hitting the primary mirror (Figure 13, left side). There's a *ring* of acceptable output angles. Common rings of acceptance are 12-25° and 15-25° for Newport and ThorLabs reflective objectives, respectively. This range of angles is large compared to output angles for typical Wright Group experiment on the fs system which are ~1.5°. The second concern comes into play when the nonlinear output makes it past the secondary mirror. If the beam isn't traveling at an angle that matches the numerical aperture of the objective, the beam will not reflect off the primary and secondary mirrors properly and will not make it out of the objective. Even if the beam does make it out of the back aperture, the likelihood it will be traveling in such a direction that allows it to hit the tube lens within the pupil distance is low (pupil distance of ~100 mm is common for infinity-corrected objectives). If the Wright Group only did one type of spectroscopy (e.g. CARS, transient grating, triple sum frequency) with a narrow range of colors, then calculating the necessary input angle and aligning the microscope could be well worth this configuration. However, the Wright Group uses many different spectroscopies with a wide color range which means using noncollinear excitation in a transmissive geometry using a reflective objective is prohibitively tedious.

With noncollinear beams in a reflective excitation geometry (i.e. input beams enter and output beam exits on same side of the objective) there are again two points of concern. The first one is

the same as the first concern in the transmissive geometry: the nonlinear output must make it past the secondary mirror which constrains the input beams' angle of incidence. The second concern has to do with the small clear aperture of Cassegrain objectives (the most common reflective objective type) which, for popular optics suppliers, is less than 10 mm. Preparing the excitation beams to be travelling parallel to one another within such a tight diameter is nontrivial with standard optics. One method, which was attempted during prototyping stages of the microscope construction, is to use a telescope to shrink the bunch of beams by the proper amount to fit into the back aperture. For example, a 5:1 telescope could be used to shrink a beam bunch separated by 25 mm that needs to fit into a 5 mm back aperture. In theory this will work but in practice the alignment is nontrivial. Concave mirrors used in the telescope, if not aligned perfectly, will introduce aberrations such as astigmatism to the excitation beams. Any issues introduced in the telescope will get compounded when hitting the highly curved primary and secondary mirrors in the Cassegrain. This leads to a messy spatial intensity profile at the sample. Using lenses to create the telescope would be a viable option for doing measurements where temporal resolution is not a factor. This leads to the conclusion that when one wishes to use a reflective objective to do nonlinear microscopy, they'd be right to use a *collinear* beam geometry exciting from the *epi* direction.

Using a refractive objective solves many of the issues discussed in the previous paragraph. While there are many lenses that comprise a refractive objective (Figure 13, right side), each lens makes minor adjustments to the beam path compared to the highly curved primary and secondary mirrors in a reflective objective. Furthermore, there's no secondary mirror in a refractive objective which greatly relaxes the phase matching constraints as the objective collects all angles that fall within its numerical aperture. A downside to using a refractive objective, however, is

chromatic aberration. Fortunately, many refractive objectives are achromatic over a bandwidth large enough to accommodate many spectroscopic experiments. The relative ease with which to use a refractive over a reflective objective is the reason for using a refractive objective as the primary imaging optic in the nonlinear microscope.

2.2.3 Imaging spectrograph

Spectrally resolved measurements are at the core of the Wright Group's research efforts so adding a spectral dimension to the nonlinear microscope was always part of the plan. Because we knew significant financial resources were needed for a state-of-the-art camera to function in ultra-low light conditions (see Section 2.2.4), we decided to pursue a more frugal route regarding adding a spectral dimension to the microscope by making a homebuilt imaging spectrometer.

The first step in the design process when building an imaging spectrograph is the wavelength dispersing element. For this there are two options: a prism or a grating. Prisms are less expensive, have higher throughput, and do not suffer from common grating issues such as ghosting and spectral overlap between neighboring diffraction orders. However, prisms have ~10x lower resolving power than gratings[64] and do not provide as much versatility in the dispersive profile as they are constrained by the index of refraction of the material they're made of. There are many types of gratings that differ in the number of lines/mm, blaze angle, and blaze wavelength that will satisfy many optical applications. The final consideration in deciding between a prism and grating is how uniform the colors are spread across a large wavelength range. Prisms disperse blue colors at greater angles than they do for red colors. For gratings, the angular dispersion is more uniform for all colors. For the Group's microscope, we desired to disperse the entire visible spectrum across a relatively small CCD active area. This means the dispersion will be small on average but would be even smaller for red wavelengths if a prism is

used for the wavelength dispersing element. To avoid any issues attempting to resolve excitonic features that are in the red part of the visible spectrum we decided a grating would better suit our needs. Overall, due to the more uniform dispersion profile, large variety to choose from, and the fact that copies of master gratings are only slightly more expensive than prisms, we opted to use a grating over a prism.

The next design choice is to choose a reflection or transmission grating. The primary difference between the two types of gratings is reflection gratings have a thin metal film deposited on the ruled substrate to act as the reflective surface, whereas a transmission grating has the ruling etched directly onto the substrate. Reflection gratings are much more common because they can fold the optical path making the instrument footprint small and can accommodate large angles of diffraction, i.e. high groove densities. Transmission gratings, due to total internal reflection at large angles of diffraction, excel at modest groove densities of ~1000 lines/mm or lower. Transmission gratings generally have higher throughput than their reflection counterparts because anti-reflection coatings are often deposited on the grating and the reflectivity off metal can be as low as 10% depending on the wavelength of light. Because the Wright Group nonlinear microscope doesn't need a highly dispersive element (large detection bandwidth, small CCD width) and will be fighting for every photon, we decided to use a transmission grating in the homebuilt spectrograph.

The final design decision considering a transmission grating will be used in the spectrograph is to decide between a holographic vs ruled grating. Holographic gratings don't have physically etched periodic rulings but rather a dichromated gelatin material with a sinusoidally varying refractive index imprinted by interfering laser beams. The changing refractive index is what gives this type of grating the ability to diffract light. Holographic gratings are well known for

their low ghosting and excellent broadband diffraction efficiency. For these reasons a holographic grating was seriously considered for the homebuilt spectrograph. However, upon interaction with an engineer at Wasatch Photonics, I was informed that “Low spatial frequencies are difficult with our technology…” and causes the diffraction efficiency to suffer both in magnitude and spectral uniformity. For this reason, I finally decided to use a transmission-based surface relief grating for the diffractive element in my homebuilt spectrograph.

The other optics that compose a spectrograph are the collimating and focusing optics. Fortuitously, before my time in the Wright Group, the group inherited a transmissive imaging spectrograph from the Hamers group at UW-Madison called the Holospec made by Kaiser Optical Systems.[65] The input and output of the spectrograph were orthogonal to each other, and Kaiser made specialty gratings that accommodated this drastic geometry. The low dispersion (and thereby low angles of diffraction, <10°) of the grating needed for the nonlinear microscope was incompatible with the footprint of the Holospec. Nevertheless, I harvested the collimating and focusing lenses from the Holospec and used them in my homebuilt version. They are Nikon Nikkor 85 mm f/1.4 commercial camera lenses which have excellent chromatic and spherical aberration correction making them ideal for 2D spatial imaging and hyperspectral imaging. Furthermore, using commercial camera lenses allows for the spectrograph alignment to be completely on-axis which further reduces aberration introduced by the spectrograph. This is not the case for the traditional Czerny-Turner spectrograph that uses curved mirrors for the collimating and focusing optics and suffers most prominently from astigmatism.[65]

The optical layout of the homebuilt spectrograph is shown in Figure 14. The grating will deflect the beam by an angle that satisfies the diffraction equation for a given wavelength of light. To ease the alignment and not have the focusing lens and camera at an angle, I opted to prepare the beam inside the spectrograph such that the optical train enters and exits the spectrograph on vertically offset but parallel lines (Figure 14a). The vertically offset camera from the spectral imaging mode alignment necessitates a similar beam deflection in the 2D spatial imaging mode alignment and is shown in Figure 14b.

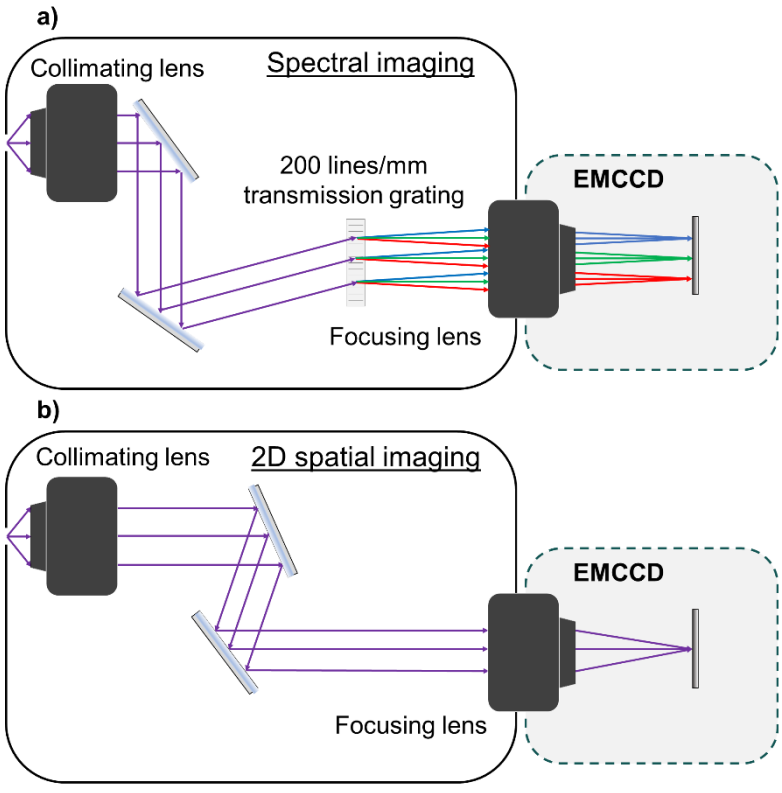

Figure 14 | Optical layout of transmission-based imaging spectragraph. a) spectral imaging configuration and b) 2D spatial imaging configuation.

The grating equation for a transmission grating is different than a reflection grating because the index of refraction of the substrate needs to be taken into account. The transmission grating equation is

$$n_g \sin\alpha - \sin\beta = \frac{m\lambda}{\sigma}$$

where n_g is the index of refraction of the grating substrate, α is the angle of incidence (AOI) relative to grating normal, β is the angle of diffraction (AOD) relative to grating normal, m is the diffraction order, λ is wavelength, and σ is the distance between grooves. Using this equation and knowing the desired spectral range of the microscope (visible from 400-800 nm), the width of the camera (8.2 mm, see Section 2.2.4), and the focal length of the focusing lens (85 mm), I calculated the linear spread of colors for various groove spacings. The groove frequency that best fits the spectrometer and camera criteria was 240 grooves/mm. Transmission gratings are less popular than reflection gratings and the variability in selection from grating suppliers reflects this. However, I was able to find a transmission grating from Richardson Gratings (owned by Newport) with 200 lines/mm which is slightly less spectral resolution than the ideal grating. The spectral range is extended to 360-840 nm to fit the camera width. Figure 15 illustrates the pixel-

to-wavelength mapping for the grating and camera that are used in the microscope (the colors are true for visible wavelengths [380-780 nm] and are artificially selected beyond this range).

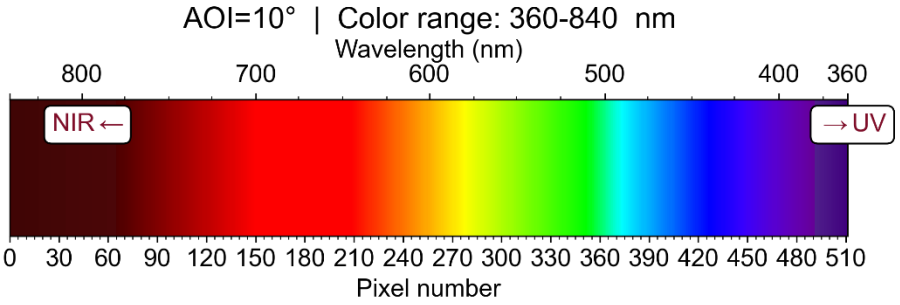

Figure 15 | Pixel to wavelength mapping for homebuilt imaging spectrograph and camera in the nonlinear microscope.

2.2.4 Detector/camera

Choosing the right camera technology was the most important aspect of the microscope design process because we knew we were going to be in a low-light regime. In a raster scanning setup the beam size effectively is the spatial resolution and needs to be focused down to the 1-5 μm range. While the fluence can remain the same as a typical ensemble measurement taken in the Wright Group of ~100 μJ/cm^2, the *total* number of photons used to excite the sample is a factor of 10^4 less and therefore results in significantly less signal photons to detect. In the widefield configuration, assuming the 100 μJ/cm^2 fluence again, a 2D array detector detects significantly more photons than the raster scanning setup and even the traditional ensemble measurement because it interrogates a larger sample area. However, the photons are spread over the entire detector so the photon number *per pixel* is similar to the photon number of a raster scanning

microscope. This is compounded by nonlinear spectroscopy inherently having low signal photon counts. Armed with this knowledge, we knew the detector had to excel in low-light conditions.

Additionally, we wanted to perform pump-probe measurements with this microscope which requires the detector to have read-out rates at or near the laser repetition rate of 1 kHz. For single-element detectors and even line cameras (single row, many columns) these read-out rates are readily achievable. However, full-frame readout rates for state-of-the-art scientific cameras these days peak at ~100 frames per second (fps). With region of interest and binning capabilities, however, readout rates can be significantly increased.

As mentioned previously, we knew we wanted to have a spectral axis with this microscope which motivated us to choose a camera over a single-element detector with a raster scanning configuration. We then needed to determine which camera technology was most appropriate for our application. The three main technologies are CCD, CMOS, and EMCCD. CCD is the cheapest of the three technologies but doesn't perform well in low-light conditions. CMOS is moderately priced, has faster full-frame readout rates but has fixed-pattern noise as well as rolling shutter artifacts. EMCCD is the most expensive but performs the best in low-light conditions which was a crucial factor in our decision. Moreover, modern EMCCD technology is capable of toggling between the traditional serial register and the electron multiplication register (i.e. it can amplify the signal or not). Finally, combining signal amplification and binning/region of interest collection strategies, frame rates close to that of CMOS cameras can be achieved. This makes EMCCD a 3-in-1 technology and is ultimately the reason we decided to pay the extra money for an EMCCD.

Beyond the multi-functional use of the EMCCD, it also provides a higher S/N ratio per pixel for a given photon flux. The photoelectron signal is calculated in Equation 1 as

$$S = I_{sample} * QE * t_{exp} \quad (1)$$

where I_{sample} (photons/s/pixel) is the signal intensity that makes it to the detector, QE (photoelectrons/photon) is the sensor's quantum efficiency, and t_{exp} is the camera exposure time. While there is only one source of signal, there are three sources of noise: shot noise, dark noise, and read noise. The number of counts due to dark current is calculated in Equation 2 as

$$D = I_D * t_{exp} \quad (2)$$

where I_D (electrons/s/pixel) is the dark current. The read noise, RN (electrons/readout), is an empirical value supplied by the manufacturer that depends on how quickly charge is transferred in the sensor. The system noise adds in quadrature and can be calculated in equation 3 as

$$N = \sqrt{S + D + RN^2} \quad (3).$$

Dividing Equation 1 by Equation 4 will give the S/N ratio for CCD and CMOS architecture. For EMCCD a multiplication factor, M, as well as an additional gain noise factor, F, must be incorporated into Equation 3. The calculated noise for an EMCCD is seen in Equation 4 as

$$N = \sqrt{F^2 * (S + D) + \frac{RN^2}{M^2}} \quad (4)$$

and shows that EMCCD lowers the limit of detection as Gain factors of 100x are readily achievable in today's EMCCD technology, with the option of going up to 1000x if needed. Figures 16 and 17 compare the signal and noise contributions in CMOS and EMCCD architecture based on Princeton Instrument's latest models for varying signal intensities. Figure 16 is in a high-intensity regime based on triple sum frequency measurements on a thin film of MoS_2 done previously by the Wright Group.[5] Figure 17 is in a low-intensity regime where there

is 1 signal photon per laser shot (10^6 times less than the high-intensity regime). Table 1 outlines the specifications of cameras considered for purchase to use in the microscope. In Figures 16 and 17, panel a) plots the signal of each camera (Equation 1), panel b) plots the noise (Equation 3 or 4 depending on camera technology), and panel c) plots the S/N ratio, all as a function of exposure time.

Table 1 | Camera parameters for S/N analysis.

	Kuro1200	**Kuro2048**	**ProEM1024**	**ProEM512**
Peak QE	0.92	0.92	0.92	0.92
I_D @ std. temp. (e^-/pix/s)	1.9	1.9	0.002	0.001
Read noise (e^- rms)	1.5	1.5	20 @ 5 MHz	25 @ 5 MHz
Pixel size (μm)	11 x 11	11 x 11	13 x 13	16 x 16
Num pixels	1200 x 1200	2048 x 2048	1024 x 1024	512 x 512
Imaging area (mm)	13.2 x 13.2	22.5 x 22.5	13.3 x 13.3	8.2 x 8.2

The signal unit is number of photoelectrons/pixel so it's important to take into account the pixel size for the following reasons: in the limit of significantly large pixel size, all the way to a single pixel that covers the entire sensor, say the number of photoelectrons generated on that sensor is large for a given signal intensity. Taking the opposite limit, where the entire sensor is made of infinitesimally small pixels that approaches 0 photons per pixel, the total amount of photoelectrons generated per *pixel* approaches 0 while the number of photoelectrons per *sensor* is the same as the large pixel size limit (when integrated over all pixels). *The takeaway here is that bigger pixels will collect more photons and lead to higher digitized pixel counts but at the*

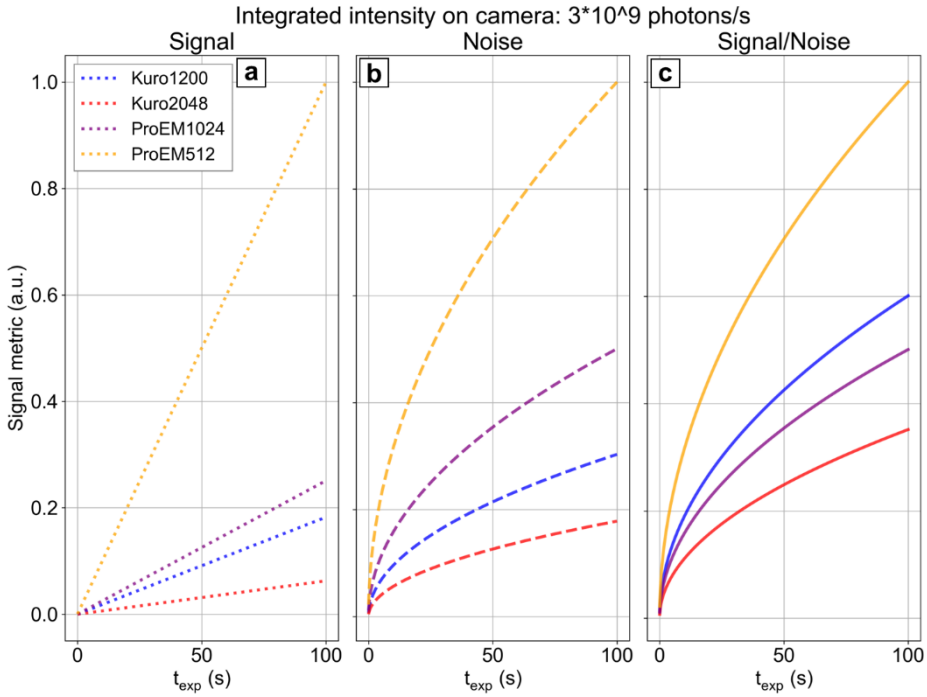

Figure 16 | Signal to noise comparison in the high-intensity regime for four Princeton Instrument cameras plotted as a function of camera exposure time. a) signal, b) noise, and c) signal/noise.

loss of spatial resolution. Figure 16a shows that the camera with the biggest pixels will have a larger amount of signal (the QE is the same for each camera). Accordingly, the added number of

photons per pixel will have larger contributions to the shot noise. Due to the required colder standard operating temperatures of EMCCD, its dark noise is significantly better than CMOS. The read noise of CMOS is considerably better than either CCD technology because CMOS has an analog-to-digital converter (ADC) for every pixel – charge doesn't have to be moved throughout the entire sensor where it can accumulate erroneous charge. This is different than CCD technology where there is a single ADC for the entire sensor. In the high-intensity regime, shot noise is the dominant noise source and EMCCD is superior to CMOS by a factor of 2-3 depending on specific camera comparison (Figure 16c). In the low-intensity regime at short exposure times, the high read noise of the EMCCDs is matched by the high dark current of CMOS (Figure 17b). At longer exposure times, the time-dependent dark current plays the

dominant role and significantly increases the CMOS noise compared to EMCCD. This results in the ProEM512 having nearly two orders of magnitude greater S/N ratio than both Kuro models and the ProEM1024 having about one order of magnitude greater S/N than both Kuro models.

This S/N analysis informed us on which EMCCD model to get in addition to strengthening our decision to purchase EMCCD over CMOS. The ProEM1024 sensor has 60% greater width than the ProEM512 which would provide greater spectral resolution. Considering the spectroscopy performed with this microscope will be done on relatively broad excitonic resonances, spectral resolution was not a significant consideration. Given the ProEM512 has a higher S/N per pixel and was 25% less expensive than the ProEM1024, we finally made the decision to purchase the ProEM512 to use as the camera in the nonlinear widefield microscope.

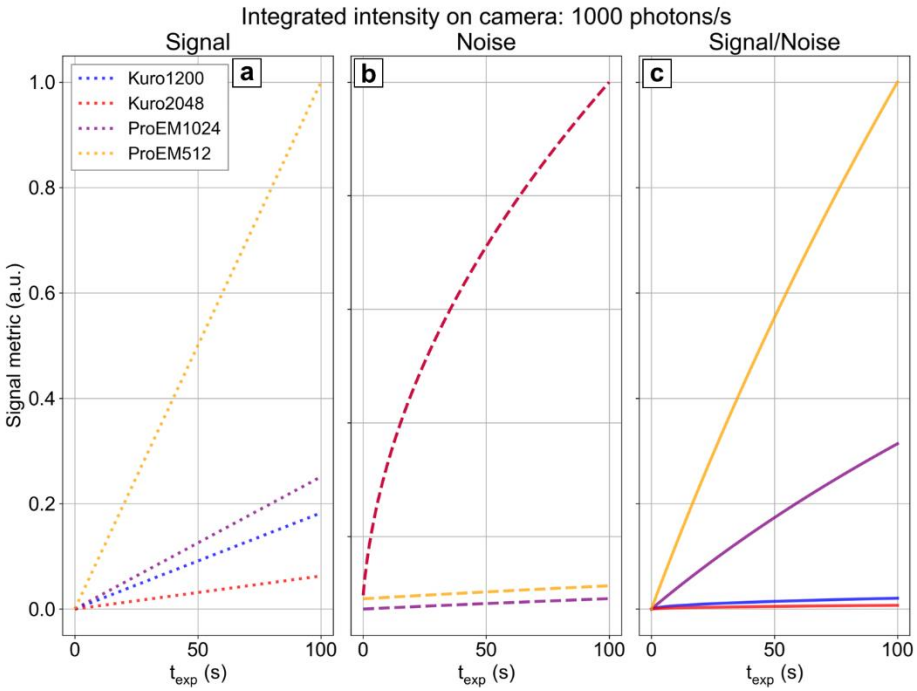

Figure 17 | Signal to noise comparison in the low-intensity regime for four Princeton Instrument cameras plotted as a function of camera exposure time. a) signal, b) noise, and c) signal/noise.

2.2.5 Zoomed out microscope view

After discussing the most important technical aspects of the microscope, I'd like to highlight the most important non-technical/logistical aspect that I wanted out of the microscope. Because the fs system that I was integrating the microscope into was already well-established in terms of downstream optics (excitation optics, signal collection and relay optics), I didn't want the microscope to get in the way of the laser system's established operation. I wanted the microscope to only add to the fs system capabilities, not take away. I'm pleased that with the remaining free space on the fs system optical table, I was able to build the entire microscope without getting in the way of the traditional spectroscopy setup. To change from the traditional to the microscope setup, only 3 flip mirrors need to be adjusted. These flip mirrors route the excitation beams to the microscope and are where the optical train starts in the zoomed-out view of the microscope in Figure 11. The three beams from two OPAs, as well as residual output from the upstream regenerative amplifier (termed "Leak Line"), are iteratively aligned such that the four beams travel parallel to one another. This alignment is not necessary for proper microscope operation but is performed to minimize the footprint of the instrument and to ensure all beams entering the microscope behave similarly. Another flip mirror may direct all beams so the microscope is in a reflective excitation geometry. As discussed earlier, this geometry has not been implemented in practice yet. Bypassing the mirror leads to several pick-off mirrors that individually route the beams to concave excitation mirrors. After the beams interact with the sample, the signal beams are collected by the microscope objective and sent to a tube lens that focuses the image on the imaging spectrograph slit. The grating inside the spectrograph sits on a magnetic mount which is used to toggle between 2D spatial imaging and spectral imaging modes. The EMCCD then collects the imaged photons.

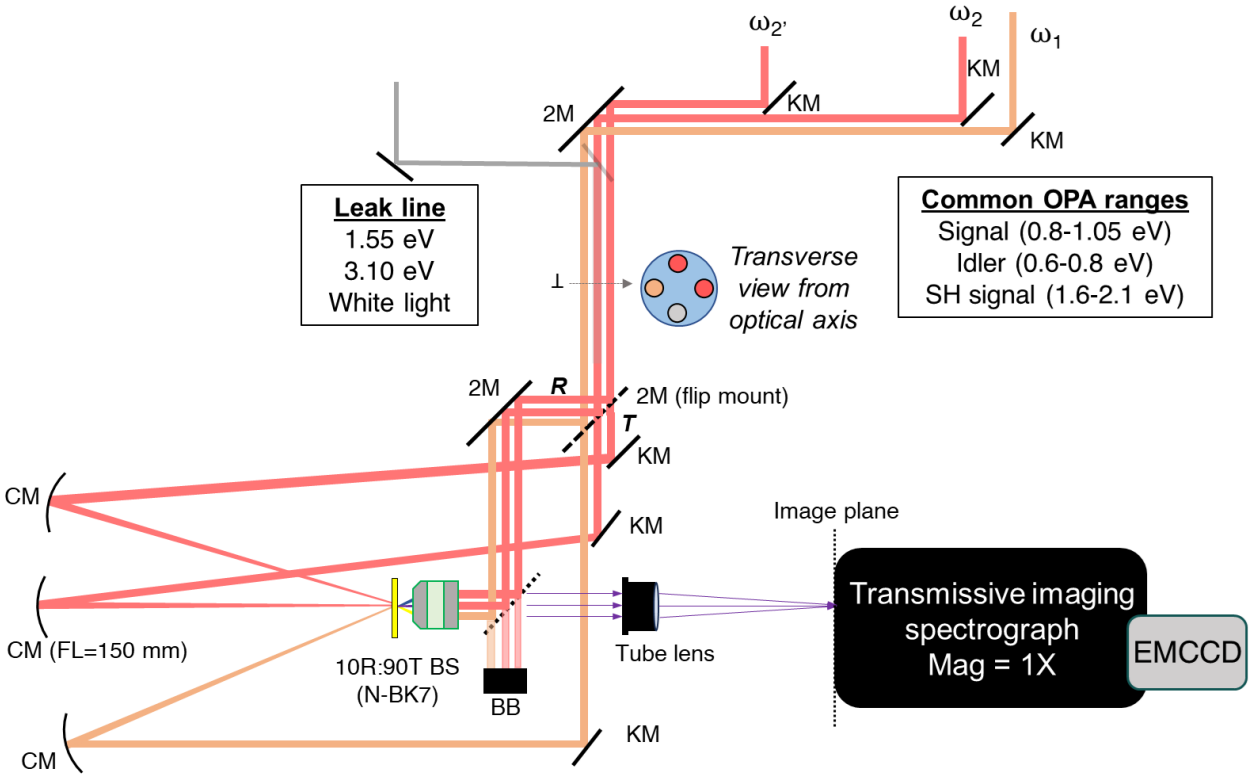

Figure 11 | Zoomed out optical layout of the widefield nonlinear microscope. Common OPA ranges employed in this dissertation are shown along with the available energies provided by the "Leak line" which is the remaining ~5% of the regenerative amplifier output that's not sent to the two upstream OPAs. The "R" and "T" denote reflection and transmission mode, respectively. Only a portion of the leak line beam path is shown to maintain figure clarity. KM: kinematic mirror; 2M: 2" flat mirror; CM concave mirror; BS: beam splitter; BB: beam block.

2.3 Proof of principle measurements

2.3.1 Manuscript: Widefield transient SHG microscopy on TMD 1Ls and HBLs

Authors: Jason M. Scheeler[1], Dan D. Kohler[1], Nicholas M. Olsen[2], Qiuyang Li[2], X.Y.-Zhu[2], John C. Wright[1]

[1]University of Wisconsin-Madison, Department of Chemistry

[2]Colombia University, Department of Chemistry

Introduction

Ultrafast transient second harmonic generation (tSHG) microscopy is a powerful technique because it correlates changes in a sample's second-order nonlinear susceptibility ($\chi^{(2)}$) with sub-diffraction limit spatial resolution. A material's static $\chi^{(2)}$ reports on parameters such as crystallographic orientation,[66–68] structural strain,[69,70] and optical resonances[12,71] making it a probe rich with information when used in SHG microscopy. Upon the introduction of charge carriers from an optical pump pulse, $\chi^{(2)}$ has been shown to change on an ultrafast time scale due to rearrangement of the crystal lattice[72,73] as well as charge transfer between donor and acceptor materials.[43,74,75]

Transient absorption microscopy (TAM) is the linear analogue to tSHG microscopy and its use as a technique has seen a steep rise in the last decade.[76] It's been used to study unique photophysics in two-dimensional (2D) materials such as quantifying the moiré potential in transition metal dichalcogenide (TMD) heterobilayers (HBLs),[44] spatially tracking hot carrier cooling in metal halide perovskite thin films,[77] and packing arrangement effects on singlet fission time scales in organic semiconductors.[61] The defining difference between TAM and tSHG, which can be

extended to other multidimensional probes like third harmonic generation (THG),[5,12] is the probe is generated primarily in the sample and has negligible contribution from the substrate (assuming the probe interacts with a strong excitonic transition dipole). The essentially background-free signal in the case of nonlinear probes can result in better S/N and help simplify pump-probe line shape interpretation. The difference between linear and nonlinear probes is particularly stark in the case of reflection where the intensity of a linear probe depends both on the material's resonance and the refractive index mismatch between sample and substrate. Often reflective resonances ride on a strong background from the substrate and the pump-probe line shapes become non-trivial to interpret and require optical modeling to quantitatively understand. Using SHG as a probe of exfoliated TMDs stratified by a SiO_2 substrate, like the present work, is a special use case of time-resolved nonlinear microscopy. Monolayers (1Ls) of TMDs are noncentrosymmetric and support strong SHG while SiO_2 does not, providing clean access to the differential signal from the analyte. THG, on the other hand, is agnostic to sample symmetry and would be a more general use case for time-resolved nonlinear microscopy. Both THG and SHG have previously been demonstrated as viable probes to investigate the photophysics of a variety of TMD sample morphologies including 1Ls, thin films, and screw-dislocation spirals.[12,74,75,78,79]

Monolayers of TMDs with transition metal Mo or W and the chalcogen S or Se act as an ideal system for investigating using tSHG microscopy. In their bulk form they are indirect semiconductors with bandgaps in the NIR. When layers comprising the bulk structure, which are held together by van der Waals forces, are stripped down to a single layer the band gap becomes direct and fluoresces strongly in the visible spectral region. 1L TMDs host excitons with large binding energies due to reduced Coulomb screening from quantum confinement and possess spin-valley polarized charge carriers as a result of broken time-reversal symmetry.[27,32,33,80–83]

Their unique materials physics makes them promising candidates for applications in next-generation devices that utilize spintronics[35,84,85] and high-performance transistors.[86] When vertically stacked, 1L TMDs become greater than the sum of their parts as close spatial proximity results in out-of-plane orbital overlap and strongly couples the constituent layers. This coupling leads to a plethora of exotic physics realized in TMD HBLs such as moiré excitons,[87,88] ultrafast charge transfer,[89] bright interlayer exciton (IX) emission and prolonged IX lifetimes,[90] and robust IX spin-valley polarization.[91,92] Recent studies have shown that the twist angle affects the interlayer distance and is therefore indicative of the coupling strength between layers.[93–96]

There are numerous examples that use SHG to characterize the crystallographic orientation and symmetry of 1L TMDs. The SHG fields generated by an even number of layers stacked in a 2H configuration (60° twist angle between successive layers) will destructively interfere to produce no SHG. SHG in stacked structures can be turned on by having an odd number of layers or an even number of layers with twist angles ≠ 60° and will produce the strongest SHG for 3R phases (0° twist angle between layers).[97] TMD HBLs have been shown to induce elliptically polarized SHG output even for aligned layers due to a material dependent SHG phase factor.[98] This reduces the contrast between the lobe peaks and nodes in SHG polar plots for HBLs even in pristine crystals. Reduced contrast in TMD SHG polar plots can also arise due to imperfections in the crystal lattice like atomic substitution (oxygen in ambient conditions with S and Se) or atomic vacancies that destroy the translational symmetry. This results in an SHG active material where the features due to crystal symmetry in the polar plot are suppressed.[99]

Ensemble-averaged tSHG experiments have been previously carried out on TMD 1Ls[100] and HBLs[43]. In the HBL study, small but reproducible increases in SHG were detected for a WS_2/MoS_2 HBL. The positive changes were attributed to a space-charge field from transferred

electrons and holes at the interface that creates an asymmetry in the sample and increases the number of SHG photons. Conversely, spatially resolved tSHG experiments performed on $WSe_2/MoSe_2$[74] and WSe_2/MoS_2[75] HBLs saw large decreases in the pumped SHG of 10-20%, more like the response found in the current work. The spatially resolved experiments in Zimmerman *et al*. employ a widefield microscopy setup which is advantageous for investigating large areas of the sample in a single experiment with minimal sample preparation.[79] This is an important technique to utilize as the analysis of wafer-scale TMDs in modern semiconductor foundries for locating defects and impurities needs to move beyond the prohibitively low-throughput methods like scanning tunneling microscopy and transmission electron microscopy.[101] The more popular confocal, raster-scanning pump-probe microscopy setups, while having many advantages, typically interrogate smaller sample areas (~10 x 10 μm) which prohibit efficient sampling of large-areas TMDs.[102] Even with the widefield imaging setup used by Zimmerman *et al.* the HBL overlap areas were only on the ~20 x 20 μm scale. Furthermore, in the pumped SHG images in these studies, if shown, there was not a clear delineation between the HBL and the constituent 1Ls making it hard to correlate transient behavior with specific 1L and HBL regions.

In this work, we employ polarization-resolved widefield tSHG microscopy to a $WS_2/MoSe_2$ sample and simultaneously interrogate large domains separated by macroscopic grain boundaries (GBs) of the HBL and both the WS_2 and $MoSe_2$ 1Ls. The SHG images are spatially well-resolved and distinguish the different materials. We find different domains give markedly different pumped SHG intensities. We see this behavior across TMD HBLs that vary in both layer composition and twist angle, making this a general aspect of TMD HBL photophysics when viewed through the lens of polarization-resolved tSHG microscopy.

Methods

Sample preparation

1L TMDs are exfoliated from their bulk crystal using a gold tape exfoliation method.[103] A layer of ultra-flat gold tape underneath a stack of thermal release tape (TRT) and polyvinylpyrrolidone (PVP) contacts a bulk crystal of $MoSe_2$ to exfoliate a 1L. The 1L $MoSe_2$ and the stack of other materials are then stamped onto the fused silica substrate. The stack is heated up to 130°C to remove the TRT and rinsed with water and a solution of I_2/I^- to get rid of the PVP and gold tape layers, respectively, leaving behind the isolated 1L $MoSe_2$ on fused silica. The same procedure is done with a bulk crystal of WS_2 and subsequently stacked onto the $MoSe_2$ layer.

Polarization- and time-resolved widefield SHG microscopy

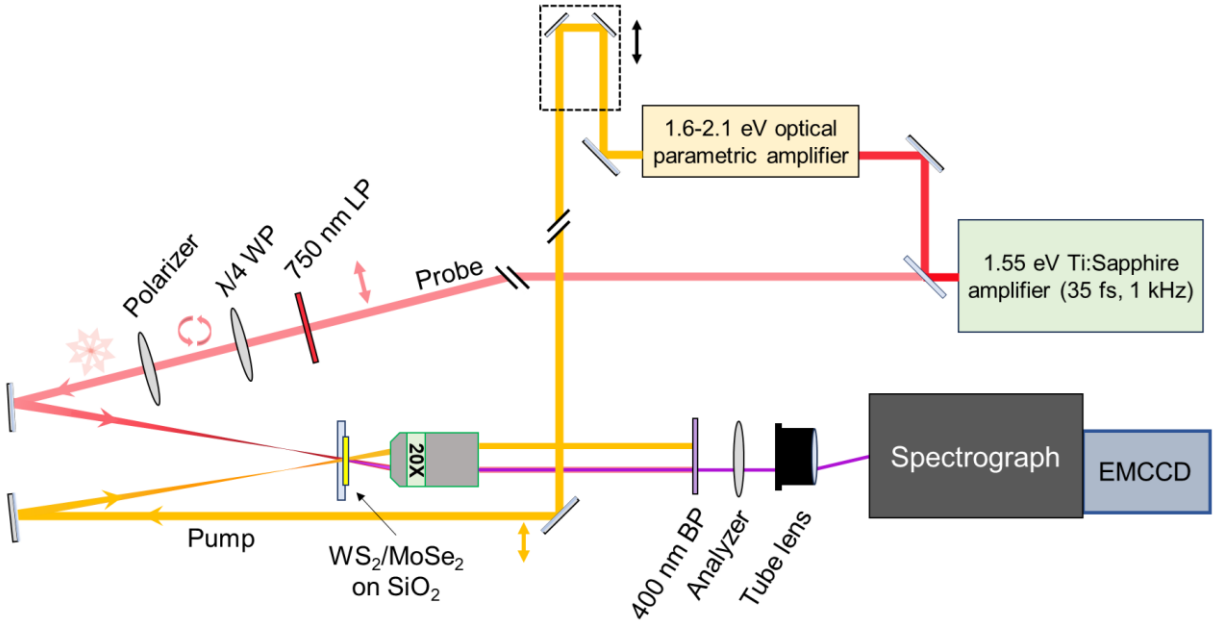

Figure 18 | Optical layout of the polarization- and time-resolved widefield SHG microscope described in the main text. The breaks in the optical beam paths indicate travel not relevant to the experiment. WP: waveplate, LP: longpass, BP: bandpass.

Figure 18 illustrates our nonlinear widefield SHG microscope setup. It uses a regenerative amplifier seeded by a Ti:Sapphire oscillator (Spitfire and Tsunami respectively, Spectra-Physics) which produces pulses centered at 1.55 eV with a temporal duration of ~35 fs. To create the pump arm, half of the amplifier output is sent to an optical parametric amplifier (OPA; TOPAS-C, Light Conversion) that produces frequency-tunable pulses from 1.6-2.1 eV. Dichroic and absorptive filters further isolate the frequency range of interest. The vertically polarized beam is sent through a mechanical delay stage to create the time delay with the probe arm. We empirically calculate a delay offset for pump pulses throughout the entire frequency range. To create the probe arm, ~5% of the amplifier output is sent through a 750 nm LP filter (Corning) to reject weak SHG generated on metal mirrors and a quarter waveplate (Thorlabs, AQWP05M-

600) to create circularly polarized light. A wire grid polarizer (Thorlabs, WP25M-UB) in a mechanically controlled rotation mount selects a linear polarization to be sent to the sample.

The pump and probe beams are focused by 150-mm focal length concave mirrors (Thorlabs, CM254-150-P01) at an angle of incidence of 10° on either side of the sample normal. Both beams progress through their focus and continue ~25 mm along the optical axis before hitting the sample. The size of both beams at the sample plane is ~0.6 mm FWHM. We choose this beam size to cover the entire field of view. These excitation conditions allow us to investigate large areas (0.5 x 0.5 mm) of the sample in a single experiment. All excitation and generated beams are collected in a transmissive geometry by an infinity-corrected microscope objective (20X Mitutoyo Plan Apo SL) that's aligned to sample normal. The SHG probe photons are isolated with a 400 nm BP filter (Thorlabs, FBH400-40) and are polarization-analyzed (passing *s*-polarization) before being focused by a tube lens (Thorlabs, TTL200) onto the slit of a homebuilt imaging spectrograph featuring a back-illuminated EMCCD (Princeton Instruments ProEM-HS: 512BX3) for the detector. Typical camera exposure times are 40 seconds.

The pump beam is "chopped" with a mechanical shutter. At every scanned motor position (delay or polarization in this study) we acquire a pump-off and pump-on image before proceeding to the next motor position. Due to the large area investigated with our technique, the beam intensity at the image edge is about 70% of the intensity at the image center. We account for this intensity variation by imaging the pump beam at sample position onto the camera and fitting the intensity profile to a 2D Gaussian. Additionally, a portion of the pump beam is picked off before the sample and is sent to a pyroelectric detector to track laser intensity fluctuations throughout the duration of the experiment. We then use these two control measurements to power-normalize our tSHG images in both space and time at post-processing. Unless otherwise noted we plot the

relative changes in SHG counts where we normalize differential SHG counts to the number of unpumped counts, that is, $rel.\Delta SHG = \frac{I_{SHG}^{pumped} - I_{SHG}^{unpumped}}{I_{SHG}^{unpumped}}$. All hardware was controlled through the yaq protocol[104]; experiments were orchestrated using an in-house deployment of Bluesky.[105]

Results and Discussion

An optical micrograph of the large-area $WS_2/MoSe_2$ HBL used in the tSHG experiment is shown in Figure 19a. There is a distinct region of pure 1L WS_2 in the lower left part of the image, pure 1L $MoSe_2$ in the upper right, two distinct HBL regions in the upper left and lower right, and the SiO_2 substrate in the lower middle. In both the 1L and HBL regions there are cracks that create domains; these cracks are likely inherited from the parent crystal and/or introduced during the exfoliation and stamping processes. Figure 19b illustrates the static SHG response of the sample (the airy disk-type patterns seen on the left side of the image are due to dust/residue on the substrate and not the collection optics). There are cracks within the pure 1Ls that create domains which give a uniform SHG intensity. However, this is not the case for the HBL domains. The average SHG intensity of the domain indicated by the orange star (D1) is higher than that of the domain indicated by green star (D2). The SHG intensities change abruptly at the cracks that

define the domains and are not imprinted by the excitation beam. This implies there's a local character to different domains located within the HBL that affects the $\chi^{(2)}$.

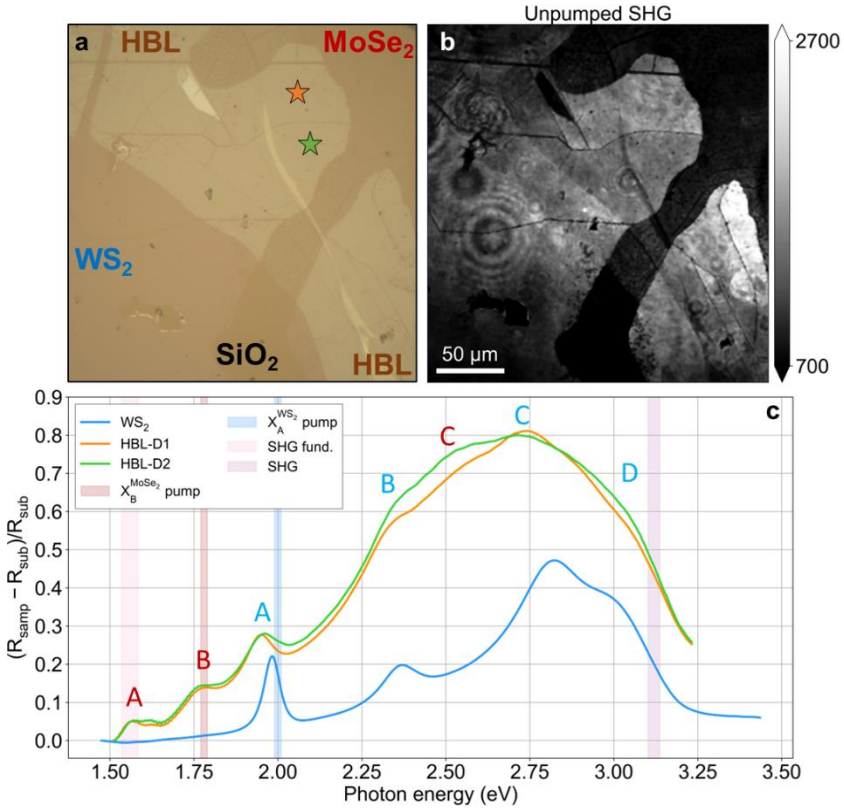

Figure 19 | Model $WS_2/MoSe_2$ HBL used for tSHG experiments. a) Optical micrograph of the bottom $MoSe_2$ layer (right) overlapping with the top WS_2 layer (left) to form two large HBL areas (upper left and bottom right). b) Unpumped SHG response. The SHG intensity in the HBL domain indicated by the orange star (HBL-D1) in panel a) is higher than the SHG intensity in the HBL domain indicated by the green star (HBL-D2). c) reflection contrast spectra for HBL-D1, HBL-D2, and pure WS_2 for a reference. The HBL resonances are labeled and the color of the font indicates which layer the resonance originates from (red for $MoSe_2$, blue for WS_2). The colored vertical boxes indicate pump and probe colors used in the experiment.

Figure 19c plots the reflection contrast of the HBL domains indicated by the stars in Figure 19a along with that of the pure WS_2 region for comparison. For this sample and substrate morphology (atomically thin sample on transparent substrate), the reflection contrast is roughly equivalent to the absorptance.[106] The two HBL domains display a similar absorptance for the

band-edge features, namely the A and B excitons which arise from spin-split bands at the valence band maximum (peaks labeled A and B, with color indicating where the resonance originates: red-$MoSe_2$, blue-WS_2). Domain absorptance differs for resonances at higher energies. D1 absorptance (orange trace) shows broad but distinguishable peaks at the C exciton (2.51 eV for $MoSe_2$ and 2.79 for WS_2), which arises from the well-known band nesting feature from parallel bands spread across the Γ-Λ points in the Brillouin zone. In addition, a broad but distinguishable peak can be seen at ~3.08 eV in the D1 absorptance which is the lesser-studied D exciton that originates from the Γ point.[23] These features are harder to distinguish in the D2 absorptance due to the resonances being broadened, otherwise the D1 and D2 regions' absorptance spectra are qualitatively the same. Their similarity in absorptance is corroborated by AFM measurements showing an equal, albeit large, distance between the top WS_2 and bottom $MoSe_2$ layers in both domains (Figure S1). The interlayer distance of ~70 nm for both domains indicates weak to no coupling between the two layers. Rather than quenched photoluminescence (PL) at the A exciton energies indicative of strong van der Waals interactions, the PL spectrum (Figure S2) shows redshifted peaks for both layers indicative of a sample with macroscopic defects such as wrinkles and cracks.[107] The degree of degradation and the large interlayer distance are consistent with the studied samples being two years old at the time experiments were conducted.

Figure 20 compares the unpumped SHG response to the tSHG response at various pump colors and a pump-probe delay of T=0.2 ps. The unpumped SHG spectrum (Figure 20a, duplicated from Figure 19b) acts as a direct comparison to the tSHG images. Figure 20b shows the relative change in SHG intensity of the $WS_2/MoSe_2$ HBL when pumping at the $MoSe_2$ B exciton energy. When pumped at this energy, D2 shows a ~15% relative decrease in SHG intensity compared to ~3% for D1. The disparity in SHG intensity between D1 and D2 is more drastic in the ΔSHG/SHG response compared to the unpumped SHG. We understand the decreased SHG to be a result of a combination of photophysical processes including Pauli blocking,[74,75] bandgap renormalization,[108] and resonance broadening.[109]

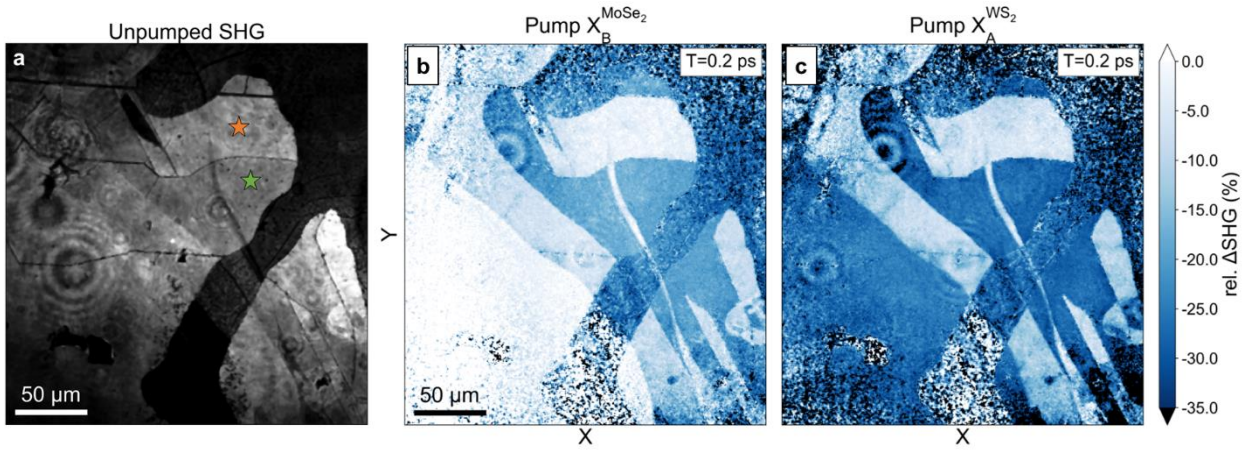

Figure 20 | Comparison of unpumped SHG images to tSHG images for two different pump colors at a pump-probe delay of T=0.2 ps. a) unpumped SHG image duplicated from Figure 19b. The orange star indicates HBL-D1 and has a higher unpumped SHG intensity than HBL-D2 indicated by the green star. b) tSHG response when pumping at the $MoSe_2$ B exciton energy and c) tSHG response when pumping at the WS_2 A exciton energy.

In Figure 20b the pure 1L $MoSe_2$ region shows an even stronger SHG suppression than D2 of ~25%, while both the substrate and pure 1L WS_2 regions oscillate about zero as expected for this pump energy. When the pump is tuned to the WS_2 A exciton energy (Figure 20c) we observe similar tSHG behavior compared to the $MoSe_2$ pump. The main differences are the pumped SHG

intensities in the pure 1L WS_2 region decrease by 25% as is expected while the other regions have additional smaller decreases. We find no difference between HBL domains when using a linear probe (Figure S3).

The sign of our ΔSHG values is consistent with Zimmerman *et al*.[74,75] and inconsistent with Yao *et al*.[43] We note that all three studies have strikingly similar experimental conditions. All parties pump resonantly with fluences in the 10s of $\mu J/cm^2$ range; all use a probe fundamental centered at ~1.55 eV and interrogate the sample off-axis at an angle of incidence of 10-20°. Zimmerman *et al.* and the present work have both studied several HBLs and see the decrease in ΔSHG/SHG across all HBL samples (WS_2/WSe_2, MoS_2/WSe_2 and $WS_2/MoSe_2$, WS_2/WSe_2, WS_2/MoS_2, respectively) suggesting the increase in pumped SHG intensity seen by Yao *et al.* was not due to the specific identity of the constituent monolayers as Yao *et al.* studied the same WS_2/MoS_2 system as the present work. Both Yao *et al.* and Zimmerman *et al.* provide data indicating close interlayer contact and strong coupling. Ultimately, the experimental conditions and sample comparisons draw no logical conclusion to explain the difference in ΔSHG sign. Thus, the discrepancy likely arises from more nuanced features of the samples including defects, how the adherence of the bottom layer to the substrate affects its electronic structure, and the interlayer distance between the two 1Ls.

The ΔSHG differences between domains is not unique to this sample as was also found in a second $WS_2/MoSe_2$ sample (Figure S4). We realize the probe fundamental being resonant with the $MoSe_2$ A exciton may suppress the ΔSHG artificially (from pumping by the front half of the probe pulse), perhaps making the ΔSHG discrepancy between HBL domains unique to HBLs that include $MoSe_2$. (The potential pumping by the probe is most evident in Figure 20c where the 1L $MoSe_2$ region has nearly the same ΔSHG as D2 in the HBL, which is expected to have more

suppressed SHG due to additional contributions from charge carriers created in the WS_2 layer.) However, this is a characteristic that is likely common across all types of TMD HBLs as we find ΔSHG discrepancies between different domains in a WS_2/WSe_2 sample with a twist angle of ~25° and a nearly aligned WS_2/MoS_2 sample (Figure S5) where the lowest energy resonances in these structures are ~1.60 and ~1.85 eV, respectively. Static SHG in a $WS_2/MoSe_2$ HBL with 1.55 eV fundamental has been studied before, although there was a 30° twist angle between layers.[46] They found that the HBL gave suppressed SHG relative to both the pure 1L WS_2 and the pure 1L $MoSe_2$ and that the output energy was important in determining whether the HBL SHG intensity was enhanced or suppressed relative to the pure 1Ls. The SHG energy in the current work is 3.10 eV which is resonant with the D exciton in the WS_2 layer that originates from the Γ point where W orbitals make up the majority of those bands.[110] While there is a slight difference in static SHG intensity between D1 and D2, the disparity is more drastic for the *pumped* SHG. This suggests that carriers induced by the pump (at the K point) may interact with the bands at

the Γ point differently. Further work demonstrating the SHG output is a probe of the Γ point in a more strongly coupled HBL sample is needed to support this theory.

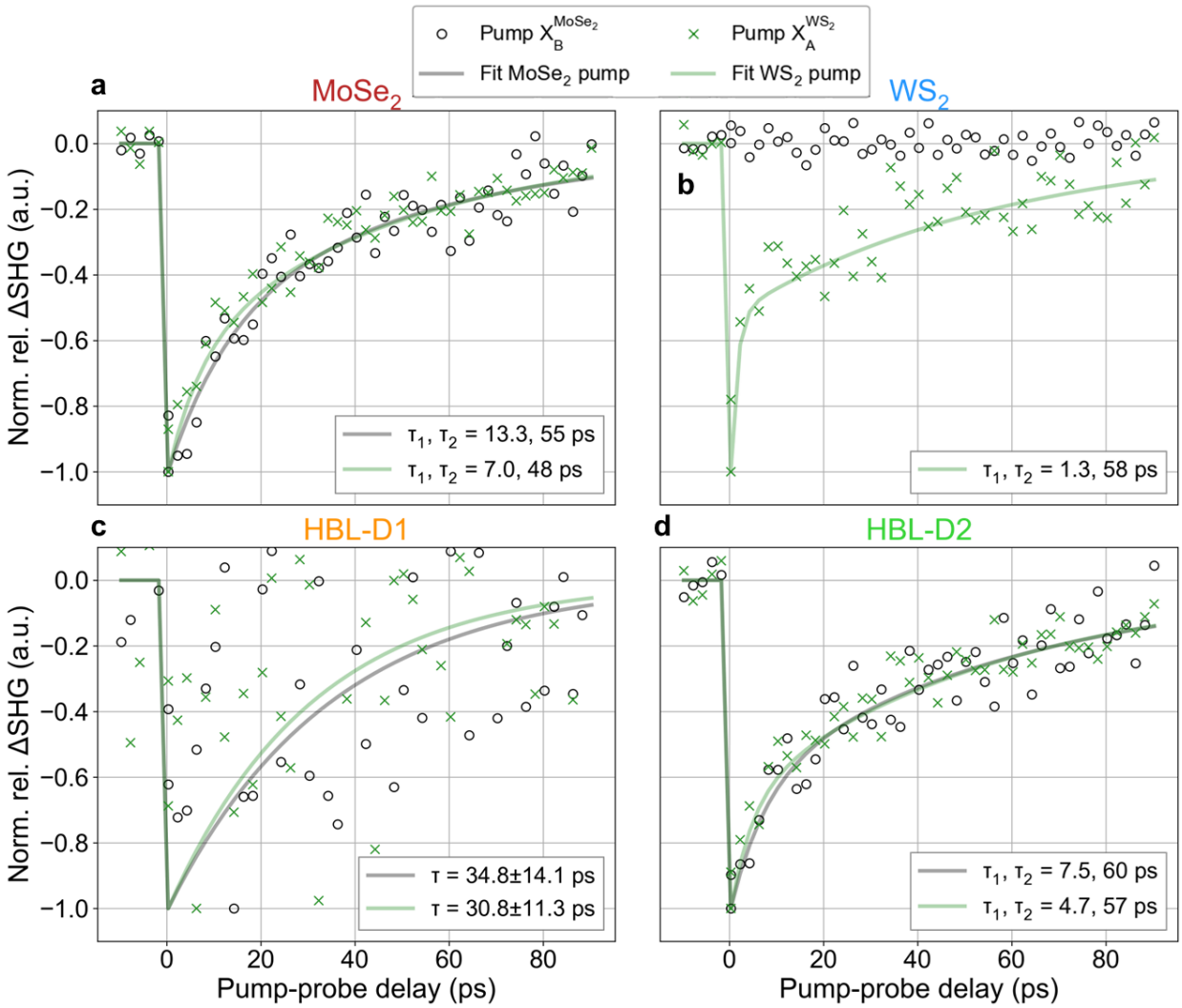

Figure 21 | Comparison of pure 1L and HBL population dynamics for two different pump energies. The black circles indicate a $MoSe_2$ B exciton pump and the green crosses indicate a WS_2 A exciton pump. The solid lines are biexponential fits of the data with the corresponding marker color. All delay traces are spatially averaged over 1000s of pixels. a) delay traces for the pure $MoSe_2$ region, b) delay traces for the pure WS_2 region, c) delay traces for HBL-D1, and d) delay traces for HBL-D2.

Figure 21 compares the pump-energy dependence of the population dynamics for the four regions of interest. All traces are normalized to the maximum ΔSHG/SHG value. The dynamics

of the $MoSe_2$ region show minimal variation between pumping at the $MoSe_2$ B exciton energy (Figure 21a, black circles) compared to pumping at the WS_2 A exciton energy (green crosses). The colored lines are fits to the corresponding data and are best fit with a biexponential for all regions except D1 which is fit with a monoexponential. The shorter time constant is attributed to carrier-carrier scattering as the pumps create a large concentration of excitons as well as defect-assisted carrier scattering due to the old age of the sample. The longer time constant is attributed to radiative exciton recombination. The fitted transients for the $MoSe_2$ region suggest that both the shorter and longer dynamics are mildly faster for the WS_2 A exciton pump. In the pure WS_2 region (Figure 21b), the $MoSe_2$ B pump doesn't create any carriers as expected. The degree of carrier-carrier scattering when pumping at the WS_2 A exciton energy is most prominent in the pure WS_2 region and is likely due to the stronger absorption at this energy compared to the $MoSe_2$, D1, and D2 regions (Figure 19c). Due to the minimal tSHG signal for HBL-D1, the spread of data for those traces (Figure 21c, black and green markers) is considerably higher than the other regions. Accordingly, the monoexponential fits have a large error associated with them. The dynamics for HBL-D2 closely resemble the pure $MoSe_2$ dynamics, where there's minimal dependence on the pump energy besides slightly faster relaxation when pumped at the WS_2 A exciton energy. However, the same measurements performed on a different $WS_2/MoSe_2$ sample show the dynamics are similar but slightly faster when pumping at the $MoSe_2$ B exciton energy Figure S6). Overall, when considering the dynamics of both $WS_2/MoSe_2$ samples, the dynamics of HBL-D2 resemble the dynamics of the individual constituent 1Ls with no interlayer coupling and no dependence on the pump energy. There is also no pump-energy dependence for the pure $MoSe_2$ region. We note the dynamics of all regions except for HBL-D1 are in line with literature values.[44,45,111]

Conclusion/Outlook

We exemplified polarization-resolved tSHG microscopy as an imaging technique that utilizes a multidimensional probe to enhance sample response over the substrate response. The HBL-D2 dynamics match those of the pure 1L regions and resembles an uncoupled HBL system with no dependence on pump color. The widefield geometry allowed us to investigate large HBL areas simultaneously, revealing stark heterogeneities between domains that are not apparent by linear characterization methods such as PL, Raman, and transient transmission. This disparity would be missed in ensemble-averaged measurements and may be overlooked by confocal microscopy methods where the field of view is significantly smaller, highlighting the importance of widefield nonlinear microscopy. While a more detailed study needs to be carried out to definitively assign the root cause of the heterogeneity, we posit it is caused by local differences in twist angle, strain, and interfacial chemistry, all of which can affect the complex $\chi^{(2)}$. These results demonstrate the complementary information that a multidimensional probe provides over a linear probe for time-resolved investigations of TMDs. Using a similar technique to the one presented herein, but with circularly polarized pump and probe pulses to assess the large-area photophysical response of spin-valley polarized carriers, could be insightful for TMD HBL uses in spintronic devices.[34]

2.3.2 Supplementary Information: Widefield transient SHG microscopy on TMD 1Ls and HBLs

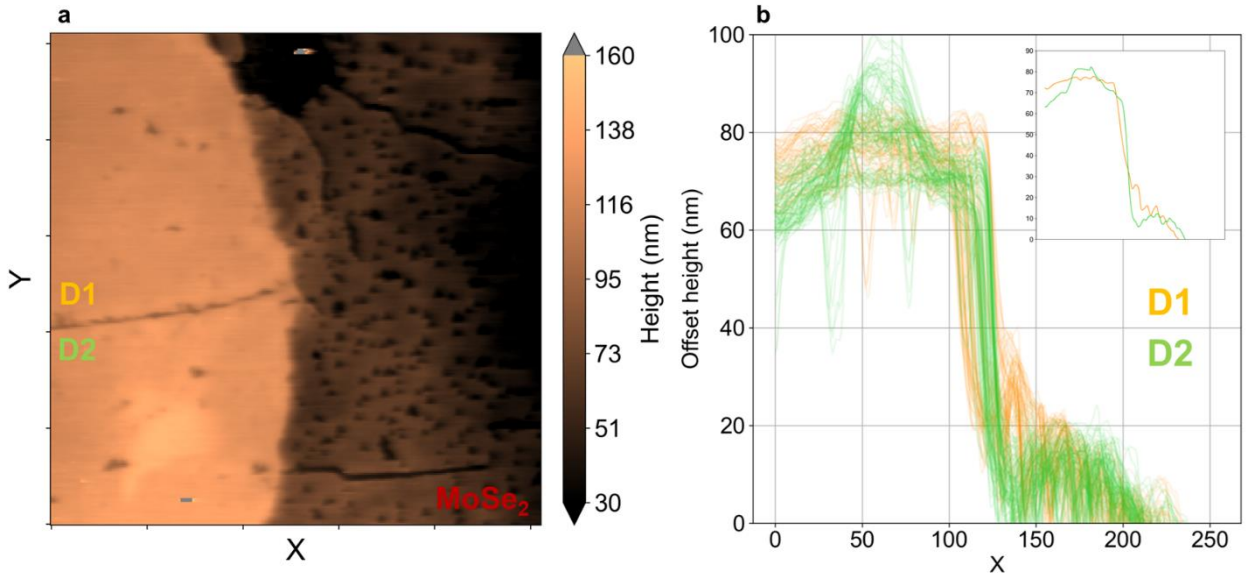

Figure S1 | AFM of the D1 and D2 regions highlighted in the main text. a) 2D topological map with the pure 1L $MoSe_2$ on the right-hand side with the domains on the left hand side. Domains are separated by the crack in the middle with D1 on top and D2 on bottom. b) 1D line profiles indicating the interlayer distance between 1L $MoSe_2$ and 1L WS_2 in D1 and D2. Inset: Average line profile.

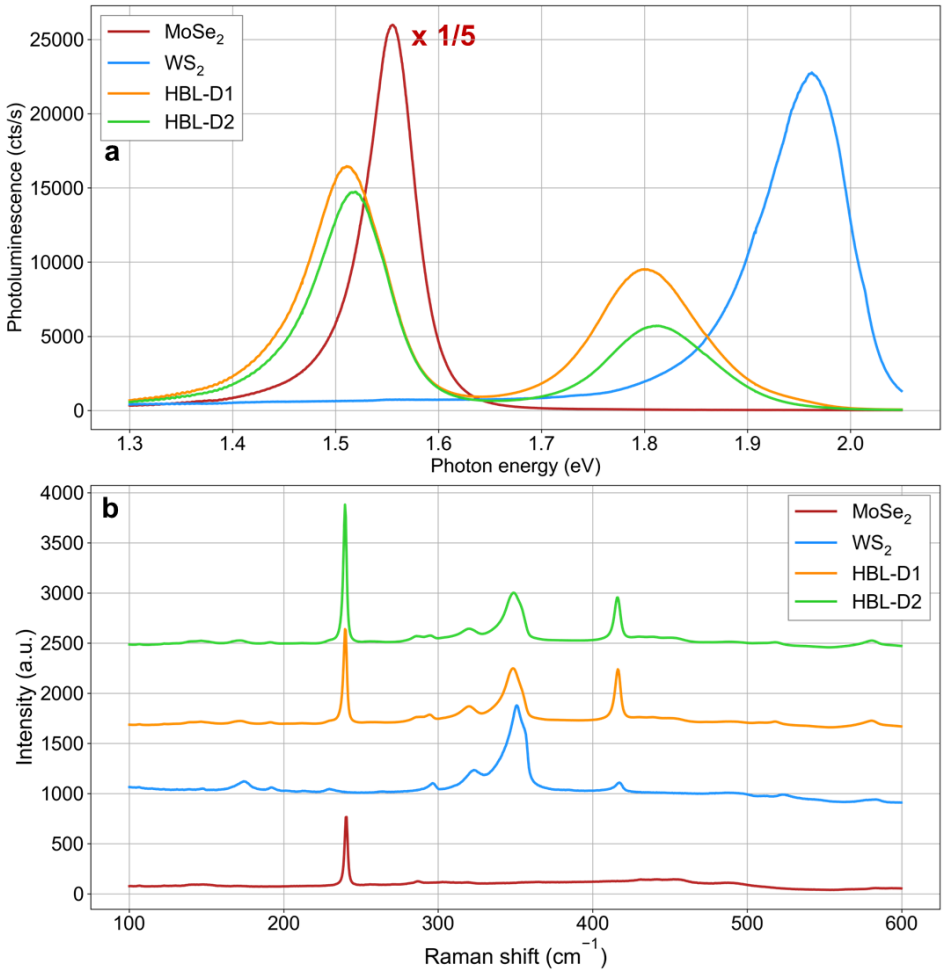

Figure S2 | Sample characterization of the four regions highlighted in the main text. a) PL spectra and b) Raman spectra.

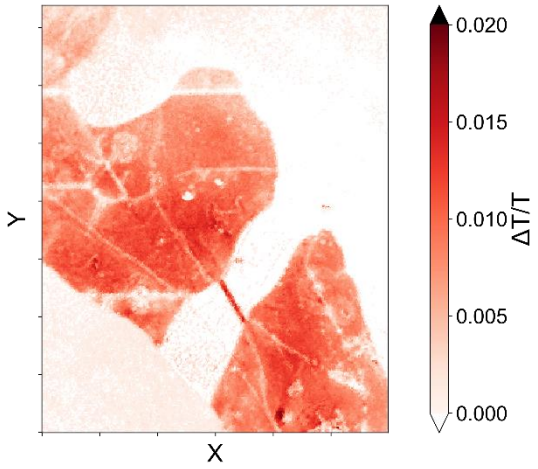

Figure S3 |Transient transmission image when pumping at the WS_2 A exciton and probing at 1.51 eV (MoSe2 A exciton in the HBL). The heterogeneities that are readily apparent in the tSHG images are not in the case of a linear probe.

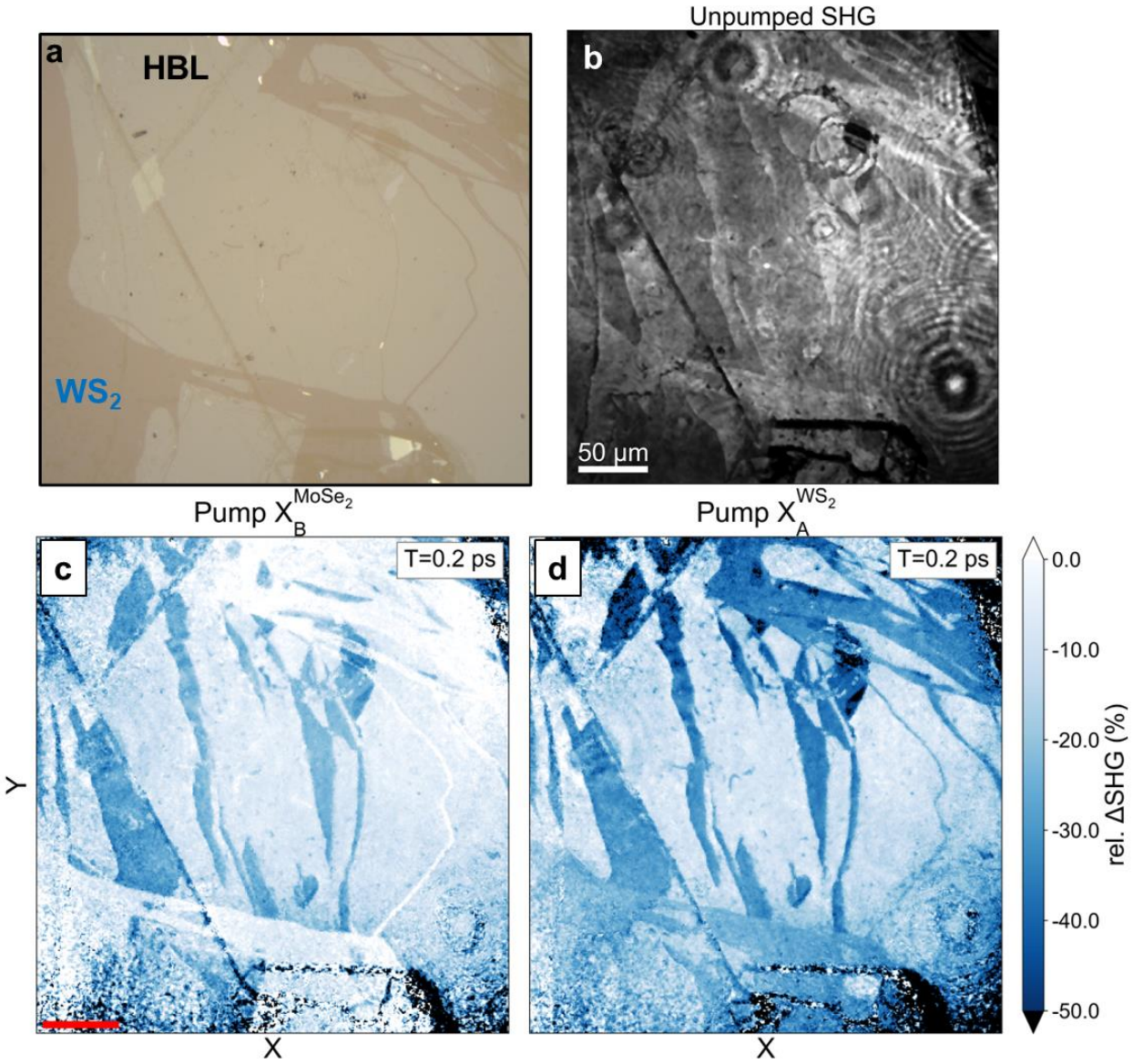

Figure S4 | Optical, unpumped, and tSHG images of a second $WS_2/MoSe_2$ HBL sample. a) Optical micrograph indicating the pure 1L WS_2 region in the bottom left with the HBL covering the majority of the image. b) unpumped SHG image. The circular, airy disk patterns are due to residue on the substrate/sample and not the collection optics. c) tSHG image at T=0.2 ps when pumping at the $MoSe_2$ B exciton energy. Scale bar is 50 μm. d) tSHG image at T=0.2 ps when pumping at the WS_2 A exciton energy. In the tSHG images, there are cracks that define domains of large SHG intensity changes and domains where there are minimal SHG intensity changes.

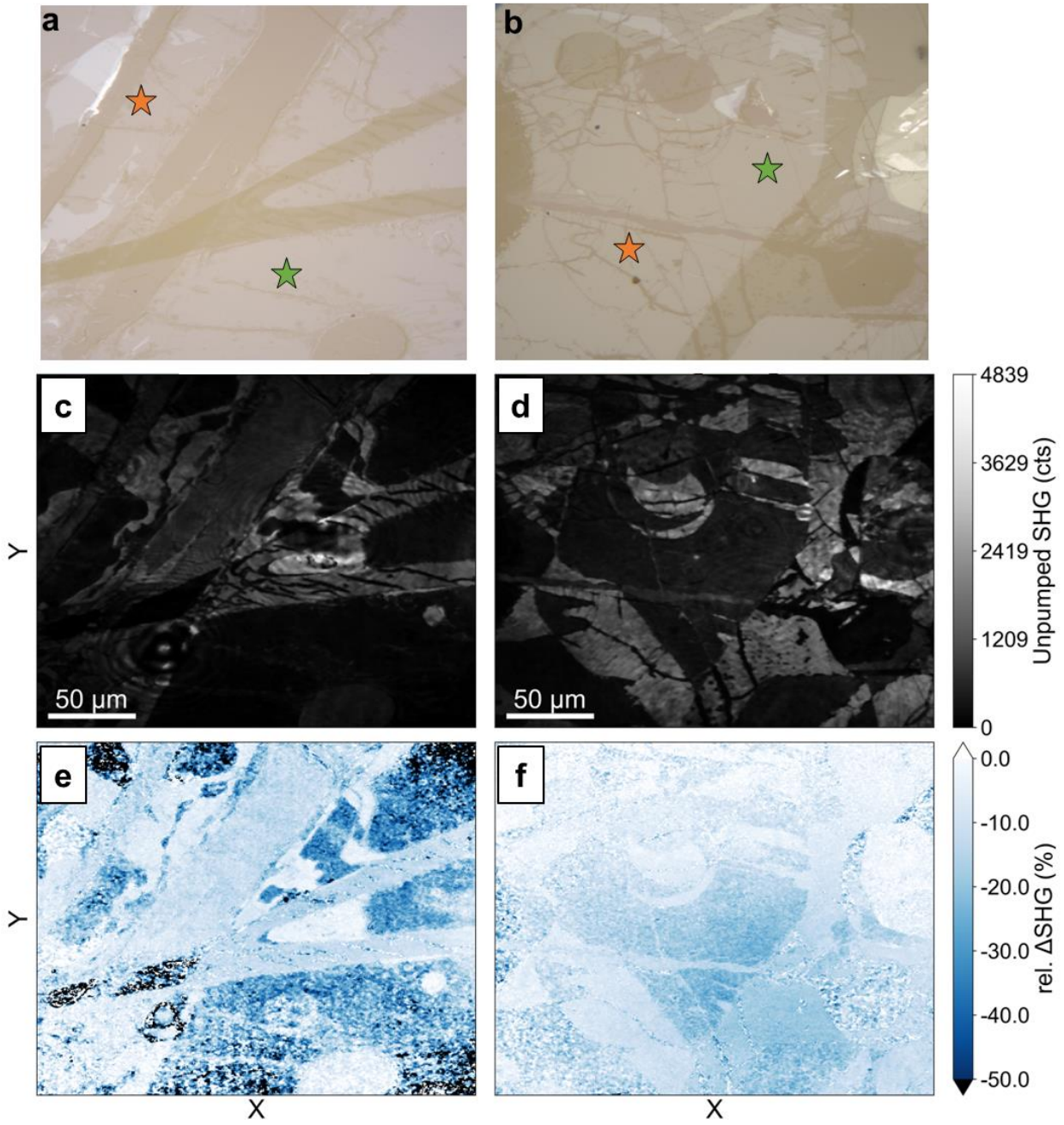

Figure S5 | Optical, unpumped, and pumped SHG images of WS_2/MoS_2 and WS_2/WSe_2 samples. The left column (a, c, e) is the WS_2/MoS_2 sample and the right column (b, d, f) is the WS_2/WSe_2 sample. Top row are the optical images, middle row is the unpumped SHG, and the bottom row is the relative ΔSHG. The orange and green stars in the optical images represent domains that behave similarly to one another and to the orange and green starts in Figure 19a of the main text. Green star: higher unpumped SHG intensity, smaller relative pumped SHG intensity. Orange star: lower unpumped SHG intensity, higher relative pumped SHG intensity.

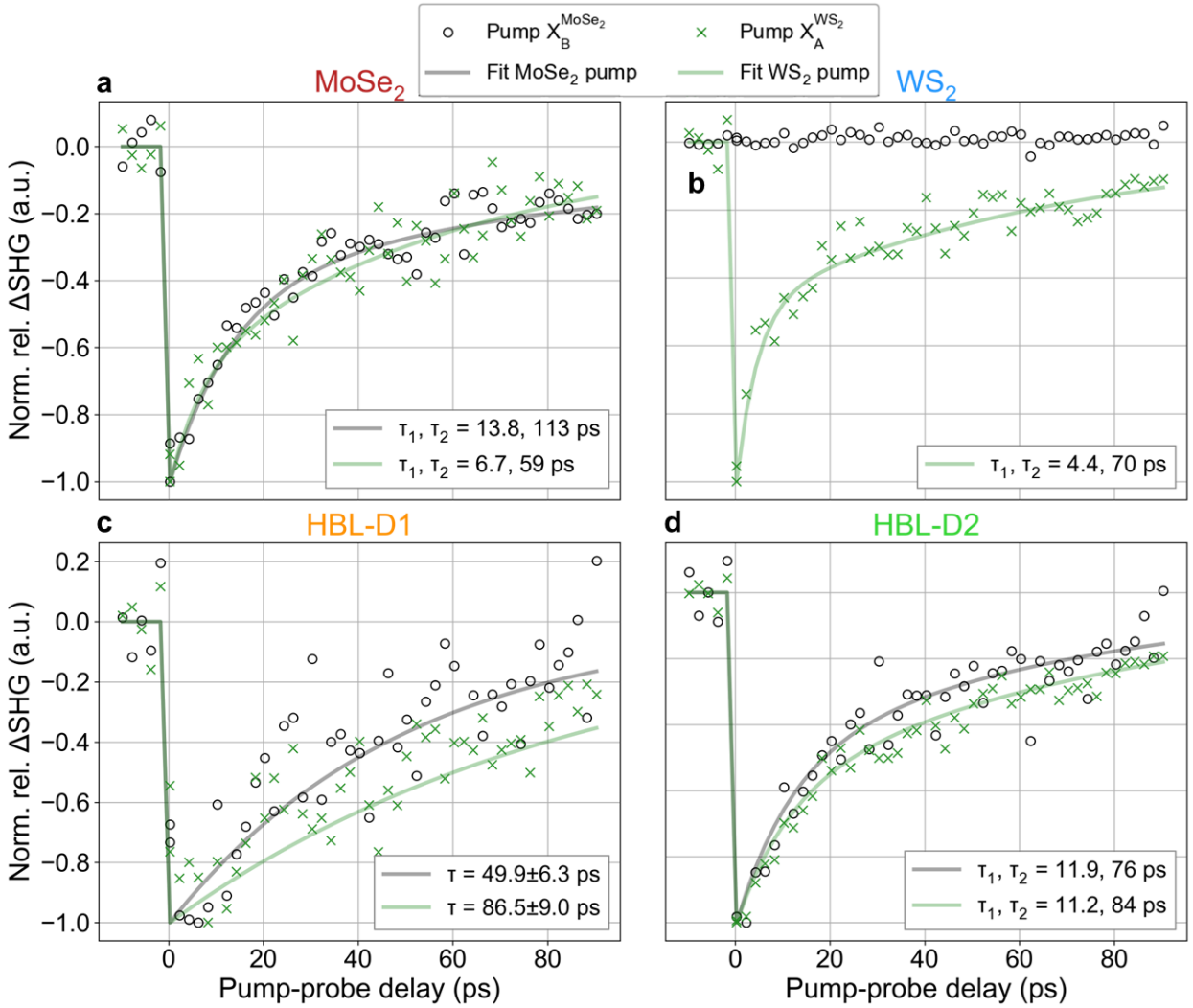

Figure S6 | Comparison of pure 1L and HBL population dynamics for two different pump energies. The black circles indicate a $MoSe_2$ B exciton pump and the green crosses indicate a WS_2 A exciton pump. The solid lines are biexponential fits of the data with the corresponding marker color. All delay traces are spatially averaged over 1000s of pixels. a) delay traces for the pure $MoSe_2$ region, b) delay traces for the pure WS_2 region, c) delay traces for HBL-D1, and d) delay traces for HBL-D2.

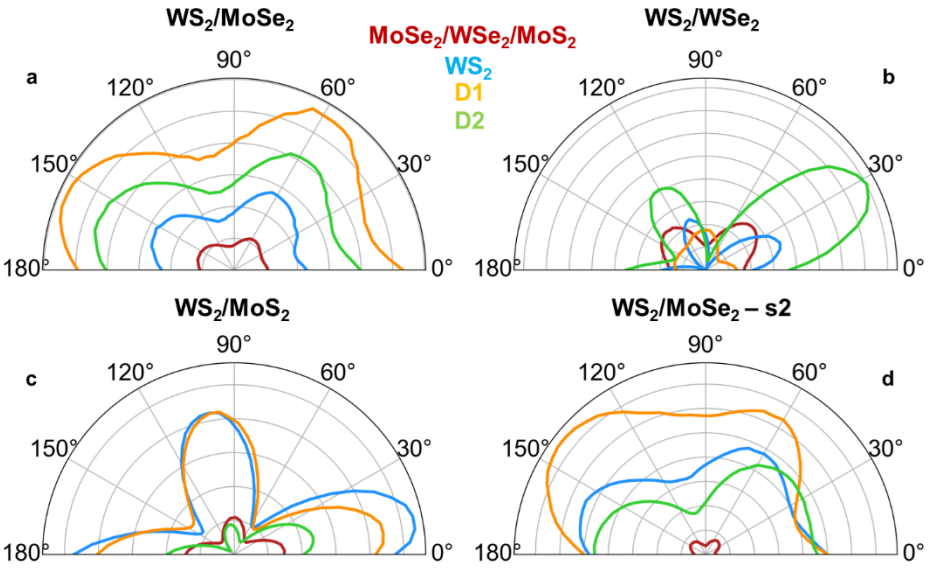

Figure S7 | Spatially averaged polar plots for the four different samples investigated in this study. a) $WS_2/MoSe_2$ sample highlighted in the main text, b) WS_2/WSe_2, c) WS_2/MoS_2, and d) the second $WS_2/MoSe_2$ sample. The legend in the upper center of the figure correlates color of trace to region in the sample. All polar plots were taken with an identical optical setup described in the Methods section of the main text. Note the WS_2 trace in panel b where nodes fall to zero intensity and the four-lobed pattern that is expected for the polarization setup, validating the non-conventional behavior seen in the other regions and other samples.

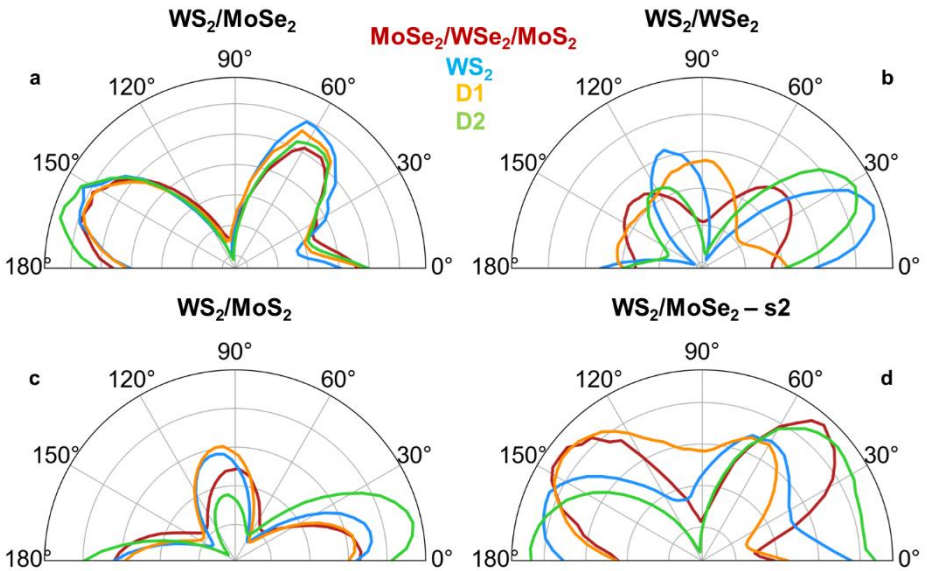

Figure S8 | Polar plots from Figure S7 but with the signal offset to enhance the contrast between lobes and nodes. a) $WS_2/MoSe_2$ sample highlighted in the main text, b) WS_2/WSe_2, c) WS_2/MoS_2, and d) the second $WS_2/MoSe_2$ sample. Each polar trace was subtracted and divided by its mean value to enhance the contrast between lobes and nodes.

3 Development of all-optical probes of charge carrier occupation at non-direct-bandgap states

Ever since I joined the Wright Group, it's been a goal to collect MR-CMDS spectra whose peaks originate, unambiguously, from various momentum points in the BZ (we've called it momentum-selective, or *k*-selective, spectroscopy). This chapter presents work toward that goal. Section 3.1 builds on the work done by my mentor in the Wright Group, Dr. Darien Morrow, by scanning higher into the CB of TMDs. I performed two-color sum-frequency generation spectroscopy (SFG) on a variety of TMD samples to look for resonance enhancement from non-direct-gap states (states that aren't made up of the VBM and CBM at the direct-gap momentum point). Section 3.1.1 presents SFG measurements on a CVD-grown 1L WS_2 sample. That section is written as the first draft of a journal article which will be submitted for publication in the near future. The remaining data in Section 3.1 are from exfoliated TMD samples and corroborate the CVD results. In Section 3.2, I continue the theme of investigating non-direct-gap states but in a transient, rather than steady state, manner by using SFG as a probe to study the mechanism by which charge transfers between TMD layers in a HBL sample. The results from the transient studies were not consistent with literature results. However, there are interesting aspects of that data that motivate further investigations.

3.1 Steady state method: Homodyned two-color sum frequency generation (2D SFG) spectroscopy

3.1.1 Manuscript: Spectral decongestion of high-lying conduction band states through momentum-selective spectroscopy in monolayer WS_2

Authors: Jason M. Scheeler[1], Dan D. Kohler[1], Yuzhou Zhao[1], Song Jin[1], John C. Wright[1]

[1]University of Wisconsin-Madison, Department of Chemistry

Introduction

Semiconducting materials systems with direct bandgaps are more popular in photovoltaic applications than their indirect-bandgap counterparts because of their strong absorption of light. A photon that's absorbed by a solid-state material has negligible momentum compared to the electron it excites, thereby only allowing optical transitions that conserve momentum. When a photon's energy is equal to the direct-bandgap energy, it creates a spatially correlated electron-hole pair called an exciton that's bound together by the Coulombic force. Depending on the material system, the exciton can be tightly or loosely bound. Lead halide perovskites (LHP), for example, host loosely bound excitons where they separate easily into the constituent electrons and holes. This facile separation coupled with a direct bandgap makes them promising materials for charge collection applications such as solar cells. [112] Conversely, monolayers of transition metal dichalcogenides (1L TMDs) host tightly bound excitons even well-beyond room temperature. This makes TMDs a useful model system for studying fundamental exotic excitonic phenomena such as moiré physics[87,88] as well as being attractive to use in next-generation

electronic and optoelectronic devices. Such excitonic devices show great promise for combining optical data transmission and electrical processing[113] and ultra-efficient power consumption.[86]

Excitons that reside at the conduction band maximum (CBM) and valence band minimum (VBM) obviously do not exist in a vacuum. There are states that exist above and below in energy at the direct-gap momentum point that affect its occupation. When a material absorbs a photon with energy higher than the bandgap, like when an LHP absorbs a UV photon from the sun, the excited electron will want to funnel down in energy to the CBM and there will be a characteristic time scale with which that happens. Even if the photon has an energy equal to the materials' direct bandgap, it's not guaranteed the charge carriers will remain at the CBM and VBM. It's been shown in 1L TMDs that there are sub-gap states where excited carriers may relax to and makes photoemission spin-forbidden, thus significantly limiting their efficiency.[31] Charge carriers can also scatter to states that are close in energy to the direct-gap state but reside at different momentum points. It's been demonstrated that momentum-forbidden dark states in TMDs can act as a charge carrier sink of direct-gap excitons and severely limit their photoluminescence.[114] Furthermore, non-direct-gap momentum points play a vital role in the charge transfer mechanism of TMD heterobilayers which will be detailed in Section 3.2.[115] Needless to say, non-direct-gap states have a large influence on the occupation of the direct-gap state, making it crucial to have probes of the non-direct-gap states to help fully realize the potential of the various photovoltaic applications of semiconducting materials systems.

Currently, the gold standard for experimentally probing the band structure of a solid-state material is angle-resolved photoemission spectroscopy (ARPES).[116] ARPES uses a pulsed XUV laser source to eject electrons from the material and by resolving the angle at which the electron is ejected, it provides unambiguous information on the electron's energy-momentum correlation.

Historically, the primary way to do ARPES measurements was to submit a proposal for instrument time at a synchrotron facility. Fortunately, the past two decades or so has seen tabletop XUV sources become more popular.[117,118] Even so, manipulating XUV light requires special optics and ultra-high vacuum capabilities which is expensive and complex.

Ultrafast laser systems, on the other hand, are ubiquitous among research institutions. Coherent multidimensional spectroscopy (CMDS) is an ultrafast laser technique that impinges multiple pulsed beams on a sample and has successfully been shown to interrogate non-direct-gap states in semiconducting solid-state systems.[27,119] Figure 22 outlines how CMDS can be applied to probe arbitrary points in the Brillouin zone (BZ) of a solid-state material. Figure 22a shows a simple band structure consisting of three bands (VB0, CB0, and CB1) with varying curvature. $\hbar\omega_A$ and $\hbar\omega_B$ represent two laser pulses interacting with the sample. The numbers at the top of Figure 22a indicate the three different momentum points at which the lasers interact. Optical transitions must conserve momentum so $\hbar\omega_A$ defines where the carriers are excited in momentum space. Both laser energies are scanned to create a CMDS spectrum which is shown in Figure 22b. Where the peaks occur in the spectrum correlate with the resonant transitions in the band structure. For example, $\hbar\omega_A$ is higher in energy in both Pathway 1 and Pathway 3 than its energy in Pathway 2 and therefore the Peaks 1 and 3 are shown at a higher energy along the $\hbar\omega_A$ axis than Peak 2. $\hbar\omega_B$ increases monotonically from Pathway 1 to Pathway 3 which is reflected in the CMDS spectrum by Peaks 1, 2, and 3 increasing in energy along the $\hbar\omega_B$ axis.

In this way, using CMDS would act as an all-optical analogue to ARPES and retrieve the same momentum-resolved information. In practice, however, it is not this straightforward. Similar to molecular liquid-state samples, there is inhomogeneous broadening that can cause constructive

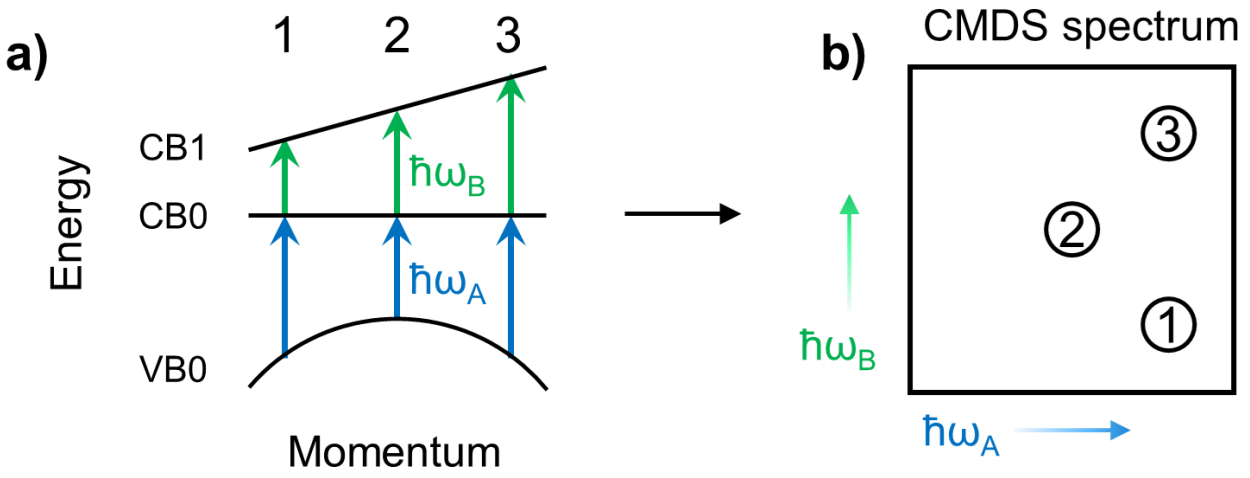

Figure 22 | Momentum-selective spectroscopy schematic. 1) cartoon band structure with three bands VB0, CB0, and CB1. The blue and green arrows represent two separate laser interactions with the sample. The numbers on top denote spectroscopic pathways at different momentum points. b) corresponding CMDS spectrum based on the three transitions shown in a). $\hbar\omega_A$ in both Pathway 1 and 3 have a greater energy than $\hbar\omega_A$ in Pathway 2 so Peaks 1 and 3 are shown at a higher energy than Peak 2 along the $\hbar\omega_A$ axis. The $\hbar\omega_B$ energy increases monotonically from Pathway 1 to Pathway 3 which is indicated in the spectrum as Peaks 1, 2, and 3 increase in energy along the $\hbar\omega_B$ axis.

or destructive interference of the nonlinear signal of interest. One must consider *all* the optical transitions in the BZ, not just the transitions at the high symmetry points that are commonly seen in band structure diagrams. The CMDS method used and the energy correlations between the bands that are coupled to one another play crucial roles in seeing nonlinear signal. For example, a sum-frequency generation (SFG) pathway will have constructive interference between bands that have a positive energy correlation and destructive interference for anti-correlated bands. The opposite is true for a difference-frequency generation (DFG) pathway.[120–122]

In this work, we present an example of multi-resonant CMDS providing momentum-resolved information at the non-direct-gap transition by performing two-color SFG spectroscopy on a CVD-grown sample of 1L WS_2. An optical micrograph of the studied sample is shown in Figure 23a. Figure 24 illustrates the band structure and experimental setup for the SFG measurements.[123] The band structure incorporates spin-orbit coupling which affects VB0, CB0, and CB2; the blue and red lines for these bands denote opposite spin states. We utilize the strong transition dipole of the direct-bandgap transition (Figure 23b, light blue line) by having one laser's energy range resonant with the A exciton (Figure 24a, orange arrow). The A exciton originates at the K point in the BZ (VB0→CB0). An additional laser is then frequency-scanned to look for resonance enhancement of high-lying CB states (VB0→CB1 or VB0→CB2) at the direct-gap momentum point (Figure 24a, pink arrow). In the 2D SFG spectrum, we find strong resonance enhancement from a CB two bands above the CBM (Figure 24a, purple arrow) as well as intense SFG output from a band nesting transition (Figure 24a, blue arrow). This work

establishes SFG spectroscopy as a viable method to learn about the energy landscape of states near the direct-gap state that will influence its occupation.

Experimental

Sample synthesis and characterization

Following the method in Ref [124], the 1L WS_2 sample was prepared using water vapor assisted chemical vapor transport by heating 100 mg WS_2 power to 1200°C at 800 torr in a tube furnace. In the tube furnace, water vapor was produced by heating 1 g $CaSO_4 \cdot 2H_2O$ powder to 150°C using heating tape wrapped around the tube furnace. 100 sccm Ar was used as the carrier gas during the reaction.

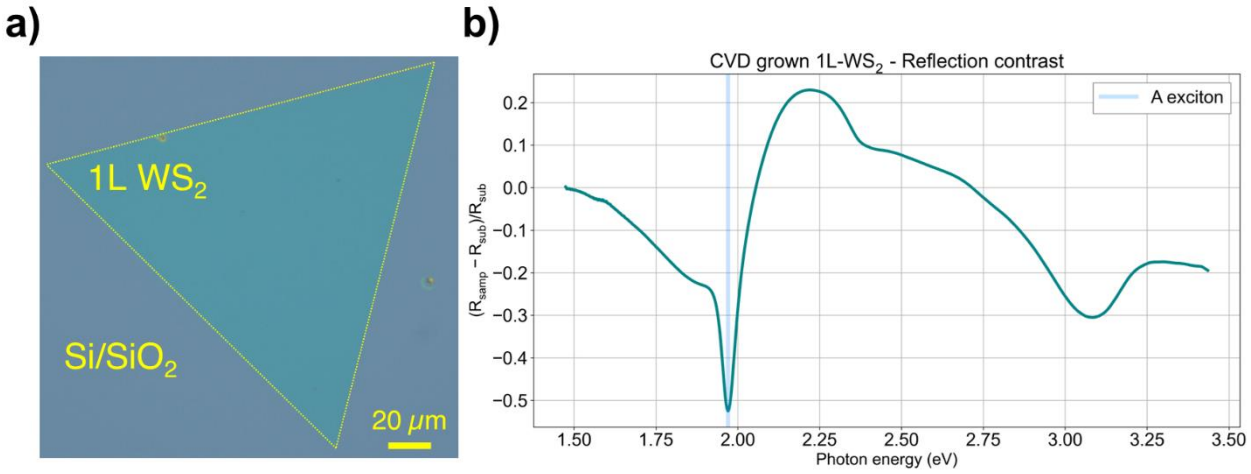

Figure 23 | Characterization of CVD-grown 1L WS_2 sample. a) optical micrograph of 1L $WS2_2$ on top of a protected silicon substrate. b) reflection contrast spectrum highlighted by the sharp A exciton resonance at 1.98 eV.

The reflection contrast measurements were taken by focusing white light (Dolan-Jenner Fiber-Lite Model 190) through a long-working-distance 20X microscope objective (Mitutoyo) onto the sample. The reflected light, collected through the same objective, was focused onto the slit of a

homebuilt transmission-based imaging spectrograph by a 200-mm focal length tube lens (ThorLabs, TTL200). The imaged light is spectrally dispersed by a 200 g/mm transmission grating (Richardson Gratings, MKS-Newport) and focused onto an electron-multiplying CCD (Princeton Instruments, ProEM-HS: 512BX3).

SFG measurements

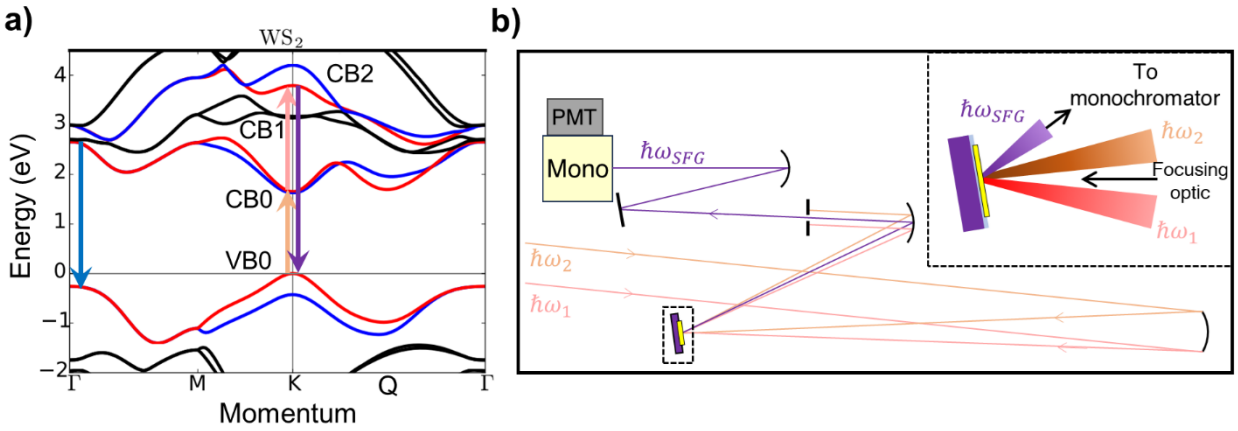

Figure 24 | Experimental setup for the 2D SFG experiment. a) 1L WS_2 band structure with spin-orbit coupling included (band structure adapted from Ref 123). The orange arrow represents $\hbar\omega_2$ and the pink arrow represents $\hbar\omega_1$. As DFT methods do not normally calculate band gap energies correctly, the length of each arrow does not correspond exactly with the energies of the transitions. Rather, they are meant to show the initial and final states as a result of the field interacting with the WS_2 sample. b) the optical layout. All beams are collected in the *epi* direction and the SFG output is spatially isolated with an aperture. Inset: zoomed-in view of the excitation beams interacting with the sample. For sake of clarity, the reflections of the excitation beams are not shown.

The upstream experimental setup uses a regenerative amplifier seeded by an ultrafast oscillator (Spitfire and Tsunami, respectively; SpectraPhysics). Pulses exit the amplifier centered at 1.55 eV with a temporal pulse duration of ~35 fs at a repetition rate of 1 kHz. The amplifier output is split in half and each arm is sent to a separate optical parametric amplifier (OPA; Topas-C, Light Conversion) which are denoted $\hbar\omega_1$ and $\hbar\omega_2$ hereafter. Subsequent nonlinear mixing crystals are

placed after each OPA such that $\hbar\omega_1$ is tunable from 1.15-1.55 eV and $\hbar\omega_2$ is tunable from 1.60-2.10 eV. Further polarization and color filters are placed into the beam line to reject signal and idler beams and isolate the energy range of interest.

The downstream optical layout is illustrated in Figure 24b. The vertically polarized OPA beams are sent to a 1 m-focal length concave mirror that focuses the beams onto the sample in a noncollinear excitation geometry. $\hbar\omega_1$ has a ~400 μm diameter and $\hbar\omega_2$ has a ~200 μm diameter at the sample. All beams are collected in the *epi* direction. The signal beam is spatially isolated with an aperture and is sent to a monochromator (MicroHR, Horiba). The monochromator energy tracks the sum of the two input beams, $\hbar\omega_{SFG}=\hbar\omega_1+\hbar\omega_2$, which is sent to a PMT (C313034-A, Hamamatsu) for detection. Due to the fast dephasing time of the WS_2 A exciton at room temperature, there is no signal beyond temporal pulse overlap. Accordingly, all spectra shown in this work are at zero delay. Due to transmissive optics in both OPA beam lines before the sample, different energy setpoints arrive at the sample at different delay times. We empirically correct for this by taking a reference scan of a non-resonant sample to determine the arrival time of each energy setpoint for both $\hbar\omega_1$ and $\hbar\omega_2$. These spectral-delay offsets are incorporated into our data acquisition software and are automated. All hardware was controlled through the yaq protocol[104]; experiments were orchestrated using an in-house deployment of Bluesky.[105]

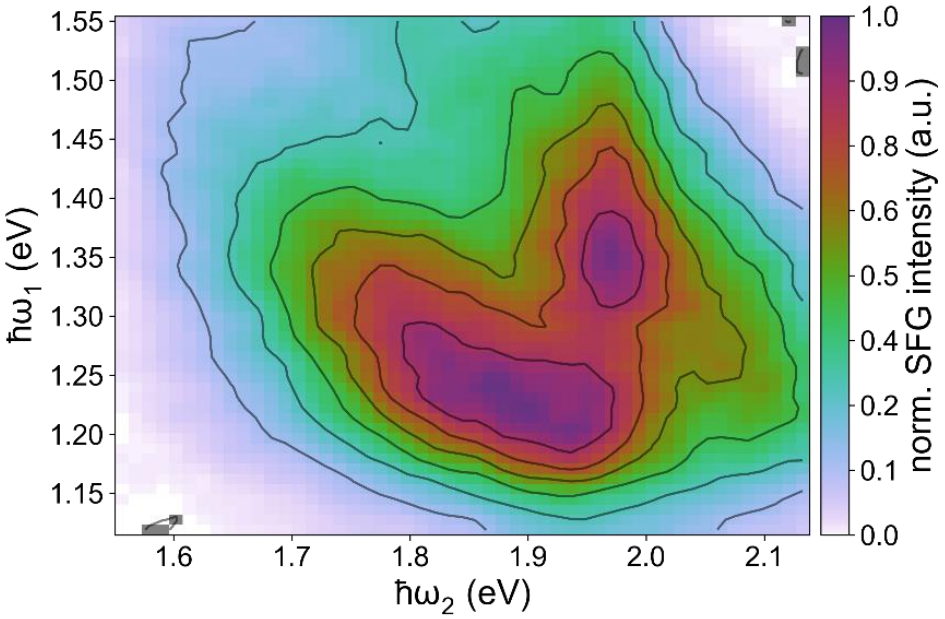

Figure 25 | 2D SFG spectrum of 1L WS_2. The grayed pixels are negative signal values that oscillate about the average signal baseline.

Results and Discussion

The raw 2D SFG spectrum shown in Figure 25 has two features of interest. The first is a doubly resonant feature peaked at ($\hbar\omega_2$, $\hbar\omega_1$) = (1.98, 1.34) eV which contains two sub-features. The first sub-feature is vertically elongated along the $\hbar\omega_1$ axis but well-defined along $\hbar\omega_2$. Because the A exciton of 1L WS_2 is at 1.98 eV, there must be a state located 1.34 eV above the CBM that causes the double resonance. The second sub-feature is negatively sloped and has a constant output color of ~3.32 eV (the contours in the upper left of the double-resonance peak [bluer $\hbar\omega_1$, redder $\hbar\omega_2$] and lower right [redder $\hbar\omega_1$, bluer $\hbar\omega_2$] act as a guide to the eye to locate this negatively sloped feature). These features arise from the K point in the BZ. Their wave mixing energy level diagrams (WMELs) along with the frequency domain $\chi^{(2)}$ expression that governs

the output intensity are shown in Figure 26. The vertical sub-feature occurs from Pathway α (Figure 26a, top) when $\hbar\omega_2$ interacts first: the intense absorption at the direct-gap K point defines where the excitons are at in momentum space. When $\hbar\omega_1$ interacts second, the electrons at the CBM get promoted either to virtual states or higher-energy CB states. The SFG signal is

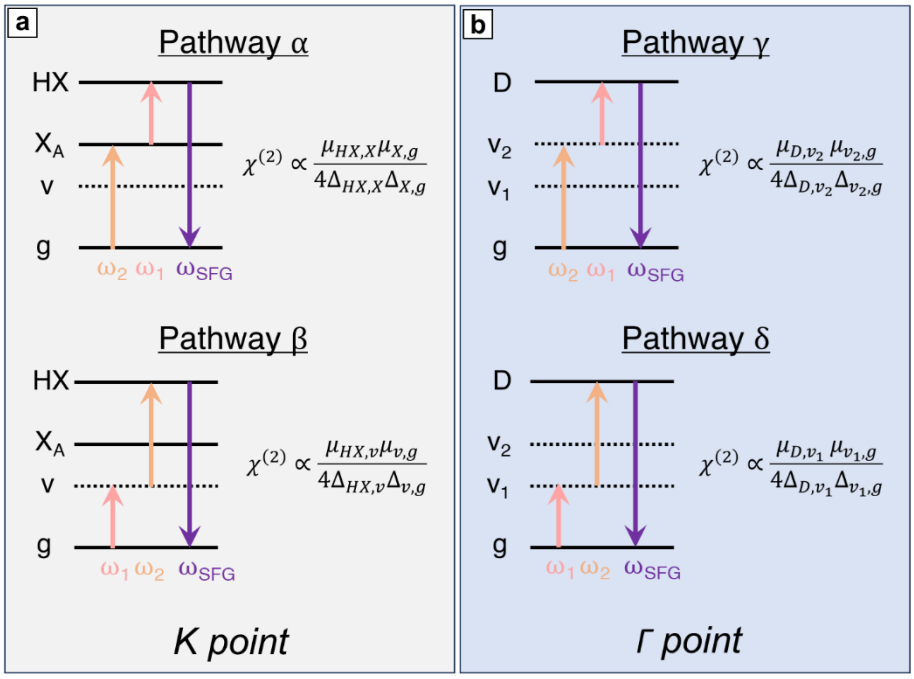

Figure 26 | WMEL diagrams for the two time orderings in the SFG experiment at the a) K point and b) Γ point. The pathways on top describe $\hbar\omega_2$ interacting first and the pathways on bottom describe $\hbar\omega_1$ interacting first. To the right of each pathway is the frequency domain $\chi^{(2)}$ expression that dictates the SFG output intensity. μ_{ab} is the transition dipole from state b to state a and $\Delta_{ab}=\omega_{ab}-\omega_{laser}+i\Gamma_{ab}$ is the detuning factor which relates the material resonance to the energy of the laser and accounts for the material's resonance linewidth, Γ_{ab}.

enhanced when $\hbar\omega_1$ is resonant with a state 1.34 eV above the CBM (and 3.32 eV above the VBM). We denote this high-energy state as HX. The HX state has been observed experimentally in two others semiconducting TMDs[96] but our work marks the first time, to the authors' knowledge, that it's been seen in 1L WS_2. Due to the strong A exciton transition dipole in 1L

WS_2, there is still signal enhancement when $\hbar\omega_1$ interacts with virtual states (i.e. when $\hbar\omega_1$=1.40-1.55 eV). The diagonal sub-feature at the 3.32 eV constant output color results from Pathway β (Figure 26a, bottom) where $\hbar\omega_1$ interacts with the sample first: electrons are promoted from VB0 theoretically at all momentum points. SFG signal will get enhanced when $\hbar\omega_1$+ $\hbar\omega_2$ is resonant with a high-lying CB state which occurs at the HX energy. The signal contribution to Pathway β will be less than Pathway α because the A exciton state is not directly visited. However, because of Pathway α we know that HX originates from the K point in momentum space.

The second feature in the SFG spectrum is strongest along the $\hbar\omega_1$ axis from 1.20-1.28 eV and along the $\hbar\omega_2$ axis from 1.80-1.98 eV (Figure 26). The feature is negatively sloped and occurs at a constant output color of ~3.08 eV. This output energy is easiest to pick out for the bluer $\hbar\omega_1$, redder $\hbar\omega_2$ region of the feature; the redder $\hbar\omega_1$, bluer $\hbar\omega_2$ part of the feature runs into the doubly resonant feature which results in interference between the two emitting states. This interference causes the feature to level out, making the output energy harder to interpret for this region of the singly resonant feature. This feature is spectrally broad and at a high energy (relative to A and B excitons) suggesting this feature comes from the well-known band nesting regions of the Brillouin zone in TMDs. We assign this feature to the so-called D exciton as its energy matches the energy of that reported in the literature.[23,125] The WMELs for the two time orderings at this momentum point are shown in Figure 26b. Like the feature that results from Pathway β, Pathways γ and δ contain a single resonance and are only resonant when $\hbar\omega_1$+ $\hbar\omega_2$ is equal to the D exciton energy.

Previous work in our group shows that first-order and second-order spectroscopies enhance transitions that arise from a large joint density of states (JDOS) while third-order spectroscopies enhance transitions that arise from a strong transition dipole.[5] It's intriguing to note, then, that the

intensity of both the singly and doubly resonant features are nominally equal. Since the SFG used in this work is a second-order process and should therefore enhance the singly resonant feature over the doubly resonant feature, this highlights the strength of the CB0→CB2 transition dipole. In the same vein, calculations by Lin *et al.* demonstrate a congested absorption spectrum in the 2.7-3.6 eV when transitions from the VBM to all CBs in the BZ are considered.[126] However, when a small range of momentum points centered at the K point and only a few CBs are considered, the absorption spectrum becomes significantly less congested. $\hbar\omega_2$ being resonant with the A exciton is akin to the "windowing" around the K point in the calculations and reflects the important role of excitonic effects.

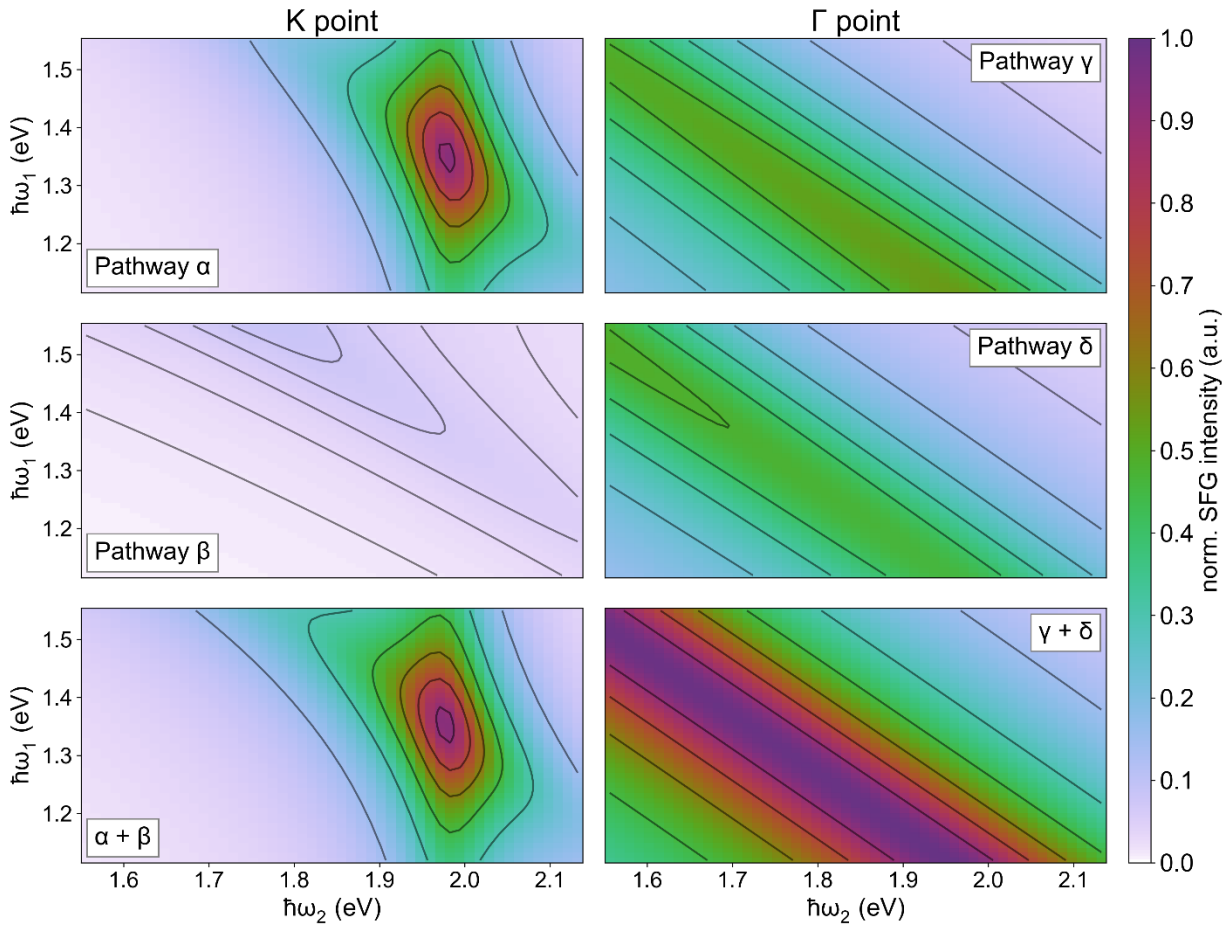

Figure 27 | Contributions from individual pathways to the overall $\chi^{(2)}$. The left-hand column plots the contributions from the K point and the right-hand column plots the contributions from the Γ point. The top row has $\hbar\omega_2$ interact first and $\hbar\omega_1$ second, the second row flips the laser interactions, and the third row is the result of adding the first and second row plots together.

In Figure 27, we use the $\chi^{(2)}$ expressions from Figure 26 to simulate the contributions from both time orderings at the relevant momentum points. The left-hand column plots the K point $\chi^{(2)}$ contributions and the right-hand column plots the Γ point $\chi^{(2)}$ contributions. The bottom row plots the addition of the two pathways in the two rows above it. The plots are globally normalized to the largest value in the six-plot set.

Comparison between the contributions from Pathway α and β prove that α dominates the SFG signal at the K point. This is unsurprising as Pathway α is in resonance with the WS_2 A exciton while Pathway β is not. In the Pathway β plot, as $\hbar\omega_1$ increases in energy and gets closer to the HX resonance at ~3.32 eV, the SFG signal values increases. This results in slight asymmetry in the overall doubly resonant line shape that adds the two time orderings together (α+β, bottom left plot, Figure 27). The line shapes for Pathways γ and δ (Figure 27, right column, top and middle plots) is similar to the line shape for Pathway β. Both Pathway γ and Pathway δ have a line of constant output color at the D exciton resonance at ~3.08 eV. The SFG signal value for Pathway γ is slightly greater than for Pathway δ because $\hbar\omega_2$ interacts with the sample first and is closer to resonance than $\hbar\omega_1$. Adding the two pathways together (γ+δ, bottom right, Figure 27) results in the same line shape of a constant output color at 3.08 eV. We compare the simulation to the experiment in Figure 28.

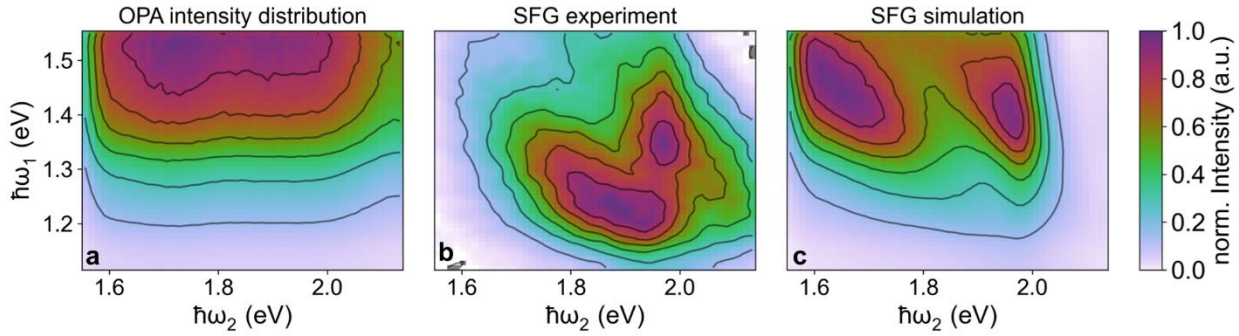

Figure 28 | Comparison between experimental and simulated SFG spectrum considering the OPA intensity distribution. a) OPA intensity distribution as a function of $\hbar\omega_1$ and $\hbar\omega_2$. $\hbar\omega_2$'s intensity distribution is mostly flat and dies off at the edges. $\hbar\omega_1$'s intensity distribution increases monotonically as the colors go from red to blue. b) experimental SFG spectrum duplicated from Figure 25 for direct comparison. Greyed out pixels are negative signal values. c) simulated SFG spectrum. This spectrum results from adding up all contributions at both K and Γ points and multiplying by the OPA intensity distribution in panel a).

The OPA intensity distributions for $\hbar\omega_2$ and $\hbar\omega_1$, taken concurrently with the SFG data, are shown in Figure 28a. The intensity of $\hbar\omega_2$ is flat across much of its range but dies off significantly at both the red and blue edges. The intensity of $\hbar\omega_1$ increases monotonically as the colors get bluer. The SFG intensity depends on the product of the two intensities. It's instructive to consider this intensity distribution when analyzing the correspondence between experiment and simulation. Figure 28b is a duplication of the experimental SFG spectrum from Figure 25. Figure 28c is the simulated SFG spectrum. We calculate it by adding Pathways α-δ and multiplying the resulting 2D spectrum by the OPA intensity distribution. The simulated spectrum correctly reproduces the two peaks seen in the experiment and their relative peak intensities. However, both the peaks in the simulated spectrum occur at bluer $\hbar\omega_1$ values compared to experiment. Because the singly resonant feature from the D exciton runs anti-diagonally (i.e. depends on both $\hbar\omega_1$ and $\hbar\omega_2$), it appears in the simulation at redder $\hbar\omega_2$ values than the experiment. Overall, the simulation over-emphasizes the $\hbar\omega_1$ intensity distribution asymmetry, but it captures well the relative contribution from both K and Γ points in the experimental SFG spectrum.

Conclusion

We performed two-color SFG spectroscopy on a CVD-grown 1L WS_2 sample. One laser being resonant with the direct-gap transition acts as a filter to decongest the SFG spectrum and reveals the energy of the HX state at 3.32 eV, 1.34 eV higher in energy than the CBM at the K point. We also found considerable SFG output when $\hbar\omega_1 + \hbar\omega_2$ was resonant with the D exciton located at the Γ point. We used simple frequency-domain expressions in the driven limit to model the SFG contributions at the K and Γ momentum points which qualitatively agrees with experiment. The multi-resonant sum-frequency spectroscopy technique herein presents a useful way to map out

the energy landscape of high-energy states at the direct-gap momentum point for solid-state systems that have large excitonic transition dipoles. The technique can also be applied to third-order spectroscopies and probing VBs that are lower in energy than the VBM when that is more useful information for improving photovoltaic performance.[127]

3.1.2 Exfoliated 1L WS_2 and HBLs

While there are small differences between the electronic and optical properties of CVD-grown and exfoliated 1L TMDs, their electronic structures are similar. It's useful then to perform the 2D SFG experiments on an exfoliated sample so confidence can be put into the CVD results. To this end, we performed SFG experiments on two separate exfoliated 1L WS_2 samples on fused silica substrates. The only experimental difference between the CVD and exfoliated samples is the SFG output is collected in transmission for the exfoliated sample. The fused silica substrate is not $\chi^{(2)}$ active and therefore does not contribute to the SFG output. The results of the SFG experiments on the exfoliated samples are compared to the CVD results in Figure 29. The CVD

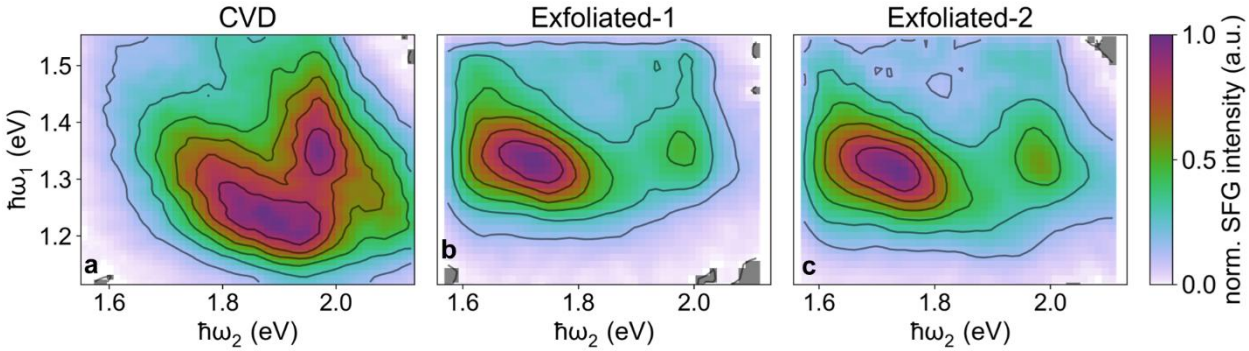

Figure 29 | Comparison of 2D SFG spectra for multiple 1L WS_2 samples synthesized two different ways. a) CVD-grown (as in Figure 25) and b, c) exfoliated from bulk WS_2. The grey pixels indicate negative signal values.

SFG spectrum (Figure 29a) is the same as the spectrum shown in Figure 25. Both exfoliated SFG

spectra (Figures 29b, c) display the two prominent features discussed in Section 3.1.1. The first one is the doubly resonant peak at ($\hbar\omega_2$, $\hbar\omega_1$) = (1.98, 1.34) eV. The vertical and diagonal elongation of the doubly resonant feature is less prominent than the CVD case but there are still slight signal enhancements in these sub-feature areas, particularly above the doubly resonant peak (at $\hbar\omega_2$=1.98, $\hbar\omega_1$=1.42-1.52 eV). The circularity of the double-resonance peak suggests both the A exciton (VBM→CBM) and HX (CB0→CB2) transition dipoles are not as strong in the exfoliated samples as they are in the CVD sample.

The singly resonant transition arising from the Γ point is seen in the exfoliated samples as in the CVD sample albeit the peak intensity is centered around bluer $\hbar\omega_1$ and redder $\hbar\omega_2$ colors (it shifts up and to the left relative to the CVD feature). This feature again is assigned to the D exciton. The difference in peak location for the two synthetic methods can primarily be attributed to the CVD and exfoliated experiments being done in two separate experimental sessions. In particular, the intensity for the redder portion of the scanned $\hbar\omega_1$ range (1.3 eV and redder) was about 1/4 of the intensity as it was for the CVD experiments. This is a result of the tuning process for OPAs in the Wright Group which can cause variability in OPA performance. Again, because the feature is diagonal, it results in shifts in both spectral axes. The constant output color of the D exciton feature is ~3.05 eV, only slightly less than the CVD energy of 3.08 eV. It's also worth noting the relative intensity decrease for the doubly resonant feature in the exfoliated samples. The doubly resonant feature is about ½ the intensity of the D exciton feature whereas the two features were at similar intensity levels for the CVD sample. This likely results from a decrease in transition dipole strength of the A exciton in the exfoliated sample CVD-grown TMD samples are typically of a higher quality than their exfoliated counterparts.

To corroborate further the SFG results seen in the 1L samples, we performed the same SFG experiment on exfoliated HBL samples, one consisting of 1L WS_2 and 1L MoS_2 and the other consisting of 1L WS_2 and 1L WSe_2. It is unknown which layer is on top and which layer is on bottom in these samples. This allowed us to again test the technique and make sure similar types of features (single resonance from Γ point and double resonance from K point) are seen in the other TMDs. The HBL SFG spectra are shown in Figure 30. The WS_2/MoS_2 spectrum (Figure 30a) has *two* doubly resonant features compared to one in the 1L WS_2 spectrum. One of the doubly resonant features occurs at ($\hbar\omega_2$, $\hbar\omega_1$) = (1.94, 1.38) eV and the other occurs at ($\hbar\omega_2$, $\hbar\omega_1$) = (1.81, 1.48) eV. The 1.38 eV feature is assigned to the HX state in WS_2 and the 1.48 eV feature is assigned to the HX state in MoS_2 since the peak aligns with the energy of the MoS_2 A exciton at 1.83 eV (red arrow, Figure 30a). It's likely the most intense feature of this SFG spectrum (the D exciton feature) is obfuscating the true energy of the CB0→CB2 transition in MoS_2 as those

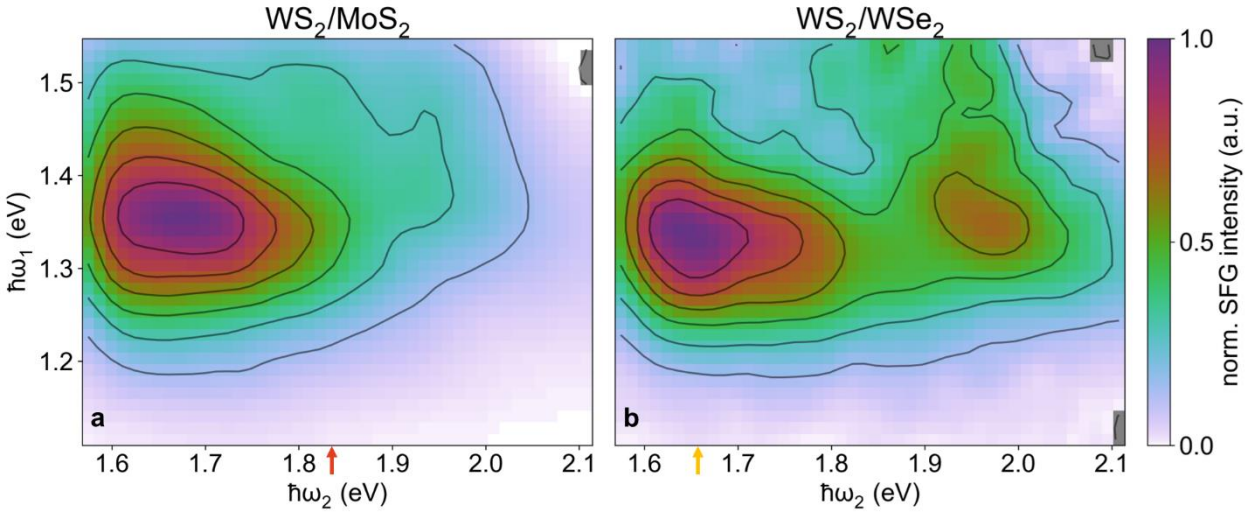

Figure 30 | 2D SFG spectra for exfoliated HBLs. a) WS_2/MoS_2 and b) WS_2/WSe_2. The red (orange) arrow below the spectrum indicates the $\hbar\omega_2$ energy that's equal to the A exciton energy for the MoS_2 (WSe_2) layer. The grey pixels represent negative signal values.

features run together. However, this is inferred from the 1L WS_2 measurements and is not certain – the HX state in MoS_2 may indeed lie 1.48 eV above the CBM. The singly resonant feature from the Γ point is about 3x as intense as both the doubly resonant features. This feature is still diagonal albeit with a smaller slope than any of the 1L samples. Band structure calculations of WS_2/MoS_2 HBLs show the VBM at the Γ point is hybridized between both layers, and the CBM at the Γ point that's mostly MoS_2 in character is ~0.2 eV lower in energy than the CBM that's mostly WS_2 in character (see Figure 33a for the band structure).[115] Therefore, we expect the MoS_2 layer to contribute to the singly resonant feature with a constant output color that's ~0.2 eV less than the D exciton contribution from the WS_2 layer. These two features run into one another which causes the resulting feature in Figure 30a to be more horizontal compared to the analogous features in the 1L samples.

Like the WS_2/MoS_2 sample, the WS_2/WSe_2 SFG spectrum (Figure 30b) has two double resonances with the second one being admittedly harder to see. The first double resonance is the familiar one originating from the WS_2 layer at $(\hbar\omega_2, \hbar\omega_1)$ = (1.97, 1.36) eV. The diagonal character of the doubly resonant feature (constant output color of 1.97+1.36=3.33 eV) is more pronounced in this spectrum than the other exfoliated SFG spectra. The second double resonance occurs at $(\hbar\omega_2, \hbar\omega_1)$ = (1.66, 1.33) eV. This one is harder to see because it falls on top of the Γ point single resonance. The contour with the highest signal value for this feature is more circular compared to all the other SFG spectra where the highest contour is more ovular. This, coupled with the fact that the more intense part of the feature overlaps well with the A exciton of WSe_2, makes me confident this is indeed a double resonance. The two double resonances dominate this spectrum making any single resonances from band nesting features difficult to see.

The spectra from both the 1L and HBL exfoliated samples corroborate the CVD results. This technique takes advantage of the large excitonic transition dipole to enhance high-energy transitions at the direct-gap momentum point. It can also probe high-energy states with a large JDOS like in the case of the D exciton resonance. I was interested in investigating how photoexcited charge carriers moved into or scattered away from these states and if the SFG output was capable of probing their transient behavior. Those experiments are in the section that follows.

3.2 Transient method: pump-SFG probe spectroscopy

3.2.1 Background: Charge transfer mechanism in TMD HBLs

With the charge transfer (CT) diagram in mind from Chapter 1 (Figure 6), recall that typical CT experiments performed on TMD HBLs have both the pump and probe resonant with the A exciton transitions. Therefore, the experiments are localized at the K point in the BZ. However, in a TMD HBL, the different dielectric environment that both layers experience as well as the interactions between out-of-plane orbitals can shift both the VBM and CBM to other momentum points than the K point in the BZ, according to several computational works.[128–130] The HBL becomes an indirect gap semiconductor. This has a consequence for CT as the charge carriers that are created at the K point scatter over to the new VBM/CBM that is at the lowest-energy configuration and may visit other momentum points along the way. Even if the calculations that posit the VBM/CBM change to other momentum points are incorrect and the K point remains as the VBM/CBM, there will be some momentum scattering from the K point in one layer to the K point in the other layer as TMD HBLs can accommodate a non-zero twist angle between the layers. In other words, there's an inherent momentum mismatch even between the same

momentum points for the constituent layers. [42] Given this situation, it was of great research interest in the mid-to-late 2010s to determine why the CT mechanism was so efficient (<50 fs timescale at room temperature) regardless of the twist angle between the layers. There were two papers that came out in 2020, one experimental and one computational, that provided insight into the CT conundrum and served as the motivation for the pump-probe experiments in the following sections. The paper is:

Direct determination of momentum-resolved electron transfer in the photoexcited van der Waals heterobilayer WS_2/MoS_2, Feng Liu *et al*, **2020**, Physical Review B. (Ref [115])

This study used time-resolved ARPES to create an unambiguous picture of the CT mechanism in a WS_2/MoS_2 HBL. It created charge carriers in both the WS_2 and MoS_2 layers using a 2.2 eV pump and probed the temporal evolution of the charge carriers using ARPES. Because ARPES

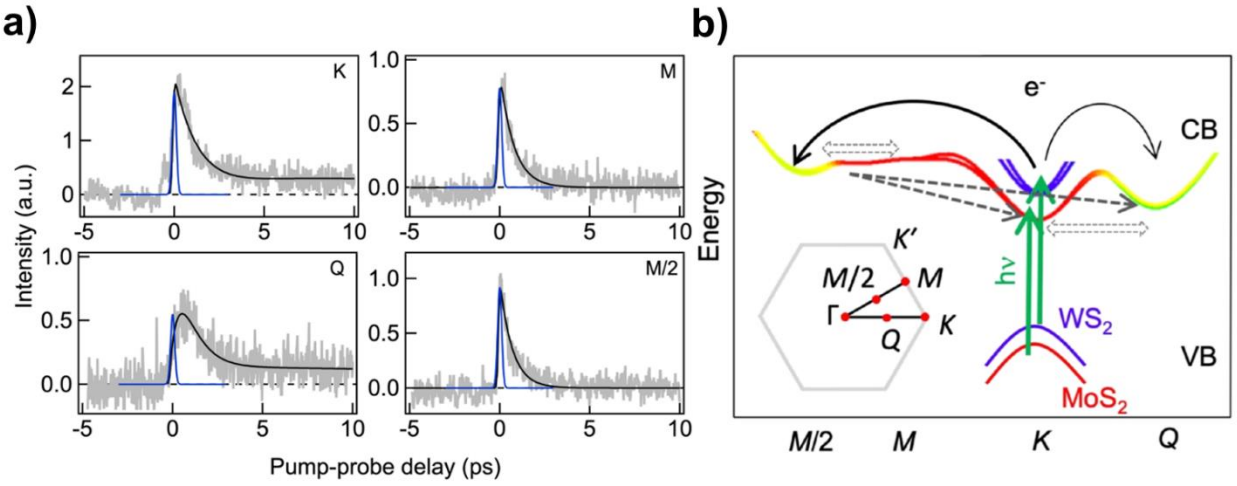

Figure 31 | Results of pump-ARPES probe experiments performed on a WS_2/MoS_2 HBL. a) ARPES transients at various high-symmetry points in the BZ. The figure shows the shapes of the excitation and sample dynamics. b) deduced CT mechanism for WS_2/MoS_2 deduced from the transients in panel a). Figure adapted from Ref 115.

directly probes the BZ, the authors were able to park their ARPES probe at various high-symmetry points in the BZ and watch how the ARPES signal changed as a function of pump-probe delay time. These transients are shown in Figure 31a.

Both the K point (Figure 31a, upper left) and the Q point (Figure 31a, lower left) have transients that peak right after the pump arrives and tails that last for a long time (with a time constant ≥ 40 ps), suggesting the electrons residing at these two momentum points in the CB are in dynamic equilibrium. The peak signal at the Q point has a slight delay relative to the peak signal at the K point and is attributed to electrons generated by the pump pulse taking time to transfer to the Q point. The transients for the M and M/2 points (Figure 31a, upper right and lower right, respectively) are characterized by an instantaneous rise time and the ARPES signal completely decaying by ~3 ps after pump arrival. The electron transfer from K→M and K→M/2 is faster than the experimental temporal resolution. The transient ARPES signal dying away completely means that electrons will funnel from the M and M/2 points to the lower-energy K and Q points. Figure 31b is a schematic of the charge transfer mechanism deduced from the pump-ARPES probe data shown in Figure 31a. CT in WS_2/MoS_2 occurs in 4 steps: 1) Electrons are promoted from the VBM to the CBM at the K point in both WS_2 and MoS_2 layers. 2) Electrons scatter over to either the Q, M, or M/2 momentum points. 3) If the excited electrons occupy the M or M/2 points, they will scatter over to the lower-energy K and Q points. 4) The excited electrons in the K and Q points remain in dynamic equilibrium until they radiatively or non-radiatively recombine with holes in the VB. *Efficient CT occurs in TMD HBLs because the momentum mismatch is relaxed by electrons scattering to non-direct-gap states in the BZ.*

The second paper is:

Excitonic Effect Drives Ultrafast Dynamics in van der Waals Heterostructures, Junyi Liu *et al.*, **2020**, ACS Nano Letters. (Ref [131])

The pump-ARPES probe measurements described above were, to my knowledge, the first time-resolved ARPES study on a TMD HBL and therefore solidified my understanding of CT. While the ARPES probe is capable of (and even more suited to) interrogating holes that are transferred

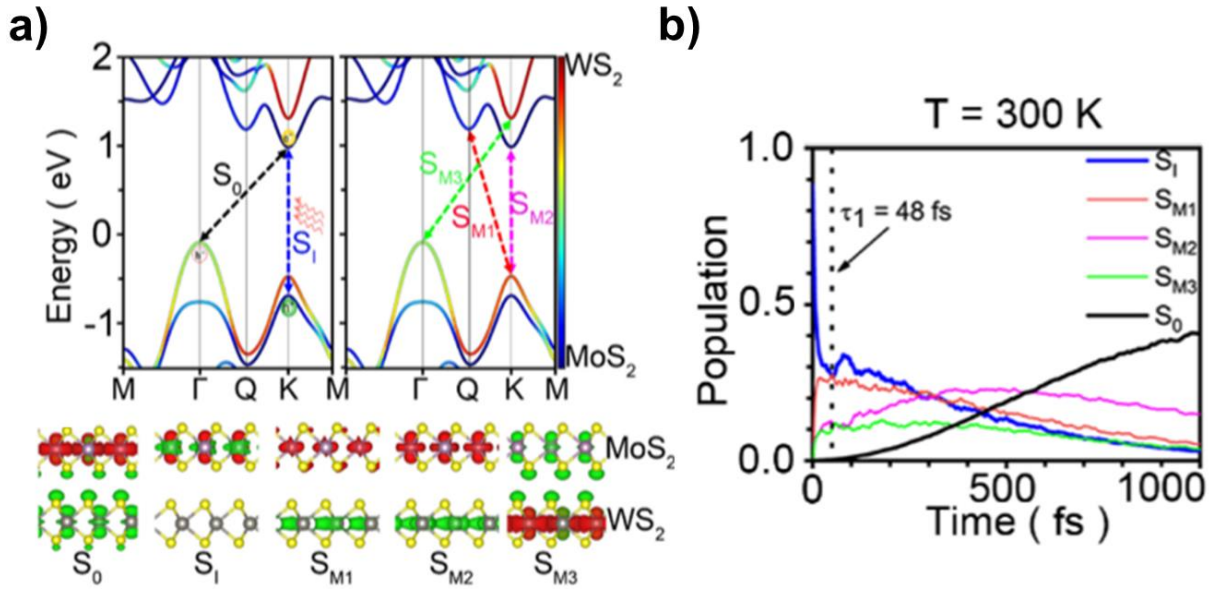

Figure 32 | Figure summary of computational CT mechanism study on a WS_2/MoS_2 HBL. a) Hybridized band structure of the WS_2/MoS_2 with the 5 different exciton species studied. The real-space orbital representations for each exciton are illustrated below the band diagram. b) Population dynamics for each exciton species after excitons are created in the lower-bandgap layer. Figure adapted from Ref 131.

between the layers, the authors did not report any of that data if taken. Those experiments gave insight into the electron transfer mechanism but not the mechanism for holes. The computational work of Liu *et al*. tracked the transferred holes in addition to tracking the whole exciton, rather than just tracking the single particles. They tracked five different exciton species which are illustrated in Figure 32a.

The specific details of all the exciton species are not important. The important observation from Figure 32a is the authors kept track of the initial exciton species S_I, the final (i.e. lowest energy) exciton species S_0, and three intermediate exciton species S_{M1}, S_{M2}, and S_{M3}. *Many of the VBs and CBs that make up these exciton species are not the direct-gap state.* The population dynamics of all the exciton species are shown in Figure 32b which simulates a pump-probe CT experiment. Again, the fine details of the transient behavior are not important. The important observation is that all the excitons studied become populated as charge transfers from the initial state (blue trace) to the final state (black trace), i.e. the red, magenta, and green traces in Figure 32b are non-zero. *The hybridization of bands between the materials indicates that immediately upon charge injection into the lower-energy layer, there is population in the other layer* which is represented in the transients of the three intermediate exciton species. The instantaneous charge transfer phenomenon has been seen in other computational works.[132]

3.2.2 Connecting the background to my transient experiments

The important insights from these two studies are that the direct-gap transitions (CBM and VBM at the K point in both layers) only tell some of the CT mechanism story. Knowing the contribution of non-direct-gap transitions to the CT mechanism, coupled with the SFG work presented in Section 3.1, suggested performing visible pump-SFG probe spectroscopy on the exfoliated WS_2/MoS_2 sample which is presented in the following section. The goal of these experiments is the same as the pump-ARPES probe study - elucidating the CT mechanism by

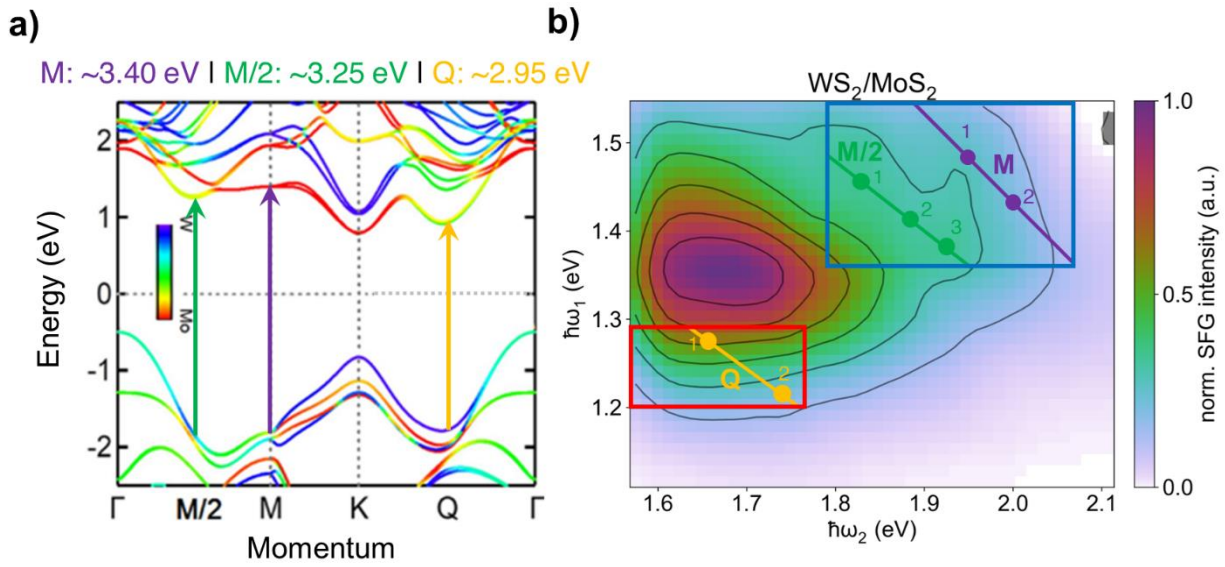

Figure 33 | Blueprint for understanding pump-SFG probe experiments. a) WS_2/MoS_2 hybridized band structure from the literature. The green, purple, and orange arrows represent transitions at the M/2, M, and Q points in the BZ. The energies of these transitions, tabulated above the band structure, are M ~ 3.40 eV, M/2 ~ 3.25 eV, and Q ~ 2.95 eV. b) The unpumped SFG spectrum of exfoliated WS_2/MoS_2 shown previously. Overlayed on the spectrum are two boxes outlined in red and blue and denote the 2D frequency space investigated in the pump-SFG probe experiments shown in Figures 35 and 36. Through each box there are lines of constant output color that correspond to $\hbar\omega_2$ and $\hbar\omega_1$ adding up to the energy of transitions denoted by the arrows in panel a). The numbered dots in the two quadrants correspond to the $\hbar\omega_2$, $\hbar\omega_1$ color combination for the transient delay traces shown in Figures 37 and 38. Band structure adapted from Ref 115.

probing various momentum points in the BZ. My study is novel because it uses the more accessible all-optical probe of the BZ rather than ARPES.

The blueprint for understanding the pump-SFG probe data below is shown in Figure 33. The hybridized band structure adapted from Ref [115] highlights three transitions at momentum points (Figure 33a) involved in the electron transfer mechanism deduced from the pump-ARPES probe measurements described in Section 3.2.1. These transitions are the M/2 point at ~3.25 eV, the M point at ~3.40 eV, and the Q point at ~2.95 eV. Note the hybridized nature of the CB and VB at these transitions indicated by the colorbar in Figure 33a. The unpumped WS_2/MoS_2 SFG spectrum is shown in Figure 33b and is overlayed by two rectangles outlined in red and blue. These quadrants denote the energy range used for the pump-SFG probe experiments. The diagonal lines are lines of constant output color that correspond to the transitions outlined in Figure 33a.

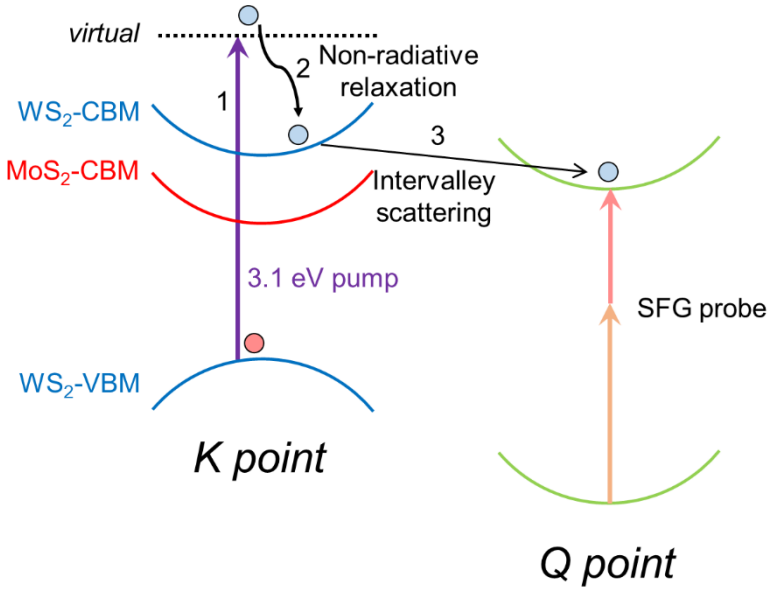

Figure 34 | Potential CT mechanism with the SFG probe tuned to the Q point energy. It mimics the WS_2/MoS_2 band structure shown in Figure 33a. The light blue circle represents an electron and the light red circle represents a hole. Step 1: the pump creates hot electrons at the K point. Step 2: the hot electrons relax non-radiatively to the band edge in the WS_2 layer. Step 3: the electron scatters with a phonon to occupy the Q point CBM. The SFG probe that's tuned to the Q point energy sees less available transitions, resulting in weaker intensity compared to the unpumped SFG intensity. This type of mechanism can be considered for the other momentum points of interest, M/2 and M, but they are not shown for clarity. The pump is 3.10 eV for all pump-SFG probe measurements shown.

The pump-SFG probe experiments have the same experimental setup as the unpumped SFG experiments except for the addition of a 3.10 eV pump pulse. The line of 3.10 eV constant output color runs anti-diagonally through the center of the 2D SFG spectrum. Due to pump scatter, the monochromator passed considerable pump photons to the detector for pixels where the monochromator collected anywhere in the range of $\hbar\omega_2 + \hbar\omega_1 = 3.10$ eV +/- 0.1 eV. This is the reason only the energy ranges indicated by the red and blue quadrants were investigated for the pump-SFG probe experiments.

Here is the thought process for performing these novel pump-probe experiments: the 3.10 eV pump will create hot carriers mostly at the K point as well as at other momentum points in the BZ. The excited electrons (holes) will funnel down (up) in energy to reach the CBM of WS_2 (VBM of MoS_2) at the K point – carriers are now populated at states similar to the ones populated in the Liu *et al.* (experimental work, PRB) and Liu *et al.* (computational work, Nano Letters). Based on these previous works, the carriers will pass through the M and M/2 points and end up at the K and Q points. A schematic of the proposed charge carrier movement in the pump-SFG probe experiments is shown in Figure 34. It is an example of when the SFG pulse sequence probes the Q point, but similar mechanisms would also occur at the M/2 and M points. The 3.10 eV pump (purple arrow) creates hot electrons at the K point (Step 1). The hot electrons relax non-radiatively to the WS_2 layer band edge (Step 2). The electron then scatters with a phonon to occupy the CBM at the Q point (Step 3). Sometime later, the SFG probe that's tuned to the Q point energy interrogates the Q point. Due to the reduced number of transitions available to the SFG probe compared to when the pump is off, the pumped SFG output will be less intense. Thus, the experimental signature in the pumped 2D SFG spectrum that indicates the method works is a bleached feature centered at any of the three energies that the SFG process is probing: 2.95 eV for Q, 3.25 eV for M/2, and 3.40 eV for M.

3.2.3 2D frequency plots at various pump-probe delay times

The pumped SFG spectra for a WS_2/MoS_2 HBL at various pump-probe delay times are shown in Figure 35. The signal metric that is plotted is the difference in pumped and unpumped SFG intensity (ΔSFG) divided by the unpumped SFG intensity. Dividing by the unpumped SFG intensity removes any dependence of the signal on the probe intensity. Furthermore, only a single pump color is used so there can be no pump intensity dependence on ΔSFG. *Thus, these*

measurements are free from intensity variation artifacts, different than the unpumped SFG spectra shown in Section 3.1.

The red and blue quadrants are plotted on the original unpumped SFG plot to show where they fit in with the original experiments. Before the pump arrives, the SFG intensity oscillates about zero indicating a good baseline and no discernible pump scatter (Figure 35, upper left). When the

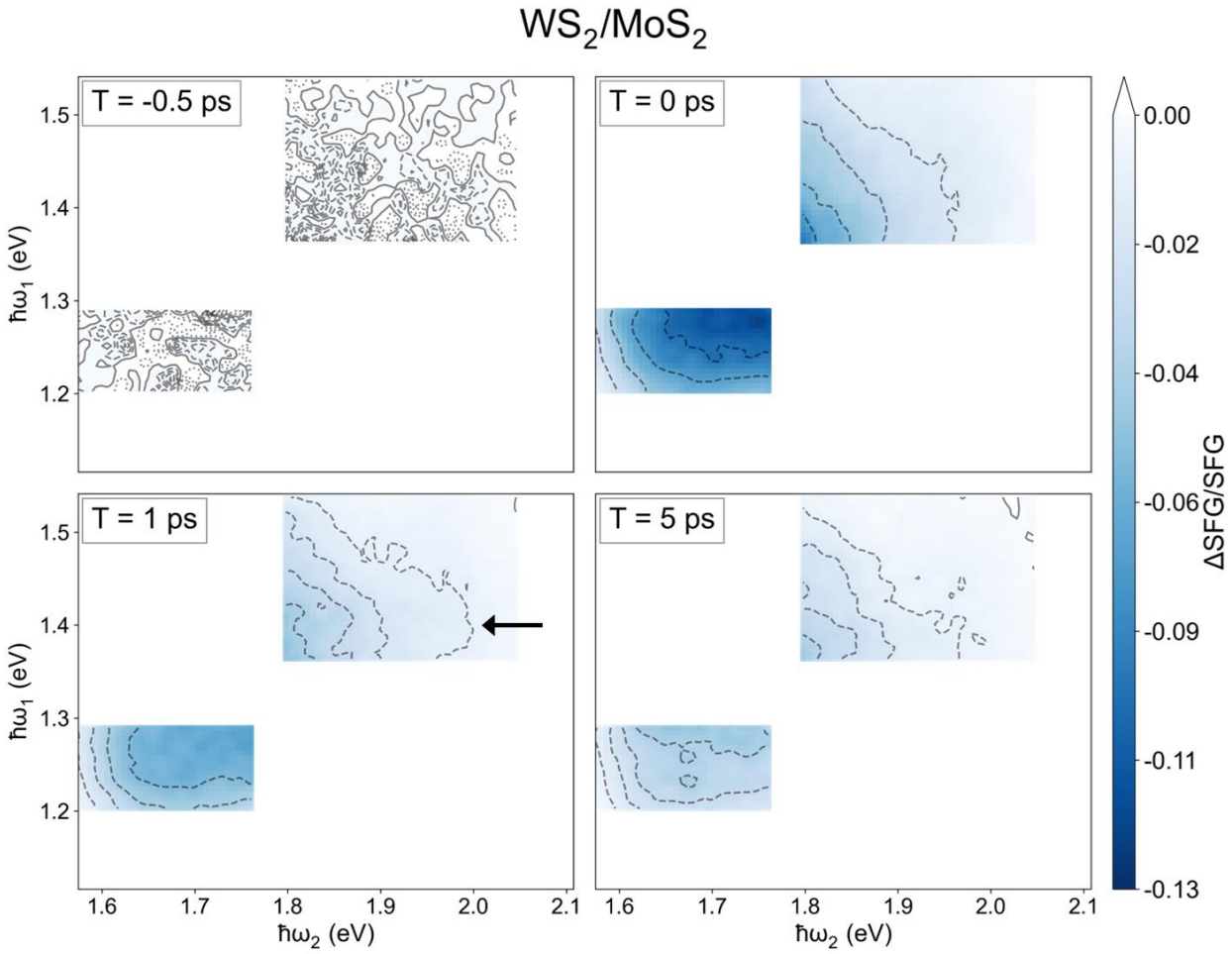

Figure 35 | Pump-SFG probe measurements for the exfoliated WS_2/MoS_2 sample at pump probe delay times of -0.5, 0, 1, and 5 ps. The black arrow in the T=1 (lower left) plot indicates the potential presence of a time-dependent phenomenon where charge is transferring into and then out of the bands associated with the doubly resonant feature contributed by the WS_2 layer (see Figure 30).

pump and probe are overlapped temporally (Figure 35, upper right) bleaches are seen in both the red and blue quadrants with the red quadrant having a maximum bleach of ~13% and the blue quadrant with a maximum bleach of ~8%.

The line shape in the T=0 red quadrant has a rounded rectangular character to it – when compared to the same feature in Figure 30a, it can easily be seen the pumped line shape follows the unpumped line shape. At later delay times of T=1 and T=5 ps (Figure 35, lower left and lower right, respectively) the line shape remains nominally the same with the SFG intensity recovering toward the unpumped intensity at the latest delay time (i.e. the bleach gets weaker). Let's now consider the line shape of the blue quadrant: at T=0, the ΔSFG/SFG signal is negatively sloped with the contours following a constant output color of 3.28 eV. This is near the M/2 point but unfortunately, if my hypothesis was correct for how I wanted these experiments to work out, the line of constant output color needs to be *centered* at or near 3.25 eV. This is clearly not the case as the bleach intensity peaks in the lower left part of the blue quadrant and falls away monotonically to the upper right of the quadrant. It's worth noting that the four contour lines in the T=0 plot all roughly have the same shape. When compared to the T=1 plot, however, this is not the case. The contour line in the blue quadrant that follows the smallest signal value has a "bulge" centered around $\hbar\omega_2$=1.95 eV. Comparing this feature to the unpumped spectrum in Figure 30a, this bulge overlaps well with the doubly resonant feature at the K point in the WS_2 layer. Because the output color of this feature is ~3.32 eV, the 3.10 eV pump likely does not populate the high-lying CB2 band. Rather, the additional bleached signal likely arises from the CBM of WS_2 getting bleached as that is one of the CB states that excited charge carriers will funnel to. Looking at the latest pump-probe delay of T=5 ps, the bulge is mostly gone and the lowest-signal contour matches the shape of the other 3 contours well as in the T=0 ps quadrant.

My hypothesis of seeing bleaches at any of M, M/2, or Q momentum points as a result of charge transferring from WS_2 to MoS_2 and *vice versa* was unfortunately unsuccessful. However, a different experimental signature of charge transferring into and out of the WS_2 CBM at the K point presented itself with the bulge in the blue quadrant in the T=1 plot but not being present at earlier or later delay times.

The same pump-SFG probe measurements were performed on the exfoliated WS_2/WSe_2 HBL as well, albeit with less interesting results than the WS_2/MoS_2 sample. I did not have solid literature

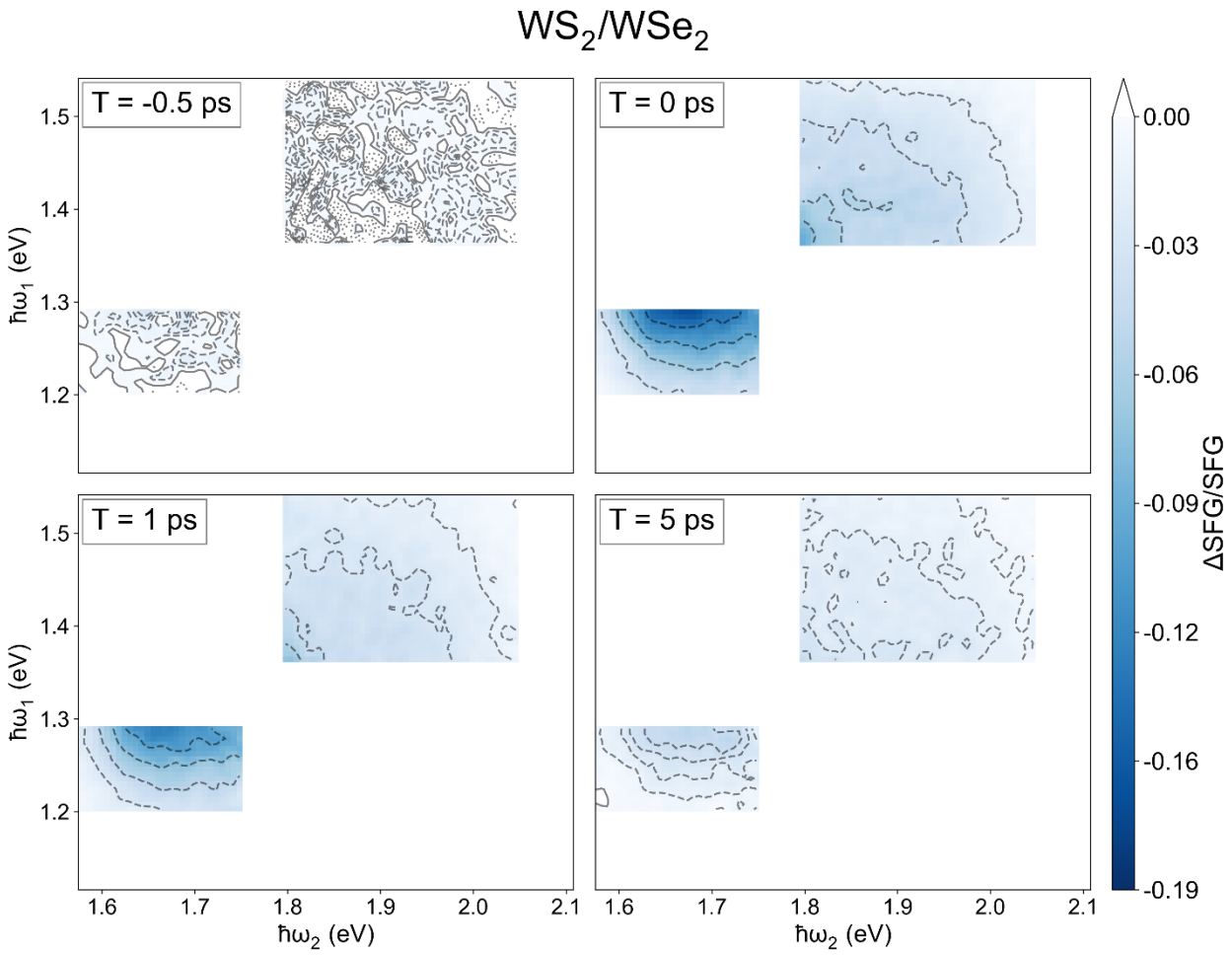

Figure 36 | Pump-SFG probe measurements for the exfoliated WS_2/WSe_2 sample at pump probe delay times of -0.5, 0, 1, and 5 ps.

results to base expectations on for the WS_2/WSe_2 sample so these measurements were mostly done to see if any high-energy diagonal bleaching features were present. The results are shown in Figure 36.

The pumped SFG spectrum before zero delay at T=-0.5 ps (Figure 36, upper left) again demonstrates no pump scatter and a robust baseline. In the T=1 ps plot (upper right) the line shape in the red quadrant follows the same line shape as the same feature in the unpumped spectrum (Figure 30b). This feature, however, does differ from the analogous feature in the pumped WS_2/MoS_2 SFG spectrum in that the WS_2/WSe_2 sample's feature is more circular where the WS_2/MoS_2 sample has more of a rectangular character. This is a result of the WSe_2 A exciton energy being within the scanned $\hbar\omega_2$ range in the red quadrant. The line shape for the red quadrant at the later delay times of T=1, T=5 ps (Figure 36, lower left and lower right, respectively) does not change significantly while the SFG intensity recovers toward the unpumped intensity value. The blue quadrant is the same story as the red quadrant for the WS_2/WSe_2 sample: the pumped line shape follows the unpumped line shape and the pumped SFG intensity recovers toward the unpumped intensity value for later delay times.

3.2.4 Decay transients at specific $\hbar\omega_2$, $\hbar\omega_1$ combinations

To investigate the long-time dynamics of the transient SFG response, $\hbar\omega_2$ and $\hbar\omega_1$ were parked at the various frequency combinations indicated in Figure 33b and the pump-probe delay was finely scanned out to 20 ps. Because the two literature works detailed above covered a WS_2/MoS_2 sample, I decided to focus these efforts on my exfoliated WS_2/MoS_2 sample. The high-resolution transients for the WS_2/MoS_2 red quadrant are shown in Figure 37. The orange traces have an

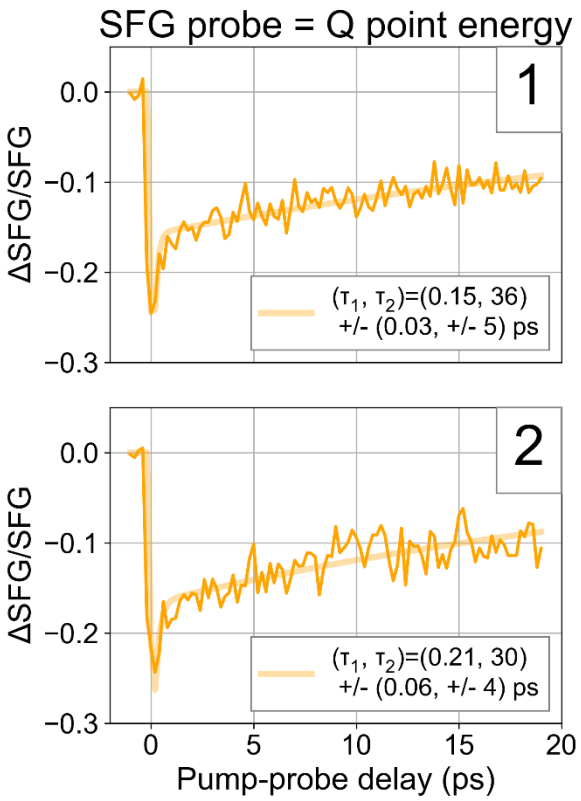

Figure 37 | Pump-SFG probe transients for various $\hbar\omega_2$, $\hbar\omega_1$ combinations in the red quadrant for the WS_2/MoS_2 sample. Both traces have an output color equal to the lowest-energy transition at the Q point and the numbers in the upper right-hand corner of each plot correspond to the numbers indicated in Figure 33b.

SFG output energy equal to the lowest-energy Q point transition (Figure 33a). By taking these high-resolution delay traces, I was looking for a delayed onset in the transient SFG signal akin to the delayed onset of the ARPES transient in Figure 31a (lower left plot).

Both of the $\hbar\omega_2$, $\hbar\omega_1$ combinations in Figure 37 have biexponential behavior and thus were fit with a biexponential. The fast time constant is typically attributed to carrier-carrier annihilation due to a high carrier density [25,133] and the slow time constant is attributed to the electron and hole recombination, either radiatively or non-radiatively. Both Q point transients have fast time constants in the 150-200 fs range and slower time constants in the 30-35 ps range. There was not a delayed response right after pump-probe overlap that indicated carriers funneling into the Q point, which is what Liu *et al.* saw with their ARPES probe (Figure 31a).

The transients for the blue quadrant are shown in Figure 38 along with their exponential decay fits. Again, the number label in the bottom right of each plot of Figure 38 corresponds to the $\hbar\omega_2$, $\hbar\omega_1$ combination indicated in Figure 33b. Other than the 2nd M point, these transients showed two dynamics regimes with a fast and slow component. Let's first consider the M/2 point transients (Figure 38, left column). The fast time constant for all three M/2 points is ~120 fs. The slow time constant is similar for the 1st and 2nd points at 40 ps but is faster for the 3rd point with a

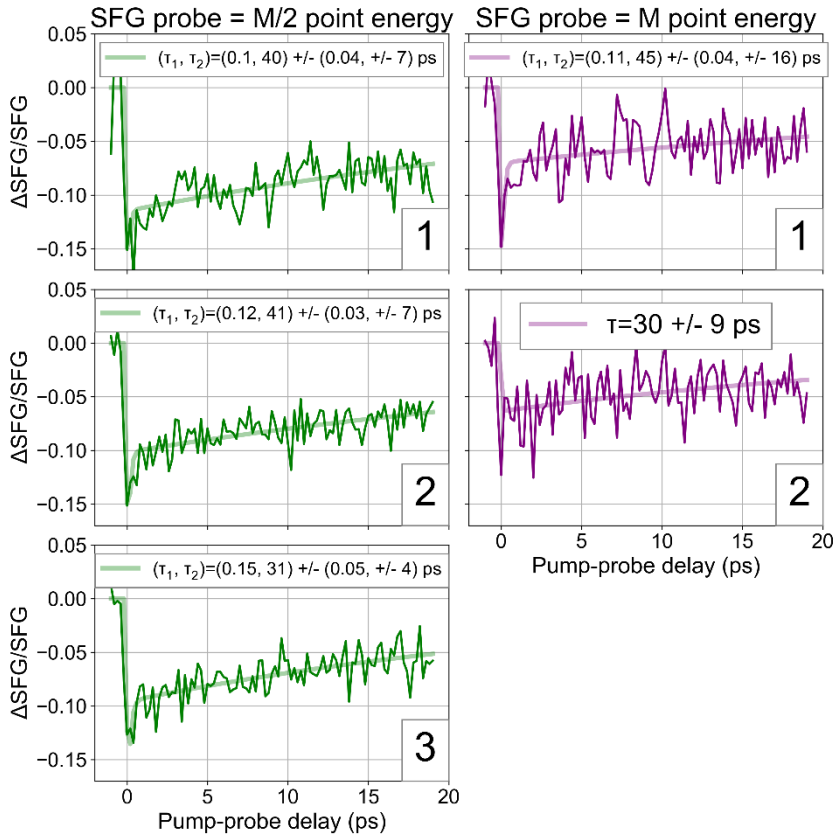

Figure 38 | Pump-SFG probe transients for various $\hbar\omega_2$, $\hbar\omega_1$ combinations in the red quadrant for the WS_2/MoS_2 sample. The left (right) column with the green (purple) traces has an output color equal to the lowest-energy transition at the M/2 (M) point and the numbers in the lower right-hand corner of each plot correspond to the numbers indicated in Figure 33b. All the transients are fit with biexponential decays except for the 2nd M point.

time constant of ~30 ps. It should be noted that the $\hbar\omega_2$, $\hbar\omega_1$ combination of the 3rd transient overlaps with the "bulge" feature that was discussed in Figure 35 (T=1 ps) which is the doubly resonant feature that originates from the WS_2 CBM at the K point.

The long-time transient behavior of the 3rd M/2 point compared to the 1st and 2nd support the findings of the 2D frequency plots in Figure 35, namely both representations of the data suggest electrons are funneled out of the WS_2 CBM either to the MoS_2 CBM or the Q point that is hybridized between the two layers (see HBL band structure, Figure 33a). The 1st M point transient (Figure 38, top right) has similar dynamics to the 1st and 2nd M/2 point transients. The 2nd M point transient was better fit with a monoexponential decay and has a time constant of ~30 ps. There's a large relative error associated with this value, however. Because the other 6 transients showed the same behavior, the 2nd M point transient was not considered when deducing the general dynamics behavior seen by the SFG probe.

In conclusion, the pump-SFG probe technique did not report the same dynamics in the WS_2/MoS_2 HBL as were reported by Liu *et al* using their pump-ARPES probe technique. There were no ΔSFG/SFG peaks centered around the Q, M/2, or M points as I had envisioned and most transients at these momentum points showed the same dynamics. The pump-SFG probe data instead points to essentially the entire BZ getting bleached which can be understood in the following way: the SFG probe ranges in output color from 2.7-3.6 eV which contains many transitions in the BZ. The 3.10 eV pump creates carriers at many points in the BZ. Upon excitation, the hot carriers scatter to a myriad of states at a rate faster than the experiment can resolve temporally. This is proven by the instantaneous differential SFG signal seen in the Q, M/2 and M point transients. We know the hot carriers populate many states from the experimental work by Liu *et al.* and the computation work by Liu *et al.* that's outlined in Section

3.2.1. The carriers occupy these lowest-energy states and relax radiatively or non-radiatively with a time constant of 35-40 ps. While the SFG probe is selective for the K point, it's not selective enough to probe the other momentum points of interest. Instead, using a third-order spectroscopy that couples four bands together will provide the selectivity required to probe specific points in the BZ. Furthermore, performing similar measurements at lowered temperatures will slow down the carrier scattering mechanisms and will allow for differences in dynamics to be resolved.

It's worth noting again that the 3rd M/2 point transient that overlaps with the HX state originating from the WS_2 layer in the WS_2/MoS_2 HBL SFG spectrum (Figure 30a) has the fastest decay of all the transients investigated. This suggests there are interesting dynamics occurring at the HX state. Unfortunately, the SFG probe cannot resolve whether the interesting dynamics are occurring at the A exciton state or the HX state. Future experiments to resolve such dynamics are presented in Chapter 4.3.

4 Future Work

The final chapter in this dissertation presents the work I believe to be the most important for carrying on the projects discussed in Chapters 2 and 3. Section 4.1 is a discussion on how to implement higher acquisition rates using the nonlinear microscope. The nonlinear microscope currently excels at performing nonlinear spectroscopies, but implementing a higher frame rate will allow it to perform more conventional TAM experiments that use linear probes. Section 4.2 proposes two experiments to confirm the assignment of the HX state seen in the 2D SFG measurements from Chapter 2.2. These experiments are prudent for confirming the validity of sum-frequency spectroscopies (SFG, TSF) as a technique to characterize high-energy CB/VB states in 2D semiconductors. Section 4.3 concludes the Chapter by suggesting a few small tweaks to the pump-SFG probe experiments discussed in Chapter 3.3 to gain a direct probe the HX state's dynamics.

4.1 Implementation of shot-to-shot acquisition rates for widefield TAM using a linear probe

In pump-SHG probe experiments like the ones discussed in Chapter 2.3, or pump-THG probe experiments like those published previously in the Wright group,[134] the peak differential signals upon resonant pumping in TMDs range from 10-50%. This signal level is more than an order of magnitude greater than differential signals in traditional pump-linear probe measurements which typically peak at a few percent. Because the differential signals are smaller in standard, linear pump-probe measurements, the pump pulse is chopped with as high a frequency as possible to

compare probe pulses that are nearby in the optical train and are therefore well-correlated.[76,135] For example, the fs system's standard pump-probe setup chops the pump at 500 Hz which is every other laser shot given the fs system's 1 kHz repetition rate. In this way, neighboring probe pulses in the optical train are compared to one another which have a higher correlation and reduces noise.

In the Wright Group widefield nonlinear microscope's current state, a mechanical shutter chops the pump pulse once for every scanned motor position (i.e. there is a "pump-on" and "pump-off" measurement taken at each motor position before progressing to the next motor position). The chopping repetition rate in this setup is defined by the camera acquisition time. For example, in the pump-SHG probe measurements in Chapter 2, the collection of an SHG image took 30 s, meaning the probe pulses used to generate the SHG images alternate every 30 000 shots. The average intensity of the probe pulses used to generate successive pump-on and pump-off images was likely different. However, the large ΔSHG/SHG values in those experiments cover any potential problems introduced by laser intensity fluctuations. This would be problematic for pump-linear probe measurements where the differential signals are smaller. If we consider the same chopping scheme using a linear probe where the intensities are much larger, and, for example, 1 s acquisitions are needed to fill the pixel wells, that means the probe pulses used to generate the linear image still alternate every 1000 shots. This is a drastic decrease in performance compared to the standard fs system pump-probe setup of collection where every other probe pulse is compared.

Indeed, nonlinear probes can retrieve the same dynamics information as linear probes.[6] Due to the lower-intensity probe field, however, pump-nonlinear probe measurements may take needlessly long to perform compared to a linear probe. Sometimes the simpler measurement is

all that is needed and it's convenient to have the option to choose between the two. This motivates implementing a shot-to-shot readout and signal processing scheme for the Wright Group's nonlinear microscope.

As mentioned in Chapter 2.2.4, reading out a smaller section of the camera's pixels (called region of interest, or ROI) and binning the pixels speed up the acquisition rate. The ProEM512 EMCCD camera employed in the Wright Group's nonlinear microscope achieves a frame rate of 1 kHz with a ROI of just less than 100 x 100 pixels. With the 16 μm square pixels and the 20X microscope magnification, this corresponds to an area of ~80 μm x 80 μm that can be imaged at the fs system repetition rate. If spatial resolution is not important and the pixels can be binned, the total area that can be imaged at 1 kHz increases to 120 μm x 120 μm for 2 x 2 binning and 200 μm x 200 μm for 4 x 4 binning. These are imaging areas that would easily house microstructures studied by the materials side of the Wright Group.

Changing the ROI and binning settings on the EMCCD is trivial. The Wright Group has optical choppers that can chop at half of the fs system repetition rate. The main challenge is in telling the data acquisition software which camera images are "pump off" and which are "pump on." In standard pump-probe measurements on the fs system, the probe and chopper signals are read out on the same data acquisition board (DAQ) and the math required to calculate the transient signal is performed by custom Python scripts. No manual calculations are necessary - all the required math is performed "under the hood."

What needs to happen is the daemon that controls the camera must call the daemon that controls the DAQ that holds all the chopper phases. Once the camera daemon has an array of the chopper phases for every shot, each camera image can be tagged with the corresponding chopper phase and the differential signal can be calculated. In Appendix C, Section 8.4 I provide an example

scenario with real numbers so future implementation may be less nebulous and more straightforward. That workflow is an important reference for Wright Group students who wish to perform pump-linear probe measurements with the widefield nonlinear microscope in the future.

4.2 Proposed experiments to further corroborate HX peak assignment from 2D SFG studies

The current assignment for the double resonance peak in the 2D SFG spectra shown in Chapter 3 is from a high-lying CB state that is two bands above the CBM at the K point. There are three factors that put a high degree of confidence into this assignment: 1) similar double resonance

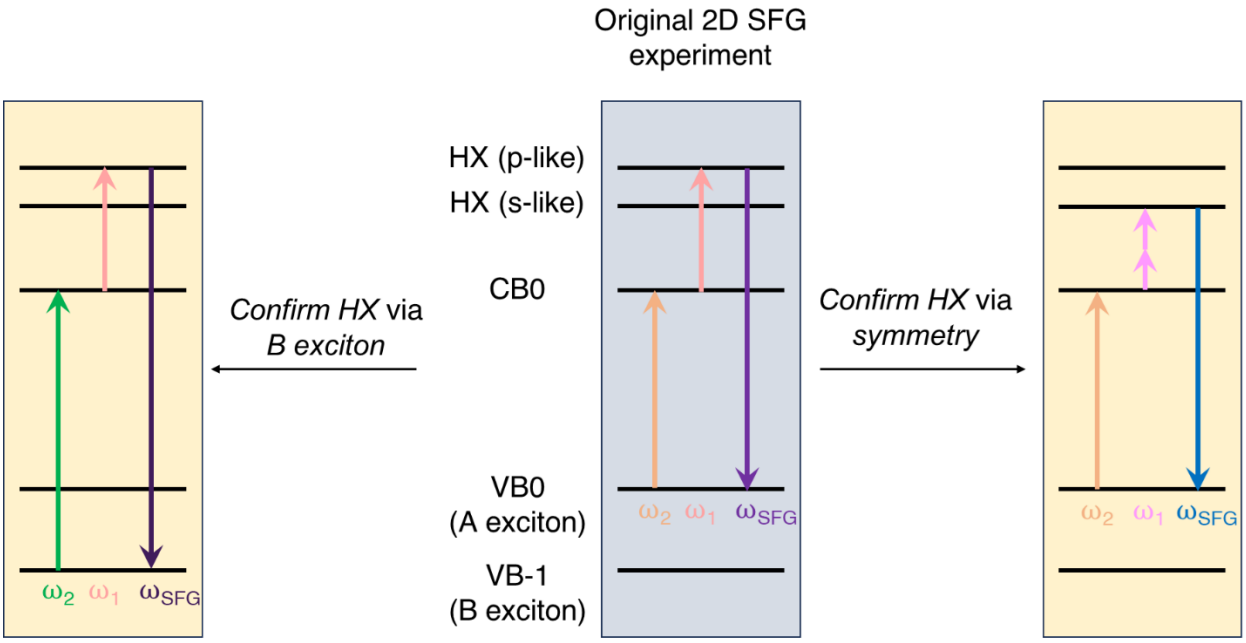

Figure 39 | WMELs for proposed experiments to confirm HX state assignment in 1L TMDs. Note the additional HX (s-like) state and VB-1 (B exciton) state relative to original WMELs shown in Chapter 3. The middle WMEL (grey background) corresponds to the prominent pathway of the original 2D SFG experiments present in Chapter 2. The SFG output emits from the HX state with p-like symmetry. The WMEL on the right (yellow background) would confirm the HX state assignment by using a $\chi^{(3)}$ process to observe TSF output from the nearby s-like HX state. The WMEL on the left (yellow background) would confirm the HX assignment by exciting the B exciton instead of the A exciton. Since they both originate from the K point, there should be a double resonance feature when ω_2 is equal to the B exciton energy (~2.40 eV in 1L WS_2).

features were seen at the MoS_2 A exciton energy and WSe_2 A exciton energy in WS_2/MoS_2 and WS_2/WSe_2 HBL samples, respectively (see Chapter 3.1.2). 2) Simple steady state equations with assumptions that match the experimental conditions have qualitative agreement with experimental line shapes. 3) The state has been observed in two other 1L TMDs, namely WSe_2 and $MoSe_2$.[96,126] While the 1st factor is promising, the SFG measurements performed on HBL samples have twice the available resonances compared to 1Ls which complicates the 2D SFG spectra interpretation. The 3rd factor is also promising because the electronic structure for the four popular semiconducting TMDs are qualitatively the same. However, there are differences between TMDs, such as SOC, that make the electronic structure and optical transitions quantitatively different. To unambiguously confirm the assignment of the HX state in 1L WS_2, additional experiments need to be performed on 1L WS_2 that lock-in the HX energy and location at the K point. The WMEL diagrams for two supporting experiments are shown in Figure 39.

The middle WMEL (grey background) outlines the primary pathway in the original 2D SFG experiments discussed in Chapter 3. Note there are two HX states with symmetry assignments of s-like or p-like.[96] Because the A exciton (VB0→CB0) is s-like, symmetry selection rules prohibit promotion of the electron at CB0 to the s-like HX state. This means that the HX state that emits the SFG output field in the original measurements is from the p-like HX state. The p-like HX state is slightly higher in energy than the s-like HX state.[96] In order to access the s-like HX state, the nonlinear process needs to be odd-ordered. I propose to use TSF to access the s-like HX state in 1L WS_2. The WMEL for such a pathway is shown on the right in Figure 39 (yellow background). By simply using two interactions at half the energy of $\hbar\omega_1$ in substitution for one interaction at the original $\hbar\omega_1$ energy, the transition from A→ HX will be symmetry allowed.

Observing TSF output at a lower energy than the SFG output will confirm the assignment of the HX state.

Another way to confirm the HX state assignment is to change the energy of $\hbar\omega_2$ to be resonant with the *B exciton* rather than the A exciton (Figure 39 left WMEL, yellow background). The energy of $\hbar\omega_1$ is unchanged. The B exciton energy in 1L WS_2 is at ~2.40 eV. Since the A and B excitons both originate from the K point, observing a double resonance feature at ($\hbar\omega_2$, $\hbar\omega_1$) = (~2.40, 1.35) eV will confirm two things: 1) the HX state is indeed at the K point, and 2) the HX state is ~1.35 eV above the CBM, as posited by the original 2D SFG experiments. This method is more straightforward than the aforementioned symmetry method since the energy difference between the A and B excitons in 1L WS_2 is well known compared to the energy difference between the s-like and p-like HX states.

4.3 Pump-push-probe spectroscopy for directly probing HX dynamics

The SFG measurements presented in Chapter 3 demonstrated a selective way to probe a high-lying conduction band state in TMDs that occurs ~1.35 eV above the conduction band minimum (the HX state). HX may influence the carrier occupation of the A exciton state as they are close to one another in the BZ and even share the same valence band. For example, knowing how the HX state feeds the band edge state when a TMD/perovskite absorbs a high-energy photon from the sun is important for solar cell applications. The pump-SFG probe setup presented in Chapter

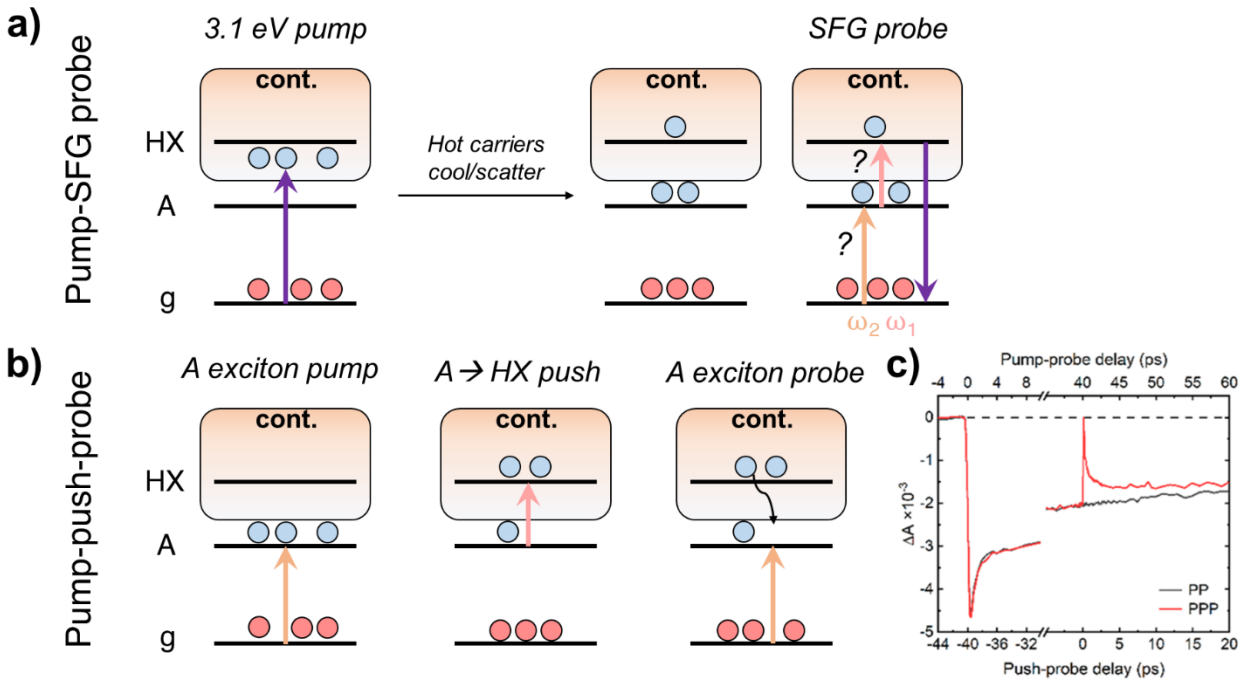

Figure 40 | Comparison of pump-SFG probe experiments from Chapter 3.3 to proposed pump-push-probe spectroscopy for interrogating HX state dynamics. a) The 3.1 eV pump populates hot carriers at the K point as well as throughout the Brillouin zone. Hot carriers at the K point cool to the band edge. Electrons at the Γ point scatter over to the K point at HX and A states through phonon emission/absorption. The SFG probe bleach is obfuscated by electron population at both SFG transitions b) an A exciton pump creates band-edge excitons. A NIR push pulse, equal to the A→HX transition energy, promotes A exciton electrons to the HX state. An A exciton probe measures the relaxation of HX electrons back to the A exciton. c) An example delay trace for pump-push-probe spectroscopy. The negative spike on the LHS of the plot corresponds to the pump-probe signal and the positive spike on the RHS of the plot corresponds to the push-probe signal. Panel c) adapted from Ref 136.

3.2 was not conducive to measuring HX dynamics and Figure 40a explains the reason by presenting a series of WMELs that describes charge carrier occupation created by the 3.1-eV pump and seen by the SFG probe. The 3.1-eV pump creates hot carriers at the K point as well as many other points in the BZ. The hot carriers cool to the band edge and occupy the A exciton state. Charge carriers at other momentum points can absorb/emit a phonon to scatter to the HX state at the K point. The occupation of the HX state induced by the pump is much less than the occupation at the A exciton state, although it is non-zero. The SFG probe interacts with the sample and has bleaches from both transitions: $\hbar\omega_2$ has a bleached g→A transition due to cooled hot carriers from the pump, and $\hbar\omega_1$ has a bleached A→HX transition due to scattered electrons that originate from other momentum points in the BZ. As the bleached SFG signal goes from its maximum value back to baseline (i.e. carriers are relaxing), it's not possible to know the contributions of the two transitions to the overall bleach. In fact, most of the SFG bleach signal is likely coming from the A exciton transition as that state has a higher occupation of carriers. There is only one readout (the overall SFG bleach) from two signal contributions (both resonant transitions) meaning there's no reliable way to extract the dynamics from only the HX state.

Using a technique called pump-push-probe spectroscopy can unambiguously probe the HX state dynamics. The technique is similar to pump-probe spectroscopy except for an additional "push" pulse that further excites pump-induced charge carriers. Figure 40b presents a series of WMELs that shows charge carrier occupation created by the pump and push pulses and seen by the probe pulse. A pump pulse resonant with the A exciton creates excitons at the band-edge. Sometime after the excitons thermalize (i.e. after the processes from the fast relaxation component finish), a push pulse resonant with the A→HX transition promotes band-edge electrons to the HX state.

Finally, a probe pulse resonant with the A exciton monitors the relaxation of the HX-state electrons back down to the band edge.

An example delay trace for what this pump-push-probe spectroscopy experiment would look like is presented in Figure 40c.[136] The negative peak on the LHS of Figure 40c is the differential signal at the A exciton energy due to the pump. *This trace is crucial because it acts as a baseline signal for the bleach magnitude only from the pump.* The positive peak in the red trace on the RHS of Figure 40c is the differential signal at the A exciton energy due to the push pulse. A positive spike is seen because the push pulse promotes electrons from A→HX and opens occupation in the A exciton state. The dynamics of this red trace in Figure 40c is the HX dynamics as carriers relax back to the band edge. HX-state electrons may relax back to non-band-edge CBs at the K point or CBs at different momentum points. Comparing the long-time differential signal value of the pump-push-probe experiment to the control experiment with no push pulse (black trace, PP) will give insight to how many HX-state electrons relax to the band edge and how many relax to other places in the BZ.

5 References

(1) Mathew, N. A.; Yurs, L. A.; Block, S. B.; Pakoulev, A. V; Kornau, K. M.; Iii, E. L. S.; Wright, J. C. Fully and Partially Coherent Pathways in Multiply Enhanced Odd-Order Wave-Mixing Spectroscopy. *Journal of Physical Chemistry A* **2010**, *114*, 817–832.

(2) Mathew, N. A.; Yurs, L. A.; Block, S. B.; Pakoulev, A. V.; Kornau, K. M.; Wright, J. C. Multiple Quantum Coherence Spectroscopy. *Journal of Physical Chemistry A* **2009**, *113* (33), 9261–9265. https://doi.org/10.1021/jp903337s.

(3) Mathew, N. A.; Block, S. B.; Yurs, L. A.; Kornau, K. M.; Pakoulev, A. V.; Wright, J. C. Multiply Enhanced Odd-Order Wave-Mixing Spectroscopy. *Journal of Physical Chemistry A* **2009**, *113* (48), 13562–13569. https://doi.org/10.1021/jp905796y.

(4) Handali, J. D.; Sunden, K. F.; Thompson, B. J.; Neff-Mallon, N. A.; Kaufman, E. M.; Brunold, T. C.; Wright, J. C. Three Dimensional Triply Resonant Sum Frequency Spectroscopy Revealing Vibronic Coupling in Cobalamins: Toward a Probe of Reaction Coordinates. *Journal of Physical Chemistry A* **2018**, *122* (46), 9031–9042. https://doi.org/10.1021/acs.jpca.8b07678.

(5) Morrow, D. J.; Kohler, D. D.; Czech, K. J.; Wright, J. C. Communication: Multidimensional Triple Sum-Frequency Spectroscopy of MoS2 and Comparisons with Absorption and Second Harmonic Generation Spectroscopies. *Journal of Chemical Physics* **2018**, *149* (9). https://doi.org/10.1063/1.5047802.

(6) Morrow, D. J.; Kohler, D. D.; Zhao, Y.; Jin, S.; Wright, J. C. Triple Sum Frequency Pump-Probe Spectroscopy of Transition Metal Dichalcogenides. *Phys Rev B* **2019**, *100* (23), 1–16. https://doi.org/10.1103/PhysRevB.100.235303.

(7) Block, S. B.; Yurs, L. A.; Pakoulev, A. V.; Selinsky, R. S.; Jin, S.; Wright, J. C. Multiresonant Multidimensional Spectroscopy of Surface-Trapped Excitons in PbSe Quantum Dots. *Journal of Physical Chemistry Letters* **2012**, *3* (18), 2707–2712. https://doi.org/10.1021/jz300599b.

(8) Yurs, L. A.; Block, S. B.; Pakoulev, A. V.; Selinsky, R. S.; Jin, S.; Wright, J. Multiresonant Coherent Multidimensional Electronic Spectroscopy of Colloidal PbSe Quantum Dots. *Journal of Physical Chemistry C* **2011**, *115* (46), 22833–22844. https://doi.org/10.1021/jp207273x.

(9) Kohler, D. D.; Thompson, B. J.; Wright, J. C. Resonant Third-Order Susceptibility of PbSe Quantum Dots Determined by Standard Dilution and Transient Grating Spectroscopy. *Journal of Physical Chemistry C* **2018**, *122* (31), 18086–18093. https://doi.org/10.1021/acs.jpcc.8b04462.

(10) Czech, K. J.; Thompson, B. J.; Kain, S.; Ding, Q.; Shearer, M. J.; Hamers, R. J.; Jin, S.; Wright, J. C. Measurement of Ultrafast Excitonic Dynamics of Few-Layer MoS2 Using

State-Selective Coherent Multidimensional Spectroscopy. *ACS Nano* **2015**, *9* (12), 12146–12157. https://doi.org/10.1021/acsnano.5b05198.

(11) Morrow, D. J.; Kohler, D. D.; Wright, J. C. Group- and Phase-Velocity-Mismatch Fringes in Triple Sum-Frequency Spectroscopy. *Phys Rev A (Coll Park)* **2017**, *96* (6), 1–9. https://doi.org/10.1103/PhysRevA.96.063835.

(12) Morrow, D. J.; Kohler, D. D.; Zhao, Y.; Scheeler, J. M.; Jin, S.; Wright, J. C. Quantum Interference between the Optical Stark Effect and Resonant Harmonic Generation in WS2. *Phys Rev B* **2020**, *102* (16). https://doi.org/10.1103/PhysRevB.102.161401.

(13) Ávalos-Ovando, O.; Mastrogiuseppe, D.; Ulloa, S. E. Lateral Heterostructures and One-Dimensional Interfaces in 2D Transition Metal Dichalcogenides. *Journal of Physics Condensed Matter* **2019**, *31* (21). https://doi.org/10.1088/1361-648X/ab0970.

(14) Jin, C.; Ma, E. Y.; Karni, O.; Regan, E. C.; Wang, F.; Heinz, T. F. Ultrafast Dynamics in van Der Waals Heterostructures. *Nat Nanotechnol* **2018**, *13* (11), 994–1003. https://doi.org/10.1038/s41565-018-0298-5.

(15) Sie, E. J. Coherent Light-Matter Interactions in Monolayer TMDs, Massachusetts Institute of Technology, 2017. https://doi.org/10.1134/S1063783414100321.

(16) Hsu, W. T.; Zhao, Z. A.; Li, L. J.; Chen, C. H.; Chiu, M. H.; Chang, P. S.; Chou, Y. C.; Chang, W. H. Second Harmonic Generation from Artificially Stacked Transition Metal Dichalcogenide Twisted Bilayers. *ACS Nano* **2014**, *8* (3), 2951–2958. https://doi.org/10.1021/nn500228r.

(17) Novoselov, K. S.; Geim, A. K.; Morozov, S. V.; Jiang, D.; Zhang, Y.; Dubonos, S. V.; Grigorieva, I. V.; Firsov, A. A. Electric Field Effect in Atomically Thin Carbon Films. *Science (1979)* **2004**, *306*, 666–669.

(18) Liu, F.; Wu, W.; Bai, Y.; Chae, S. H.; Li, Q.; Wang, J.; Hone, J.; Zhu, X.-Y. Disassembling 2D van Der Waals Crystals into Macroscopic Monolayers and Reassembling into Artificial Lattices. *Science (1979)* **2020**, *367* (6480), 903–906. https://doi.org/10.1126/science.aba1416.

(19) Dong, J.; Zhang, L.; Ding, F. Kinetics of Graphene and 2D Materials Growth. **2019**, *1801583*, 1–29. https://doi.org/10.1002/adma.201801583.

(20) Chernikov, A.; Berkelbach, T. C.; Hill, H. M.; Rigosi, A.; Li, Y.; Aslan, O. B.; Reichman, D. R.; Hybertsen, M. S.; Heinz, T. F. Exciton Binding Energy and Nonhydrogenic Rydberg Series in Monolayer WS2. *Phys Rev Lett* **2014**, *113* (7). https://doi.org/10.1103/PhysRevLett.113.076802.

(21) Qiu, D. Y.; Da Jornada, F. H.; Louie, S. G. Optical Spectrum of MoS2: Many-Body Effects and Diversity of Exciton States. *Phys Rev Lett* **2013**, *111* (21). https://doi.org/10.1103/PhysRevLett.111.216805.

(22) Liu, G. Bin; Xiao, D.; Yao, Y.; Xu, X.; Yao, W. Electronic Structures and Theoretical Modelling of Two-Dimensional Group-VIB Transition Metal Dichalcogenides. *Chem Soc Rev* **2015**, *44* (9), 2643–2663. https://doi.org/10.1039/c4cs00301b.

(23) Goswami, T.; Bhatt, H.; Babu, K. J.; Kaur, G.; Ghorai, N.; Ghosh, H. N. Ultrafast Insights into High Energy (C and D) Excitons in Few Layer WS2. *Journal of Physical Chemistry Letters* **2021**, *12* (28), 6526–6534. https://doi.org/10.1021/acs.jpclett.1c01627.

(24) Kormányos, A.; Burkard, G.; Gmitra, M.; Fabian, J.; Zólyomi, V.; Drummond, N. D.; Fal, V. K · p Theory for Two-Dimensional Transition Metal Dichalcogenide Semiconductors. *2d Mater* **2015**, *2*, 022001.

(25) Kumar, N.; Cui, Q.; Ceballos, F.; He, D.; Wang, Y.; Zhao, H. Exciton-Exciton Annihilation in MoSe2 Monolayers. *Phys Rev B Condens Matter Mater Phys* **2014**, *89* (12). https://doi.org/10.1103/PhysRevB.89.125427.

(26) You, Y.; Zhang, X. X.; Berkelbach, T. C.; Hybertsen, M. S.; Reichman, D. R.; Heinz, T. F. Observation of Biexcitons in Monolayer WSe2. *Nat Phys* **2015**, *11* (6), 477–481. https://doi.org/10.1038/nphys3324.

(27) Sie, E. J.; Lui, C. H.; Lee, Y. H.; Kong, J.; Gedik, N. Observation of Intervalley Biexcitonic Optical Stark Effect in Monolayer WS2. *Nano Lett* **2016**, *16* (12), 7421–7426. https://doi.org/10.1021/acs.nanolett.6b02998.

(28) Cui, Q.; Ceballos, F.; Kumar, N.; Zhao, H. Transient Absorption Microscopy of Monolayer and Bulk WSe2. *ACS Nano* **2014**, *8* (3), 2970–2976. https://doi.org/10.1021/nn500277y.

(29) Wang, H.; Strait, J. H.; Zhang, C.; Chan, W.; Manolatou, C.; Tiwari, S.; Rana, F. Fast Exciton Annihilation by Capture of Electrons or Holes by Defects via Auger Scattering in Monolayer Metal Dichalcogenides. *Phys Rev B Condens Matter Mater Phys* **2015**, *91* (16). https://doi.org/10.1103/PhysRevB.91.165411.

(30) Palummo, M.; Bernardi, M.; Grossman, J. C. Exciton Radiative Lifetimes in Two-Dimensional Transition Metal Dichalcogenides. *Nano Lett* **2015**, *15* (5), 2794–2800. https://doi.org/10.1021/nl503799t.

(31) Zhang, X. X.; You, Y.; Zhao, S. Y. F.; Heinz, T. F. Experimental Evidence for Dark Excitons in Monolayer WSe2. *Phys Rev Lett* **2015**, *115* (25), 1–6. https://doi.org/10.1103/PhysRevLett.115.257403.

(32) Sie, E. J.; McLver, J. W.; Lee, Y. H.; Fu, L.; Kong, J.; Gedik, N. Valley-Selective Optical Stark Effect in Monolayer WS2. *Nat Mater* **2015**, *14* (3), 290–294. https://doi.org/10.1038/nmat4156.

(33) Sie, E. J.; Lui, C. H.; Lee, Y.; Fu, L.; Kong, J.; Gedik, N. Large, Valley-Exclusive Bloch-Siegert Shift in Monolayer WS2. *Science (1979)* **2017**, *1069* (March), 1066–1069.

(34) Herrmann, P.; Klimmer, S.; Lettau, T.; Monfared, M.; Staude, I.; Paradisanos, I.; Peschel, U.; Soavi, G. Nonlinear All-Optical Coherent Generation and Read-Out of Valleys in Atomically Thin Semiconductors. *Small* **2023**, *19* (37). https://doi.org/10.1002/smll.202301126.

(35) Ahn, E. C. 2D Materials for Spintronic Devices. *npj 2D Materials and Applications*. Nature Research December 1, 2020. https://doi.org/10.1038/s41699-020-0152-0.

(36) Schaibley, J. R.; Yu, H.; Clark, G.; Rivera, P.; Ross, J. S.; Seyler, K. L.; Yao, W.; Xu, X. Valleytronics in 2D Materials. *Nature Reviews Materials*. Nature Publishing Group August 23, 2016. https://doi.org/10.1038/natrevmats.2016.55.

(37) Pant, A.; Mutlu, Z.; Wickramaratne, D.; Cai, H.; Lake, R. K.; Ozkan, C.; Tongay, S. Fundamentals of Lateral and Vertical Heterojunctions of Atomically Thin Materials. *Nanoscale* **2016**, *8* (7), 3870–3887. https://doi.org/10.1039/c5nr08982d.

(38) Okada, M.; Kutana, A.; Kureishi, Y.; Kobayashi, Y.; Saito, Y.; Saito, T.; Shinohara, H.; Kitaura, R. Direct and Indirect Interlayer Excitons in a van Der Waals Heterostructure of HBN/WS2/MoS2/ HBN. *ACS Nano* **2018**, *12*, 2498–2505. https://doi.org/10.1021/acsnano.7b08253.

(39) Zheng, Z.; Zheng, Q.; Zhao, J. Ultrafast Electron Transfer Dynamics in Lateral Transition-Metal Dichalcogenide Heterostructures. *Electronic Structure* **2019**, *1*, 034001.

(40) Kohler, D. D.; Morrow, D. J.; Zhao, Y.; Scheeler, J. M.; Jin, S.; Wright, J. C. Photoluminescence, Reflection Contrast, Raman, and Second Harmonic Generation Spectroscopies Spatially Resolve Strain, Alloying, Defects, and Electronic Characteristics of Lateral MX2 Heterostructures. *Journal of Physical Chemistry Letters* **2023**, *14* (42), 9424–9432. https://doi.org/10.1021/acs.jpclett.3c02407.

(41) Hong, X.; Kim, J.; Shi, S. F.; Zhang, Y.; Jin, C.; Sun, Y.; Tongay, S.; Wu, J.; Zhang, Y.; Wang, F. Ultrafast Charge Transfer in Atomically Thin MoS2/WS2 Heterostructures. *Nat Nanotechnol* **2014**, *9* (9), 682–686. https://doi.org/10.1038/nnano.2014.167.

(42) Zhu, H.; Wang, J.; Gong, Z.; Kim, Y. D.; Hone, J.; Zhu, X. Y. Interfacial Charge Transfer Circumventing Momentum Mismatch at Two-Dimensional van Der Waals Heterojunctions. *Nano Lett* **2017**, *17* (6), 3591–3598. https://doi.org/10.1021/acs.nanolett.7b00748.

(43) Yao, P.; He, D.; Zereshki, P.; Wang, Y.; Zhao, H. Nonlinear Optical Effect of Interlayer Charge Transfer in a van Der Waals Heterostructure. *Appl Phys Lett* **2019**, *115* (26), 263103. https://doi.org/10.1063/1.5131165.

(44) Yuan, L.; Zheng, B.; Kunstmann, J.; Brumme, T.; Kuc, A. B.; Ma, C.; Deng, S.; Blach, D.; Pan, A.; Huang, L. Twist-Angle-Dependent Interlayer Exciton Diffusion in WS2–WSe2 Heterobilayers. *Nat Mater* **2020**. https://doi.org/10.1038/s41563-020-0670-3.

(45) Ceballos, F.; Bellus, M. Z.; Chiu, H. Y.; Zhao, H. Probing Charge Transfer Excitons in a MoSe2-WS2 van Der Waals Heterostructure. *Nanoscale* **2015**, *7* (41), 17523–17528. https://doi.org/10.1039/c5nr04723d.

(46) Kim, W.; Jeong, G.; Oh, J.; Kim, J.; Watanabe, K.; Taniguchi, T.; Ryu, S. Exciton-Sensitized Second-Harmonic Generation in 2D Heterostructures. *ACS Nano* **2023**. https://doi.org/10.1021/acsnano.3c07428.

(47) Mueller, T.; Malic, E. Exciton Physics and Device Application of Two-Dimensional Transition Metal Dichalcogenide Semiconductors. *npj 2D Materials and Applications*. Nature Publishing Group December 1, 2018. https://doi.org/10.1038/s41699-018-0074-2.

(48) Lee, C. H.; Lee, G. H.; Van Der Zande, A. M.; Chen, W.; Li, Y.; Han, M.; Cui, X.; Arefe, G.; Nuckolls, C.; Heinz, T. F.; Guo, J.; Hone, J.; Kim, P. Atomically Thin P-n Junctions with van Der Waals Heterointerfaces. *Nat Nanotechnol* **2014**, *9* (9), 676–681. https://doi.org/10.1038/nnano.2014.150.

(49) Hao, K.; Moody, G.; Wu, F.; Dass, C. K.; Xu, L.; Chen, C. H.; Sun, L.; Li, M. Y.; Li, L. J.; MacDonald, A. H.; Li, X. Direct Measurement of Exciton Valley Coherence in Monolayer WSe2. *Nat Phys* **2016**, *12* (7), 677–682. https://doi.org/10.1038/nphys3674.

(50) Volmer, F.; Ersfeld, M.; Faria Junior, P. E.; Waldecker, L.; Parashar, B.; Rathmann, L.; Dubey, S.; Cojocariu, I.; Feyer, V.; Watanabe, K.; Taniguchi, T.; Schneider, C. M.; Plucinski, L.; Stampfer, C.; Fabian, J.; Beschoten, B. Twist Angle Dependent Interlayer Transfer of Valley Polarization from Excitons to Free Charge Carriers in WSe2/MoSe2 Heterobilayers. *NPJ 2D Mater Appl* **2023**, *7* (1). https://doi.org/10.1038/s41699-023-00420-1.

(51) Van Der Zande, A. M.; Huang, P. Y.; Chenet, D. A.; Berkelbach, T. C.; You, Y.; Lee, G. H.; Heinz, T. F.; Reichman, D. R.; Muller, D. A.; Hone, J. C. Grains and Grain Boundaries in Highly Crystalline Monolayer Molybdenum Disulphide. *Nat Mater* **2013**, *12* (6), 554–561. https://doi.org/10.1038/nmat3633.

(52) Zhang, D.; Gan, L.; Zhang, J.; Zhang, R.; Wang, Z.; Feng, J.; Sun, H.; Ning, C. Z. Reconstructing Local Profile of Exciton-Emission Wavelengths across a WS2Bubble beyond the Diffraction Limit. *ACS Nano* **2020**, *14* (6), 6931–6937. https://doi.org/10.1021/acsnano.0c01337.

(53) Zhang, C.; Wang, C.; Yang, F.; Huang, J. K.; Li, L. J.; Yao, W.; Ji, W.; Shih, C. K. Engineering Point-Defect States in Monolayer WSe2. *ACS Nano* **2019**. https://doi.org/10.1021/acsnano.8b07595.

(54) Emitter, L.; Ws, M.; Peimyoo, N.; Shang, J.; Cong, C.; Shen, X.; Wu, X. Nonblinking, Intense Two-Dimensional Light Emitter: Monolayer WS2 Triangles. **2013**, No. 12, 10985–10994.

(55) Geim, A. K.; Grigorieva, I. V. Van Der Waals Heterostructures. *Nature*. 2013, pp 419–425. https://doi.org/10.1038/nature12385.

(56) Yuan, L.; Chung, T. F.; Kuc, A.; Wan, Y.; Xu, Y.; Chen, Y. P.; Heine, T.; Huang, L. Photocarrier Generation from Interlayer Charge-Transfer Transitions in WS2-Graphene Heterostructures. *Sci Adv* **2018**, *4* (2), 1–10. https://doi.org/10.1126/sciadv.1700324.

(57) Pan, D.; Fu, Y.; Spitha, N.; Zhao, Y.; Roy, C. R.; Morrow, D. J.; Kohler, D. D.; Wright, J. C.; Jin, S. Deterministic Fabrication of Arbitrary Vertical Heterostructures of Two-Dimensional Ruddlesden–Popper Halide Perovskites. *Nat Nanotechnol* **2021**, *16* (2), 159–165. https://doi.org/10.1038/s41565-020-00802-2.

(58) Shearer, M. J.; Samad, L.; Zhang, Y.; Zhao, Y.; Puretzky, A.; Eliceiri, K. W.; Wright, J. C.; Hamers, R. J.; Jin, S. Complex and Noncentrosymmetric Stacking of Layered Metal Dichalcogenide Materials Created by Screw Dislocations. *J Am Chem Soc* **2017**, *139* (9), 3496–3504. https://doi.org/10.1021/jacs.6b12559.

(59) Baiz, C. R.; Schach, D.; Tokmakoff, A. Ultrafast 2D IR Microscopy. *Opt Express* **2014**, *22* (15), 18724. https://doi.org/10.1364/oe.22.018724.

(60) Ostrander, J. S.; Serrano, A. L.; Ghosh, A.; Zanni, M. T. Spatially Resolved Two-Dimensional Infrared Spectroscopy via Wide-Field Microscopy. *ACS Photonics* **2016**, *3* (7), 1315–1323. https://doi.org/10.1021/acsphotonics.6b00297.

(61) Jones, A. C.; Kearns, N. M.; Ho, J. J.; Flach, J. T.; Zanni, M. T. Impact of Non-Equilibrium Molecular Packings on Singlet Fission in Microcrystals Observed Using 2D White-Light Microscopy. *Nat Chem* **2020**, *12* (1), 40–47. https://doi.org/10.1038/s41557-019-0368-9.

(62) Purz, T. L.; Martin, E. W.; Holtzmann, W. G.; Rivera, P.; Alfrey, A.; Bates, K. M.; Deng, H.; Xu, X.; Cundiff, S. T. Imaging Dynamic Exciton Interactions and Coupling in Transition Metal Dichalcogenides. *Journal of Chemical Physics* **2022**, *156* (21). https://doi.org/10.1063/5.0087544.

(63) Rosete-Aguilar, M.; Estrada-Silva, F. C.; Bruce, N. C.; Román-Moreno, C. J.; Ortega-Martínez, R. Calculation of Temporal Spreading of Ultrashort Pulses Propagating through Optical Glasses. *Revista Mexicana de Fisica* **2008**, *54* (2), 141–148.

(64) Ian R. Kenyon. *The Light Fantastic: A Modern Introduction to Classical and Quantum Optics*, 2nd ed.; Oxfod University Press, 2011.

(65) Battey, D. E.; Slater, J. B.; Wludyka, R.; Owen, H.; Pallister, D. M.; Morris, M. D. Axial Transmissive f/1.8 Imaging Raman Spectrograph with Volume-Phase Holographic Filter and Grating. *Appl Spectrosc* **1993**, *47* (11), 1913–1919.

(66) Kumar, N.; Najmaei, S.; Cui, Q.; Ceballos, F.; Ajayan, P. M.; Lou, J.; Zhao, H. Second Harmonic Microscopy of Monolayer MoS2. *Phys Rev B Condens Matter Mater Phys* **2013**, *87* (16). https://doi.org/10.1103/PhysRevB.87.161403.

(67) Janisch, C.; Wang, Y.; Ma, D.; Mehta, N.; Elías, A. L.; Perea-López, N.; Terrones, M.; Crespi, V.; Liu, Z. Extraordinary Second Harmonic Generation in Tungsten Disulfide Monolayers. *Sci Rep* **2014**, *4*. https://doi.org/10.1038/srep05530.

(68) Maragkakis, G. M.; Psilodimitrakopoulos, S.; Mouchliadis, L.; Paradisanos, I.; Lemonis, A.; Kioseoglou, G.; Stratakis, E. Imaging the Crystal Orientation of 2D Transition Metal Dichalcogenides Using Polarizationresolved Second-Harmonic Generation. *Opto-Electronic Advances* **2019**, *2* (11), 1–8. https://doi.org/10.29026/oea.2019.190026.

(69) Mennel, L.; Paur, M.; Mueller, T. Second Harmonic Generation in Strained Transition Metal Dichalcogenide Monolayers: MoS 2 , MoSe 2 , WS 2 , and WSe 2. *APL Photonics* **2019**, *4* (3). https://doi.org/10.1063/1.5051965.

(70) Mennel, L.; Furchi, M. M.; Wachter, S.; Paur, M.; Polyushkin, D. K.; Mueller, T. Optical Imaging of Strain in Two-Dimensional Crystals. *Nat Commun* **2018**, *9* (1). https://doi.org/10.1038/s41467-018-02830-y.

(71) Autere, A.; Jussila, H.; Marini, A.; Saavedra, J. R. M.; Dai, Y.; Säynätjoki, A.; Karvonen, L.; Yang, H.; Amirsolaimani, B.; Norwood, R. A.; Peyghambarian, N.; Lipsanen, H.; Kieu, K.; De Abajo, F. J. G.; Sun, Z. Optical Harmonic Generation in Monolayer Group-VI Transition Metal Dichalcogenides. *Phys Rev B* **2018**, *98* (11), 1–7. https://doi.org/10.1103/PhysRevB.98.115426.

(72) Sie, E. J.; Nyby, C. M.; Pemmaraju, C. D.; Park, S. J.; Shen, X.; Yang, J.; Hoffmann, M. C.; Ofori-Okai, B. K.; Li, R.; Reid, A. H.; Weathersby, S.; Mannebach, E.; Finney, N.; Rhodes, D.; Chenet, D.; Antony, A.; Balicas, L.; Hone, J.; Devereaux, T. P.; Heinz, T. F.; Wang, X.; Lindenberg, A. M. An Ultrafast Symmetry Switch in a Weyl Semimetal. *Nature* **2019**, *565* (7737), 61–66. https://doi.org/10.1038/s41586-018-0809-4.

(73) Shank, C. V; Yen, R.; Hirlimann, C. *Femtosecond-Time-Resolved Surface Structural Dynamics of Optically Excited Silicon*; Vol. 51.

(74) Zimmermann, J. E.; Kim, Y. D.; Hone, J. C.; Höfer, U.; Mette, G. Directional Ultrafast Charge Transfer in a WSe2/MoSe2heterostructure Selectively Probed by Time-Resolved SHG Imaging Microscopy. *Nanoscale Horiz* **2020**, *5* (12), 1603–1609. https://doi.org/10.1039/d0nh00396d.

(75) Zimmermann, J. E.; Axt, M.; Mooshammer, F.; Nagler, P.; Schüller, C.; Korn, T.; Höfer, U.; Mette, G. Ultrafast Charge-Transfer Dynamics in Twisted MoS$_2$/WSe$_2$ Heterostructures. **2021**. https://doi.org/10.1021/acsnano.1c04549.

(76) Gross, N.; Kuhs, C. T.; Ostovar, B.; Chiang, W. Y.; Wilson, K. S.; Volek, T. S.; Faitz, Z. M.; Carlin, C. C.; Dionne, J. A.; Zanni, M. T.; Gruebele, M.; Roberts, S. T.; Link, S.; Landes, C. F. Progress and Prospects in Optical Ultrafast Microscopy in the Visible Spectral Region: Transient Absorption and Two-Dimensional Microscopy. *Journal of Physical Chemistry C*. American Chemical Society August 3, 2023, pp 14557–14586. https://doi.org/10.1021/acs.jpcc.3c02091.

(77) Nah, S.; Spokoyny, B. M.; Soe, C. M. M.; Stoumpos, C. C.; Kanatzidis, M. G.; Harel, E. Ultrafast Imaging of Carrier Cooling in Metal Halide Perovskite Thin Films. *Nano Lett* **2018**, *18* (2), 1044–1048. https://doi.org/10.1021/acs.nanolett.7b04520.

(78) Morrow, D. J.; Kohler, D. D.; Zhao, Y.; Jin, S.; Wright, J. C. Triple Sum Frequency Pump-Probe Spectroscopy of Transition Metal Dichalcogenides. *Phys Rev B* **2019**, *100* (23), 1–16. https://doi.org/10.1103/PhysRevB.100.235303.

(79) Zimmermann, J. E.; Li, B.; Hone, J. C.; Höfer, U.; Mette, G. Second-Harmonic Imaging Microscopy for Time-Resolved Investigations of Transition Metal Dichalcogenides. *Journal of Physics Condensed Matter* **2020**, *32* (48). https://doi.org/10.1088/1361-648X/aba946.

(80) Wang, Q.; Ge, S.; Li, X.; Qiu, J.; Ji, Y.; Feng, J.; Sun, D. Valley Carrier Dynamics in Monolayer Molybdenum Disulfide from Helicity-Resolved Ultrafast Pump-Probe Spectroscopy. *ACS Nano* **2013**, *7* (12), 11087–11093. https://doi.org/10.1021/nn405419h.

(81) Zhu, Z. Y.; Cheng, Y. C.; Schwingenschlögl, U. Giant Spin-Orbit-Induced Spin Splitting in Two-Dimensional Transition-Metal Dichalcogenide Semiconductors. *Phys Rev B Condens Matter Mater Phys* **2011**, *84* (15), 1–5. https://doi.org/10.1103/PhysRevB.84.153402.

(82) Xiao, D.; Liu, G. Bin; Feng, W.; Xu, X.; Yao, W. Coupled Spin and Valley Physics in Monolayers of MoS 2 and Other Group-VI Dichalcogenides. *Phys Rev Lett* **2012**, *108* (19), 1–5. https://doi.org/10.1103/PhysRevLett.108.196802.

(83) Xu, X.; Yao, W.; Xiao, D.; Heinz, T. F. Spin and Pseudospins in Layered Transition Metal Dichalcogenides. *Nat Phys* **2014**, *10* (5), 343–350. https://doi.org/10.1038/nphys2942.

(84) Lin, X.; Yang, W.; Wang, K. L.; Zhao, W. Two-Dimensional Spintronics for Low-Power Electronics. *Nature Electronics*. Nature Publishing Group July 1, 2019, pp 274–283. https://doi.org/10.1038/s41928-019-0273-7.

(85) Sierra, J. F.; Fabian, J.; Kawakami, R. K.; Roche, S.; Valenzuela, S. O. Van Der Waals Heterostructures for Spintronics and Opto-Spintronics. *Nature Nanotechnology*. Nature Research August 1, 2021, pp 856–868. https://doi.org/10.1038/s41565-021-00936-x.

(86) Chhowalla, M.; Jena, D.; Zhang, H. Two-Dimensional Semiconductors for Transistors. **2016**. https://doi.org/10.1038/natrevmats2016.52.

(87) Seyler, K. L.; Rivera, P.; Yu, H.; Wilson, N. P.; Ray, E. L.; Mandrus, D. G.; Yan, J.; Yao, W.; Xu, X. Signatures of Moiré-Trapped Valley Excitons in MoSe 2 /WSe 2 Heterobilayers. *Nature* **2019**, *567* (7746), 66–70. https://doi.org/10.1038/s41586-019-0957-1.

(88) Jin, C.; Regan, E. C.; Yan, A.; Utama, M. I. B.; Wang, D.; Zhao, S.; Qin, Y.; Yang, S.; Zheng, Z.; Shi, S.; Watanabe, K.; Taniguchi, T.; Tongay, S.; Zettl, A.; Wang, F. Observation of Moiré Excitons in WSe2/WS2 Heterostructure Superlattices. *Nature* **2019**, *567*, 2–7. https://doi.org/10.1038/s41586-019-0976-y.

(89) Hong, X.; Kim, J.; Shi, S. F.; Zhang, Y.; Jin, C.; Sun, Y.; Tongay, S.; Wu, J.; Zhang, Y.; Wang, F. Ultrafast Charge Transfer in Atomically Thin MoS2/WS2 Heterostructures. *Nat Nanotechnol* **2014**, *9* (9), 682–686. https://doi.org/10.1038/nnano.2014.167.

(90) Rivera, P.; Schaibley, J. R.; Jones, A. M.; Ross, J. S.; Wu, S.; Aivazian, G.; Klement, P.; Seyler, K.; Clark, G.; Ghimire, N. J.; Yan, J.; Mandrus, D. G.; Yao, W.; Xu, X. Observation of Long-Lived Interlayer Excitons in Monolayer MoSe 2-WSe 2 Heterostructures. *Nat Commun* **2015**, *6*. https://doi.org/10.1038/ncomms7242.

(91) Jiang, C.; Xu, W.; Rasmita, A.; Huang, Z.; Li, K.; Xiong, Q.; Gao, W. B. Microsecond Dark-Exciton Valley Polarization Memory in Two-Dimensional Heterostructures. *Nat Commun* **2018**, *9* (1). https://doi.org/10.1038/s41467-018-03174-3.

(92) Rivera, P.; Seyler, K. L.; Yu, H.; Schaibley, J. R.; Yan, J.; Mandrus, D. G.; Yao, W.; Xu, X.; Science, S. O. *Valley-Polarized Exciton Dynamics in a 2D Semiconductor Heterostructure*; 2016; Vol. 351. https://www.science.org.

(93) Zhang, L.; Zhang, Z.; Wu, F.; Wang, D.; Gogna, R.; Hou, S.; Watanabe, K.; Taniguchi, T.; Kulkarni, K.; Kuo, T.; Forrest, S. R.; Deng, H. Twist-Angle Dependence of Moiré Excitons in WS2/MoSe2 Heterobilayers. *Nat Commun* **2020**, *11* (1), 1–8. https://doi.org/10.1038/s41467-020-19466-6.

(94) Yuan, Y.; Liu, P.; Wu, H.; Chen, H.; Zheng, W.; Peng, G.; Zhu, Z.; Zhu, M.; Dai, J.; Qin, S.; Novoselov, K. S. Probing the Twist-Controlled Interlayer Coupling in Artificially Stacked Transition Metal Dichalcogenide Bilayers by Second-Harmonic Generation. *ACS Nano* **2023**. https://doi.org/10.1021/acsnano.3c03795.

(95) Wu, K.; Zhong, H.; Guo, Q.; Tang, J.; Zhang, J.; Qian, L.; Shi, Z.; Zhang, C.; Yuan, S.; Zhang, S.; Xu, H. Identification of Twist-Angle-Dependent Excitons in WS2/WSe2 Heterobilayers. *Natl Sci Rev* **2021**, No. November 2020. https://doi.org/10.1093/nsr/nwab135.

(96) Lin, K. Q.; Faria Junior, P. E.; Bauer, J. M.; Peng, B.; Monserrat, B.; Gmitra, M.; Fabian, J.; Bange, S.; Lupton, J. M. Twist-Angle Engineering of Excitonic Quantum Interference and Optical Nonlinearities in Stacked 2D Semiconductors. *Nat Commun* **2021**, *12* (1). https://doi.org/10.1038/s41467-021-21547-z.

(97) Zeng, Z.; Sun, X.; Zhang, D.; Zheng, W.; Fan, X.; He, M.; Xu, T.; Sun, L.; Wang, X.; Pan, A. Controlled Vapor Growth and Nonlinear Optical Applications of Large-Area 3R Phase WS 2 and WSe 2 Atomic Layers. *Adv Funct Mater* **2019**, *29* (11). https://doi.org/10.1002/adfm.201806874.

(98) Kim, W.; Ahn, J. Y.; Oh, J.; Shim, J. H.; Ryu, S. Second-Harmonic Young's Interference in Atom-Thin Heterocrystals. *Nano Lett* **2020**, *20* (12), 8825–8831. https://doi.org/10.1021/acs.nanolett.0c03763.

(99) Solomon, J. M.; Ahmad, S. I.; Dave, A.; Lu, L. S.; Wu, Y. C.; Chang, W. H.; Luo, C. W.; Her, T. H. Ultrafast Multi-Shot Ablation and Defect Generation in Monolayer Transition Metal Dichalcogenides. *AIP Adv* **2022**, *12* (1). https://doi.org/10.1063/5.0078054.

(100) Mannebach, E. M.; Duerloo, K. A. N.; Pellouchoud, L. A.; Sher, M. J.; Nah, S.; Kuo, Y. H.; Yu, Y.; Marshall, A. F.; Cao, L.; Reed, E. J.; Lindenberg, A. M. Ultrafast Electronic and Structural Response of Monolayer MoS2 under Intense Photoexcitation Conditions. *ACS Nano* **2014**, *8* (10), 10734–10742. https://doi.org/10.1021/nn5044542.

(101) Wu, P.; Zhang, T.; Zhu, J.; Palacios, T.; Kong, J. 2D Materials for Logic Device Scaling. *Nat Mater* **2024**, *23* (1), 23–25. https://doi.org/10.1038/s41563-023-01715-w.

(102) Purz, T. L.; Martin, E. W.; Holtzmann, W. G.; Rivera, P.; Alfrey, A.; Bates, K. M.; Deng, H.; Xu, X.; Cundiff, S. T. Imaging Dynamic Exciton Interactions and Coupling in Transition Metal Dichalcogenides. **2022**.

(103) Liu, F.; Wu, W.; Bai, Y.; Chae, S. H.; Li, Q.; Wang, J.; Hone, J.; Zhu, X.-Y. Disassembling 2D van Der Waals Crystals into Macroscopic Monolayers and Reassembling into Artificial Lattices. *Science (1979)* **2020**, *367* (6480), 903–906. https://doi.org/10.1126/science.aba1416.

(104) Sunden, K. F.; Kohler, D. D.; Meyer, K. A.; Cruz Parrilla, P. L.; Wright, J. C.; Thompson, B. J. The Yaq Project: Standardized Software Enabling Flexible Instrumentation. *Review of Scientific Instruments* **2023**, *94* (4). https://doi.org/10.1063/5.0135255.

(105) Sunden, K.; Thompson, B. Bluesky-Cmds. July 26, 2022.

(106) Li, Y.; Heinz, T. F. Two-Dimensional Models for the Optical Response of Thin Films. *2d Mater* **2018**, *5* (2). https://doi.org/10.1088/2053-1583/aab0cf.

(107) Wu, S.-S.; Huang, T.-X.; Xu, X.; Bao, Y.-F.; Pei, X.-D.; Yao, X.; Cao, M.-F.; Lin, K.-Q.; Wang, X.; Wang, D.; Ren, B. Quantitatively Deciphering Electronic Properties of Defects at Atomically Thin Transition-Metal Dichalcogenides. *ACS Nano* **2022**. https://doi.org/10.1021/acsnano.2c00096.

(108) Pogna, E. A. A.; Marsili, M.; De Fazio, D.; Dal Conte, S.; Manzoni, C.; Sangalli, D.; Yoon, D.; Lombardo, A.; Ferrari, A. C.; Marini, A.; Cerullo, G.; Prezzi, D. Photo-Induced Bandgap Renormalization Governs the Ultrafast Response of Single-Layer MoS2. *ACS Nano* **2016**, *10* (1), 1182–1188. https://doi.org/10.1021/acsnano.5b06488.

(109) Trovatello, C.; Katsch, F.; Li, Q.; Zhu, X.; Knorr, A.; Cerullo, G.; Dal Conte, S. Disentangling Many-Body Effects in the Coherent Optical Response of 2D Semiconductors. *Nano Lett* **2022**. https://doi.org/10.1021/acs.nanolett.2c01309.

(110) Amin, B.; Kaloni, T. P.; Schreckenbach, G.; Freund, M. S. Materials Properties of Out-of-Plane Heterostructures of MoS2-WSe2 and WS2-MoSe2. *Appl Phys Lett* **2016**, *108* (6). https://doi.org/10.1063/1.4941755.

(111) Nie, Z.; Trovatello, C.; Pogna, E. A. A.; Dal Conte, S.; Miranda, P. B.; Kelleher, E.; Zhu, C.; Turcu, I. C. E.; Xu, Y.; Liu, K.; Cerullo, G.; Wang, F. Broadband Nonlinear Optical Response of Monolayer MoSe2 under Ultrafast Excitation. *Appl Phys Lett* **2018**, *112* (3). https://doi.org/10.1063/1.5010060.

(112) Li, Z.; Klein, T. R.; Kim, D. H.; Yang, M.; Berry, J. J.; Van Hest, M. F. A. M.; Zhu, K. Scalable Fabrication of Perovskite Solar Cells. *Nature Reviews Materials*. Nature Publishing Group March 27, 2018. https://doi.org/10.1038/natrevmats.2018.17.

(113) Unuchek, D.; Ciarrocchi, A.; Avsar, A.; Watanabe, K.; Taniguchi, T.; Kis, A. Room-Temperature Electrical Control of Exciton Flux in a van Der Waals Heterostructure. *Nature* **2018**, *560* (7718), 340–344. https://doi.org/10.1038/s41586-018-0357-y.

(114) Berghäuser, G.; Steinleitner, P.; Merkl, P.; Huber, R.; Knorr, A.; Malic, E. Mapping of the Dark Exciton Landscape in Transition Metal Dichalcogenides. *Phys Rev B* **2018**, *98* (2), 1–6. https://doi.org/10.1103/PhysRevB.98.020301.

(115) Liu, F.; Li, Q.; Zhu, X. Direct Determination of Momentum-Resolved Electron Transfer in the Photoexcited van Der Waals Heterobilayer WS2/MoS2. *Phys Rev B* **2020**, *101* (20), 201405. https://doi.org/10.1103/PhysRevB.101.201405.

(116) Boschini, F.; Zonno, M.; Damascelli, A. Time-Resolved ARPES Studies of Quantum Materials. *Rev Mod Phys* **2024**, *96* (1). https://doi.org/10.1103/RevModPhys.96.015003.

(117) Zhang, K.; Lin, M. F.; Ryland, E. S.; Verkamp, M. A.; Benke, K.; De Groot, F. M. F.; Girolami, G. S.; Vura-Weis, J. Shrinking the Synchrotron: Tabletop Extreme Ultraviolet Absorption of Transition-Metal Complexes. *Journal of Physical Chemistry Letters* **2016**, *7* (17), 3383–3387. https://doi.org/10.1021/acs.jpclett.6b01393.

(118) Sie, E. J.; Rohwer, T.; Lee, C.; Gedik, N. Time-Resolved XUV ARPES with Tunable 24–33 EV Laser Pulses at 30 MeV Resolution. *Nat Commun* **2019**, *10* (1). https://doi.org/10.1038/s41467-019-11492-3.

(119) Thouin, F.; Neutzner, S.; Cortecchia, D.; Dragomir, V. A.; Soci, C.; Salim, T.; Lam, Y. M.; Leonelli, R.; Petrozza, A.; Kandada, A. R. S.; Silva, C. Stable Biexcitons in Two-Dimensional Metal-Halide Perovskites with Strong Dynamic Lattice Disorder. *Phys Rev Mater* **2018**, *2* (3), 1–10. https://doi.org/10.1103/PhysRevMaterials.2.034001.

(120) Riebe, M. T.; Wright, J. C. Spectral Line-Narrowing and Saturation Effects in Fully Resonant Nondegenerate Four Wave Mixing. *J Chem Phys* **1988**, *88* (5), 2981–2994. https://doi.org/10.1063/1.453939.

(121) Carlson, R. J.; Wright, J. C. Line Narrowing in Multiresonant Third Order Molecular Spectroscopies. *J Mol Spectrosc* **1990**, *143*, 1–17.

(122) Carlson, R. J.; Wright, J. C. Absorption and Coherent Interference Effects in Multiply Four-Wave Mixing Spectroscopy. *Appl Spectrosc* **1988**, *43*, 413.

(123) Danovich, M.; Zólyomi, V.; Fal'ko, V. I.; Aleiner, I. L. Auger Recombination of Dark Excitons in WS2 and WSe2 Monolayers. *2d Mater* **2016**, *3* (3). https://doi.org/10.1088/2053-1583/3/3/035011.

(124) Zhao, Y.; Jin, S. Controllable Water Vapor Assisted Chemical Vapor Transport Synthesis of WS2-MoS2Heterostructure. *ACS Mater Lett* **2020**, *2* (1), 42–48. https://doi.org/10.1021/acsmaterialslett.9b00415.

(125) Jung, G. H.; Yoo, S. J.; Park, Q. H. Measuring the Optical Permittivity of Two Dimensional Materials without a Priori Knowledge of Electronic Transitions. *Nanophotonics* **2018**, *8* (2), 263–270. https://doi.org/10.1515/nanoph-2018-0120.

(126) Lin, K. Q.; Ong, C. S.; Bange, S.; Faria Junior, P. E.; Peng, B.; Ziegler, J. D.; Zipfel, J.; Bäuml, C.; Paradiso, N.; Watanabe, K.; Taniguchi, T.; Strunk, C.; Monserrat, B.; Fabian, J.; Chernikov, A.; Qiu, D. Y.; Louie, S. G.; Lupton, J. M. Narrow-Band High-Lying Excitons with Negative-Mass Electrons in Monolayer WSe2. *Nat Commun* **2021**, *12* (1), 1–8. https://doi.org/10.1038/s41467-021-25499-2.

(127) Li, X.; Fu, Y.; Pedesseau, L.; Guo, P.; Cuthriell, S.; Hadar, I.; Even, J.; Katan, C.; Stoumpos, C. C.; Schaller, R. D.; Harel, E.; Kanatzidis, M. G. Negative Pressure Engineering with Large Cage Cations in 2D Halide Perovskites Causes Lattice Softening. *J Am Chem Soc* **2020**, *142* (26), 11486–11496. https://doi.org/10.1021/jacs.0c03860.

(128) Gillen, R.; Maultzsch, J. Interlayer Excitons in MoSe2 / WSe2 Heterostructures from First Principles. *Phys Rev B* **2018**, *97*, 165306. https://doi.org/10.1103/PhysRevB.97.165306.

(129) Koåmider, K.; Fernández-Rossier, J. Electronic Properties of the MoS2-WS2 Heterojunction. *Phys Rev B Condens Matter Mater Phys* **2013**, *87* (7), 2–5. https://doi.org/10.1103/PhysRevB.87.075451.

(130) Wang, H.; Bang, J.; Sun, Y.; Liang, L.; West, D.; Meunier, V.; Zhang, S. The Role of Collective Motion in the Ultrafast Charge Transfer in van Der Waals Heterostructures. *Nat Commun* **2016**, *7* (May), 1–9. https://doi.org/10.1038/ncomms11504.

(131) Liu, J.; Zhang, X.; Lu, G. Excitonic Effect Drives Ultrafast Dynamics in van Der Waals Heterostructures. *Nano Lett* **2020**, *20* (6), 4631–4637. https://doi.org/10.1021/acs.nanolett.0c01519.

(132) Long, R.; Prezhdo, O. V. Quantum Coherence Facilitates Efficient Charge Separation at a MoS2/MoSe2 van Der Waals Junction. *Nano Lett* **2016**, *16* (3), 1996–2003. https://doi.org/10.1021/acs.nanolett.5b05264.

(133) Sun, D.; Rao, Y.; Reider, G. A.; Chen, G.; You, Y.; Brézin, L.; Harutyunyan, A. R.; Heinz, T. F. Observation of Rapid Exciton-Exciton Annihilation in Monolayer Molybdenum Disulfide. *Nano Lett* **2014**, *14* (10), 5625–5629. https://doi.org/10.1021/nl5021975.

(134) Morrow, D. J.; Kohler, D. D.; Zhao, Y.; Jin, S.; Wright, J. C. Triple Sum Frequency Pump-Probe Spectroscopy of Transition Metal Dichalcogenides. *Phys Rev B* **2019**, *100* (23), 1–16. https://doi.org/10.1103/PhysRevB.100.235303.

(135) Kearns, N. M.; Mehlenbacher, R. D.; Jones, A. C.; Zanni, M. T. Broadband 2D Electronic Spectrometer Using White Light and Pulse Shaping: Noise and Signal Evaluation at 1 and 100 KHz. *Opt Express* **2017**, *25* (7), 7869. https://doi.org/10.1364/oe.25.007869.

(136) Wang, T.; Hopper, T. R.; Mondal, N.; Liu, S.; Yao, C.; Zheng, X.; Torrisi, F.; Bakulin, A. A. Hot Carrier Cooling and Trapping in Atomically Thin WS2 Probed by Three-Pulse Femtosecond Spectroscopy. *ACS Nano* **2023**, *17* (7), 6330–6340. https://doi.org/10.1021/acsnano.2c10479.

APPENDIX

6 Appendix A - Optical layout of fs system

The Wright Group added the fs system to its laser lab around 2010. The desire to study semiconductor materials systems, where the charge carrier dynamics are equally important as their spectral signatures and occur on time scales less than 1 ps, motivated the implementation of the system. Figure A1 illustrates the upstream optical layout of the fs system. The configuration of these optics/lasers was static throughout much of my graduate school career. They are responsible for the preparation of the excitation beams (scannable frequency range, time delay, pulse fluence) before being sent to the traditional CMDS spectrometer/microscope, where the optical alignments are more fluid depending on the experiment.

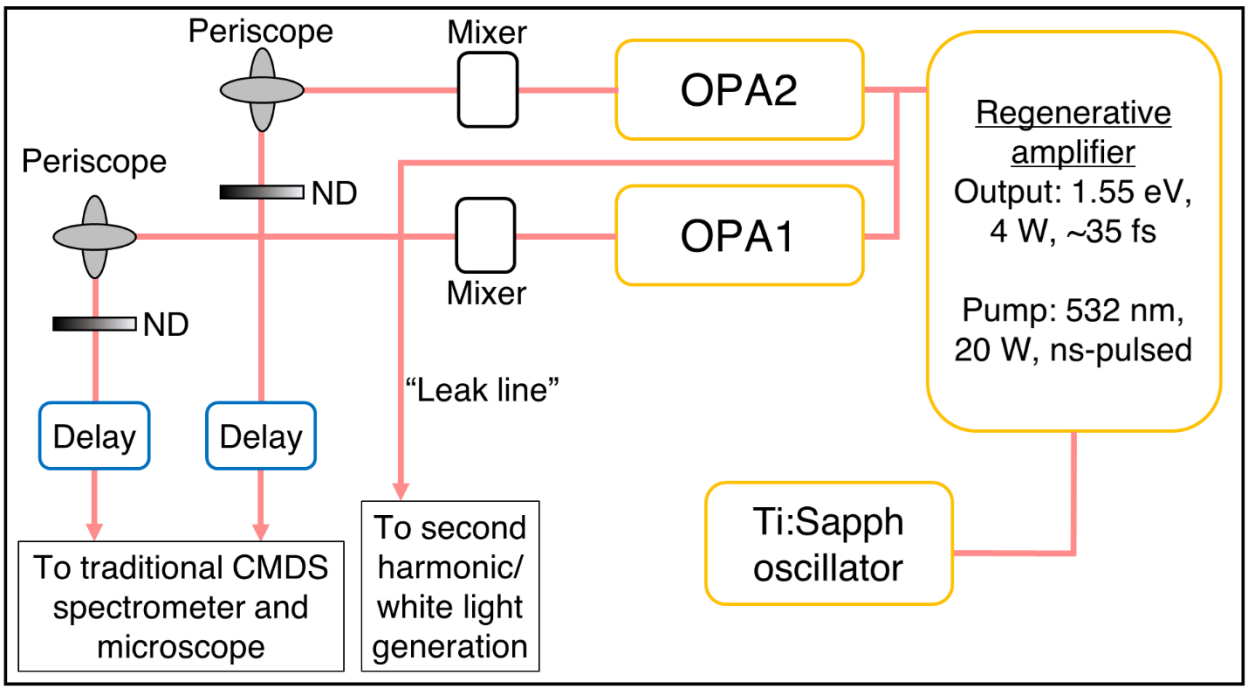

Figure A1 | Upstream optical layout of the fs system in the Wright Group.

The fs system starts with a Ti:Sapph oscillator (Tsunami, Spectra-Physics) that outputs pulses centered at 1.55 eV with a temporal pulse duration of ~35 fs and a repetition rate of 1 kHz. The oscillator seeds a regenerate amplifier (Spitfire, Spectra-Physics) that outputs pulses centered at the same central frequency and with the same temporal duration as the seed. It outputs a total power of 4 W. 20 W of a ns-pulsed diode laser centered at 532 nm pumps the amplifier. A little less than half of the amplifier output is sent to an optical parametric amplifier (OPA; Topas-C, Light Conversion) which has been named "OPA2." The remaining power is sent to another OPA of the same make and model which has been named "OPA1." A few percent of the amplifier output is picked off on its way from OPA2 to OPA1 which the Group has named the "Leak line." We use the Leak line in three different ways: 1) unchanged as 1.55 eV, 2) frequency-doubled at 3.10 eV, or 3) used as the seed for white light generation.

The OPAs have two amplifying stages and typically have output powers (signal + idler beams) of 600-700 mW. The signal, idler, and 1.55 eV pump beams are further combined in nonlinear crystals housed in the Mixers to create energy ranges that span from the MIR to the UV. The OPA ranges most used in this dissertation are signal (0.8-1.05 eV), idler (0.55-0.8 eV), second harmonic signal (1.6-2.1 eV), and second harmonic idler (1.10-1.6 eV).

After the Mixers, both beams are sent through a periscope that unifies the two polarizations in addition to lowering the beam height. The beams are vertically polarized after exiting the periscope. The beams are then sent through a mechanically controlled variable neutral density (ND) wheel to control the pulse fluence. Finally, the beams are sent through a delay stage that controls the time at which the pulses arrive at the sample position.

7 Appendix B - Additional proof-of-principle measurements performed using widefield nonlinear microscope

The following sections present measurements on 2D Ruddlesden-Popper (RP) perovskite samples provided by the Jin group using the widefield nonlinear microscope outlined in Chapter 2. The Jin group members I collaborated with and I thought of interesting and exciting experiments to try on these samples using the microscope I built. The motivation behind these experiments was materials driven and the new widefield pump-SHG probe microscopy technique could answer the questions we had. There was a low risk, high reward to perform those experiments but unfortunately they weren't successful. After these experiments were completed, I decided to take preliminary, proof-of-principle measurements on these samples to show fellow Wright and Jin group members the versatility of the instrument. Thus, these measurements act more as an advertisement to potential future users rather than to gain scientific insight into perovskite photophysics.

These measurements supplement the transient SHG and transient transmission data taken on the TMD HBL samples in Chapter 2.

7.1 Widefield transient THG microscopy on thick $(PA)_2(EA)Pb_2I_7$ microcrystals

Using THG as a nonlinear probe is a promising instrumental capability to utilize because there are no symmetry requirements like SHG. THG can probe all samples. Of course, this means that the substrate produces THG but when the sample possesses strong excitonic transition dipoles, like in the case of TMDs and RP perovskites, the material response is orders of magnitude

greater than the substrate response. Like SHG, THG is sensitive to the polarization of the fundamental field. Heterostructures with constituent materials that have different $\chi^{(3)}$ tensors, or the same $\chi^{(3)}$ tensor but are rotated with respect to one another, can be isolated by the correct combination of polarization optics. In other words, the polarizations conditions of the experiment can "turn off" the THG from one material and only pass THG from the other material. This would be particularly useful for charge transfer experiments where the pump selectively excites the material with the lower energy bandgap, and the probe polarization can be set to selectively interrogate the material with the higher energy bandgap.

Figure B1 shows the proof of principle measurements taken on three thick $(PA)_2(EA)Pb_2I_7$ (PA=pentylammonium, EA=ethylammonium) microcrystals. The fundamental energy is 1.0 eV and therefore the THG output energy is 3.0 eV. The pump energy is 3.1 eV and has a fluence of ~40 μJ/cm^2. Filters before the imaging spectrograph slit get rid of pump scatter and photoluminescence from the perovskites so that only THG photons create the image. Figure B1a is a false-color reflection image from a white light lamp of the three crystals. Figure B1b is a transient THG image taken at pulse overlap. It plots the relative change in THG intensity induced by the pump, $\frac{\Delta THG}{THG} = \frac{THG_{pumped} - THG_{unpumped}}{THG_{unpumped}}$. The entire area of all three microcrystals have decreased THG which is likely due to bleaching from Pauli blocking. The ΔTHG/THG magnitude for the interior of the crystals (not the border which, perhaps artificially, has a significantly higher amount of THG decrease) is in the range of 5-15%. The different facets seen in the lamp image are only faintly made out in the transient THG image. Figure B1c presents the spatially averaged dynamics for the three well-separated crystals. As might be expected, the three

crystals show qualitatively similar dynamics with a large decrease in THG at pulse overlap (0 ps).

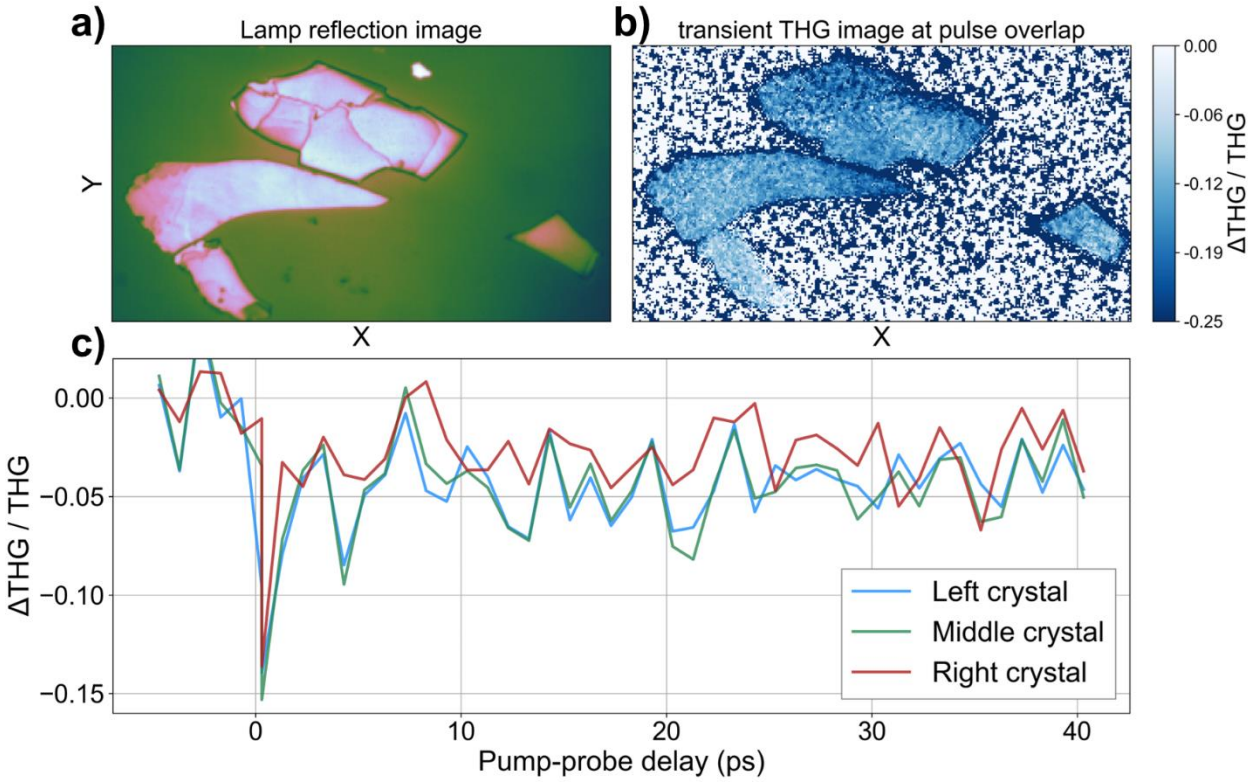

Figure B1 | Transient THG microscopy on 2D perovskite microcrystals. a) False-color image taken with a white light lamp in a reflection geometry. b) transient THG image taken at pulse overlap. All crystals show a decrease in pumped THG intensity, likely due to Pauli blocking. c) Spatially averaged dynamics for the three well-separated crystals (left, middle, right). The three crystals show qualitatively similar dynamics.

7.2 Widefield transient transmission (ΔT/T) microscopy on a Pb/Sn halide perovskite heterostructure

These measurements demonstrate the microscope's capability to perform more conventional transient absorption microscopy experiments that use linear probes. These measurements did not

have the optimal chopping routine for a pump-linear probe experiment (see Chapter 4.1), but the transient transmission signal was strong enough to still make out the pump-induced behavior. The experiment was performed on a Pb/Sn halide perovskite heterostructure. The Pb phase was composed of $(HA)_2PbI_4$ and the Sn phase was composed of $(FPEA)_2SnI_4$ (FPEA=4-fluorophenethyl ammonium). The pump had an energy of 1.55 eV at a fluence of ~300 μJ/cm^2 and therefore two-photon absorption was used to create a population. The probe was centered at a wavelength of 630 nm which is the exciton wavelength of the Sn phase. A 630-nm bandpass filter was placed in front of the imaging spectrograph to collect only the probe pulse. Figure B2a shows a white light lamp image in reflection at 630 nm. The Pb phase is the square layer on the left side of the structure that resembles a postage stamp (dashed white box). The Sn phase is the

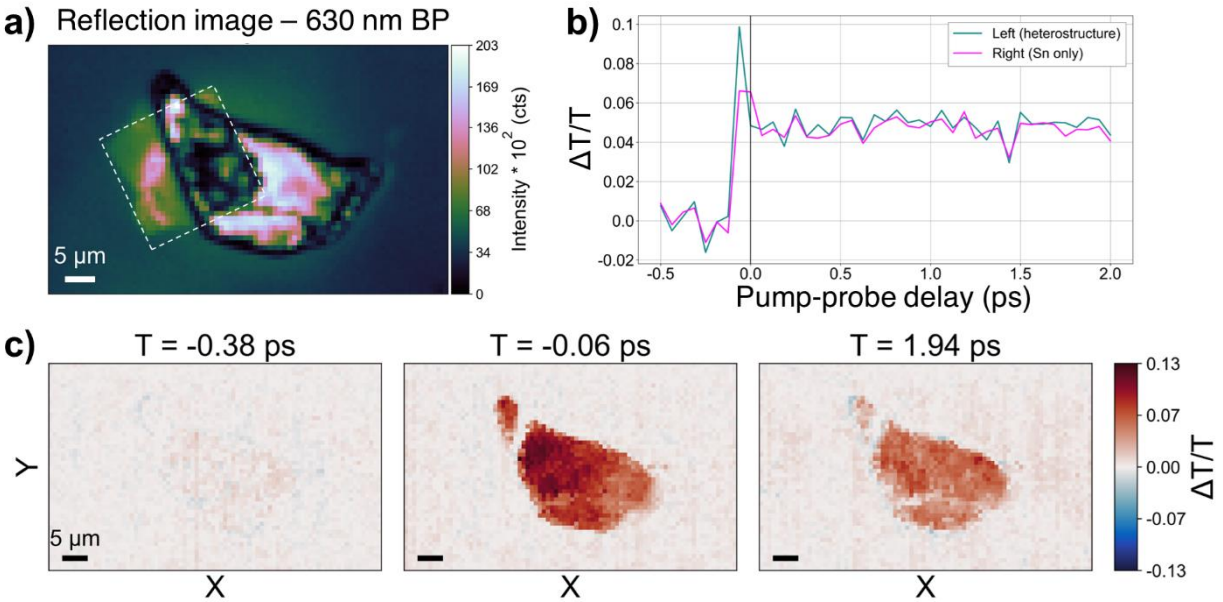

Figure B2 | Transient transmission measurements on a Pb/Sn perovskite heterostructure. a) white light lamp reflection image filtered through a 630-nm bandpass filter, equal to the exciton energy of the Sn phase. The Pb phase is the smaller structure outlined by the dashed white box and the Sn phase is the bigger structure that's centered in the image. b) spatially averaged dynamics of the heterostructure region (teal trace) and Sn-only region (magenta trace). The heterostructure region has increased ΔT/T at pulse overlap compared to the Sn-only region. c) ΔT/T images of the Pb-Sn heterostructure before, at, and after pulse delay. Asymmetry in the ΔT/T values comparing the heterostructure to the Sn-only region can be seen at pulse overlap but wash away for later delay times.

large structure that's centered in the image. Figure B2b presents spatially averaged dynamics of the two regions: the heterostructure region (teal trace) and the Sn-only region (magenta trace). ΔT/T is plotted and is represented mathematically as $\frac{\Delta T}{T} = \frac{T_{pumped} - T_{unpumped}}{T_{unpumped}}$. The heterostructure trace peaks at ~10% change at pulse overlap and the Sn-only trace peaks at about 7%. The difference in peak signal values could be explained by CT but supporting evidence is needed to make that claim. The dynamics past pulse overlap are qualitatively the same. Figure B2c shows three ΔT/T images at varying delay times. There is minimal structure before zero delay (left image). At pulse overlap (middle image) there is a strong increase in transmission throughout the entirety of the structure. There is asymmetry in the ΔT/T magnitude throughout the structure, however. Where the Pb-phase stamp is on the left has a higher ΔT/T value compared to the Sn-only right side. Because the pump is doing two-photon absorption, the Pb phase may be getting populated from the pump as well which rules out any *clear* indication of CT. However, the asymmetry seen in the image at pulse overlap merits further investigation using this technique on a similar sample morphology. At a pump-probe delay of 1.94 ps (right image), the ΔT/T signal persists but the asymmetry is washed out.

8 Appendix C - Nonlinear Widefield Microscope Best Practices

8.1 Introduction

I use this appendix to deposit much of the information and know-how I've developed over the years working with the nonlinear widefield microscope and pass it on to current and future Wright Group members. In terms of having the capability to take reproducible, publishable data, the microscope is still in its infancy. Undoubtedly there will be further optimization of the microscope workflow to get from the initial stage of loading the sample to the final stage of taking scans. The steps in the following section are thus bulleted, and not numbered, as the order of steps may change depending on the type of experiment. However, the bullets are ordered in such a way that represents my average workflow in getting from sample loading to taking scans.

Up until the sample position, the microscope excitation's conditions are quite similar to traditional Wright Group CMDS experimental setups. Finding zero delay using the microscope is analogous to finding zero delay on the traditional fs system other than a different excitation geometry. The primary difference with the microscope lies between toggling between LightField, which is Princeton Instruments' (the EMCCD manufacturer) proprietary software for camera control, and the Wright Group's homebuilt software for hardware control (`yaqc-qtpy`) and experiment orchestration (`bluesky-cmds`) and knowing when to use which software.

8.2 Workflow and best practices for taking data with the microscope

The workflow is split into two parts. The first part includes the finding and optimization of signal (whatever that signal may be). The second part includes setting up and taking scans using the

EMCCD as a detector. During the first part only LightField should be used to toggle camera settings (exposure time, gain, etc.) because the software makes those settings easily accessible which is ideal for signal optimization. Also during the first part the camera daemon should not be running. Once signal is optimized, the LightField software can be shut down and the camera daemon can be run (in either the background or foreground).

This workflow assumes a transmission geometry as that's the only geometry implemented to date. The other key assumption for this workflow is the use of the Mitutoyo 20X long working distance objective as the microscope objective. The Goldsmith group owns two of these objectives, I borrowed one from them. Also note that I write this procedure from memory, so the exact terminology for LightField operations may not be exact but they will be close.

To complete the first part of the workflow (finding and optimizing signal):

- Turn camera power on (black Princeton Instruments power box above actual camera) and boot up LightField software
- Go to the Devices tab in LightField and "Connect" the EMCCD. Alternatively, the EMCCD can be connected to the software by dragging the EMCCD icon to the small optical table near the middle of the screen
- Wait for the EMCCD sensor to cool down to -70° F. Do not toggle camera settings until the sensor temperature has reached -70° F
- Place the 500-μm pinhole into the correct optical table slots
    - The excitation beams should be aligned through the pinhole at this point

- Once the sensor temperature has reached -70° F, we'll need to change the camera's online processing to account for the its 90° rotation in the lab frame (it's technically on its side to avoid the camera cooling fan blowing into the leak line)
    - On the LHS of LightField click the Online Processing drop down. There will be an Orientation section. Click the Left Arrow – the camera will now process images in the correct lab frame so they are right side up in LightField (Note: the camera daemon automatically accounts for this)
- Use the white light lamp (black Dolan Jenner model) to make sure objective is imaging the 500-µm pinhole
    - Turn white light lamp on to lowest intensity setting
    - Apply roughly ND=2 to lamp to avoid saturating the camera
    - Turn camera exposure time to 50-100 ms in LightField
    - Confirm that excitation beams are shuttered/blocked
    - Click "Run" in upper right-hand corner of LightField to get live video feed
    - Use the horizontal and vertical kinematic knobs on the objective mount to center the objective's field of view on the 500-µm pinhole
- Remove the pinhole and insert the xyz-stage with mounted sample into the microscope sample area
- Locate sample area of interest using xyz-stage and adjust camera exposure time if needed
- Now that the sample is in the microscope's field of view, we need to ensure all the excitation beams are overlapped with the sample
    - Turn off the white light lamp
    - Turn up the ND all the way on all excitation beams that are being used

    - Let one of the excitation beams into the microscope beam path
    - You should see the beam's FWHM overlapping the sample area of interest. Adjust ND and camera exposure time settings as needed to obtain good visibility of the beam and sample
    - If there is not good overlap, make minor adjustments to beam pointing with kinematic mounts that house excitation mirrors
    - Shutter/block beam
    - Repeat this process for all excitation beams
- Now the instrument is ready to look for signal
    - Make sure camera is not acquiring
    - Place any color, polarization, etc. filters into the microscope beam line. These should be placed right before the imaging spectrograph slit. Image quality does not suffer with filters at this position. Ideally, the filters are pressed up against the slit housing to reject any stray light from lasers and/or room lights
    - Turn ND on excitation beams back to reasonable values (ones that you expect to use during scans)
    - At this stage I like to put the fs system enclosure around the microscope back up so the exploratory images are a better representation of what the images will look like when taking scans
    - There are two settings you can change to increase pixel counts: exposure time and electron multiplication (EM) gain. The EM gain can be changed in LightField using the panels on the left-hand side of the screen.

        - I always start the exploratory stage with the exposure time and EM gain low since the signal intensity is not known, and there may be stray light getting to the detector. Continually increase the exposure time and EM gain and hopefully signal is seen
        - Continue to optimize other experimental variables (beam pointing, delay, etc.)
    - Once signal is found, determine the EM gain value and camera exposure time that will be used during scans. Ideally the highest pixel intensity value is just under the saturation point of 2^{16} or ~65k counts. This will result in the highest S/N. However, it may take an unreasonably long exposure time to get to saturation. You will have to compromise exposure time and pixel counts to work with your experimental goals and time frame
    - Once these parameters are known, turn off LightField

We can now move on to the second part of the workflow:

- Once LightField is off, turn on the camera daemon (`pi-proem`) in either the foreground or background. Wait ~10 s to let it boot up
- Once it boots up successfully, start `yaqc-qtpy`
- Once `yaqc-qtpy` boots up successfully, get to the camera daemon console. Use `c.set_em_gain(int)` and `c.set_exposure_time(float, in ms)` to change the required settings. If you want to take multiple images and average or sum them together for a datum point, use `c.set_readout_count(int)`. The camera daemon exposes a few other camera settings but these are the most common

- Now boot up `bluesky-cmds`. With the camera daemon already running, `bluesky` should recognize it (to check this, see if you can make a `yaqc_bluesky.Device()` object with the camera – if you can, then it will appear in the `bluesky` GUI). It can take up to 30 s for `bluesky` to recognize the camera daemon
- Scans can now be taken using the microscope camera. A few miscellaneous bits of information:
    - You can use multiple `Devices` in one scan, e.g. the DAQ and camera daemons can collect data concurrently
    - `Bluesky` refreshes/updates queue progress at the camera frame rate, which will likely be slow for your experiment compared to non-spatially resolved CMDS experiments

8.3 Toggling between 2D spatial and spectral imaging modes

Toggling between the 2D spatial imaging and spectral channels is straightforward. The following method is robust so long as you are gentle with the optics. To go from 2D spatial -- > spectral imaging:

- Make sure the camera is not running or acquiring an image
- Remove the top cover of the imaging spectrograph housing. Then remove the side panel nearest to you
- You will need to flip down two mirrors and flip up two mirrors to prepare the beam properly. Refer to the Imaging Spectrograph section in Chapter 2 for an optical layout of the spectrograph's different imaging channels

- I keep the grating in the imaging spectrograph. It sits on top of a magnetic mount – remember to be gentle when you mate it with the other half of the magnetic mount
- To make sure the spectrograph is aligned properly, use the white light lamp and a 600 +/- 10 nm BP filter to center the peak on ypixel=255, xpixel=255 while using LightField. Right clicking the image will give you the option to view the full image of horizontal slices at specific y pixels. I prefer the horizontal-slice view when calibrating the spectrometer. In this view there is an automated peak finding method in LightView that I use when calibrating the spectrograph
    - If the 600 nm peak is not centered at ypixel, xpixel=255, 255 change the pointing of the beam into the grating. Only slight adjustments should be needed (if big adjustments are needed, you weren't gentle enough when changing imaging channels*). Use the horizontal kinematic knob on the mirror just before the grating to change the pointing*. For reasons that I still don't understand, the dispersion of transmission gratings is not sensitive to the angle of incidence (see Traub *et al*., *JOSAA*, **1990**, *7*, 1779-1791) so slight beam-pointing changes are not problematic.

To go from spectral → 2D spatial imaging, reverse the steps above (minus spectrometer calibration).

8.4 Procedure for shot-to-shot frame rate capabilities

The procedure that follows will allow the data acquisition software to run scans where the microscope camera's frame rate is shot-to-shot, or 1 kHz. Having this capability is prudent for pump-probe measurements where the probe field is intense relative to typical four wave mixing

signals (e.g. transient absorption compared to transient SHG) and was motivated in detail in Chapter 4.1.

1. Scenario: A transient absorption microscopy delay trace of 50 points needs to be taken. At each delay point 1000 laser shots will be collected. With a 1 kHz laser system, this corresponds to 1 second per data point and a 50-second delay scan.
2. The EMCCD does 2 x 2 binning and collects a 120 μm x 120 μm pixel area to achieve the required frame rate of 1 kHz. Thus, the dimensionality of the scan is (50, 120, 120) for (delay, y-pixel, x-pixel).
3. The *n_frames* parameter is set to 1000 and the *exposure_time* parameter is set to 1 ms in the camera daemon settings.
4. The scan starts and all 1000 camera images are taken for the data point at the first delay position. The camera daemon status is BUSY. The camera daemon calls the DAQ daemon and acquires its array with the chopper phases, 1 for pump-on and -1 for pump-off.
5. Through `numpy` advanced indexing the (1000, 120, 120) array of camera images and the (1000,) array of chopper phases are used to create a pump-on array and pump-off array. Each array will have a shape of (500, 120, 120).
6. The average of each array along the laser shot axis is taken (500 images averaged) which leaves behind two arrays, both with shape (120, 120). Each array is an averaged pump-on and pump-off image of the sample.
7. The pump-off array is subtracted from the pump-on array leaving behind one transient image with shape (120, 120).

8. The transient image is returned to the data orchestration software and the camera daemon status is no longer BUSY. The delay stage moves to the next motor position and the process repeats, starting at Step 4.